6-4-2014 12:00 AM

Shock Metamorphic Effects in Lunar and Terrestrial Plagioclase Feldspar Investigated by Optical Petrography and Micro-X-Ray Diffraction

Annemarie E. Pickersgill
The University of Western Ontario

Supervisor
Dr. Gordon Osinski
The University of Western Ontario Joint Supervisor
Dr. Roberta Flemming
The University of Western Ontario

Graduate Program in Geology
A thesis submitted in partial fulfillment of the requirements for the degree in Master of Science

SHOCK METAMORPHIC EFFECTS IN LUNAR AND TERRESTRIAL PLAGIOCLASE FELDSPAR INVESTIGATED BY OPTICAL PETROGRAPHY AND MICRO-X-RAY DIFFRACTION

(Thesis format: Integrated Article)

by

Annemarie Elisabeth Pickersgill

Graduate Program in Geology (Planetary Science)

A thesis submitted in partial fulfillment
of the requirements for the degree of
Master of Science - Geology (Planetary Science)

The School of Graduate and Postdoctoral Studies
The University of Western Ontario
London, Ontario, Canada

Abstract

Shock metamorphism, caused by hypervelocity impact, is a poorly understood process in feldspar. This thesis addresses: a) developing a quantitative scale of shock deformation in plagioclase feldspar; b) expanding the utility of plagioclase feldspar for determining shock level; and c) micro-X-ray diffraction as a technique with which to study shock in feldspar.

Andesine and labradorite from the Mistastin Lake impact structure, Labrador, Canada, and anorthite from Earth's moon, returned during the Apollo program, show shock effects such as diaplectic glass. Planar deformation features are absent in plagioclase, but abundant in terrestrial quartz. A pseudomorphous zeolite phase (levyne-Ca) was identified as a replacement mineral of diaplectic feldspar glass in some terrestrial samples. Micro-X-ray diffraction patterns revealed increased peak broadening in the chi direction (χ) (due to strain-related mosaicity) with increased optical signs of deformation. Measuring the full-width-at-half-maximum (FWHMχ) of these peaks provides a quantitative way to measure strain in shocked samples.

Keywords

Impact cratering, shock metamorphism, shock metamorphic effects, anorthosite, andesine, labradorite, anorthite, plagioclase, feldspar, levyne-Ca, diaplectic glass, maskelynite, planar deformation features, Mistastin Lake, Apollo, micro-X-ray diffraction, strain-related mosaicity.

Co-Authorship Statement

I conducted the laboratory work (optical petrography, scanning electron microscopy, and micro-X-ray diffraction), and processed and analyzed the data. I also developed the ideas, and wrote the papers. Dr. Osinski and Dr. Flemming provided training on instruments, guidance on how to conduct research, proper presentation of the material, and discussion about shock effects in minerals.

Acknowledgments

There are a great number of people and organizations who I must thank for their assistance in helping me to finish this thesis.

First and foremost I must thank my supervisors, Dr. Gordon Osinski and Dr. Roberta Flemming, for their constant guidance, feedback and support (both financial and moral) through every stage of this project, and for the inspiration to start down this path in the first place. Their support has provided me opportunities that had never crossed my mind before I met them, and no matter what crazy idea I had for my next adventure, they always helped me find a way to make it so. The discussions we had together helped me to increase my own understanding of impact cratering, mineralogy, crystallography, shock metamorphism, and science as a process. So truly thank you, Oz and Robbie, for a great M.Sc., and for all the time and effort you put into me over the past 7 years.

Collecting samples for this project was an adventure in itself, so for helping me weather the hurricanes, the snowstorms, the wildlife, (the blackflies), and all the other challenges of working and camping in Labrador, I have to thank Cassandra Marion, Marianne Mader, Marc Beauchamp, Raymond Francis, Kelsey Young, and Alaura Singleton. Without you I would almost certainly have been blown away by the wind that never stops, and I certainly would have lost my mind from the isolation. You really helped to turn down the suck.

I have to thank the Curation and Analysis Planning Team for Extraterrestrial Materials (CAPTEM) for granting me use of the Apollo sample collection. And I have to thank Ryan Zeigler, Andrea Mosie, and Anne Kascak for helping to arrange my visit to Johnson Space Centre, for escorting me everywhere while there, for showing me the amazing facilities, and for bearing with my incessant questions and need to photograph the whole adventure.

Over the years I have benefited greatly discussing various aspects of this project with numerous minds more educated than my own, including Marianne Mader, Cassandra Marion, Alaura Singleton, Emily McCullough, Marc Beauchamp, Kate Souders, Steven Jaret, Phil McCausland, Michael Craig, Ludovic Ferrière, Bevan French, and Richard Grieve. You all

helped me to develop my ideas in coherent scientific thoughts, and without you this thesis would make a lot less sense.

All of the Spacerocks crew and Mineralogy groupies, past and present, who have provided feedback on presentations, shoulders to cry on, shoulders to lean on, helpful distractions, and a whole lot of fun times, you guys rock, and without you my time here would have been nowhere near this level of awesome. My next research group will be hard pressed to live up to the level of greatness I've come to expect from my colleagues because of you.

No acknowledgements would be complete without a big thank you to my many, many, financial sponsors. Funding for my degree was provided by the Natural Sciences and Engineering Research Council (NSERC) through a Canada Graduate Scholarship, and through the Ontario Graduate Scholarship. Fieldwork was funded by the Canadian Space Agency and the Northern Scientific Training Program. A generous award from the Nanofabrication facility at Western provided SEM training and instrument time. The NSERC CREATE Technologies and Techniques for Earth and Space Exploration program provided travel funding and training opportunities to expand my research. Additional travel funding to attend conferences was provided by the Lunar and Planetary Institute, the Mineralogical Association of Canada, and the Meteoritical Society.

My dear friend Emily McCullough has provided immeasurable emotional support, invaluable scientific feedback, and incredible editing skills of not only this thesis but also the many applications I had to submit while completing my degree. She has helped me keep my science on track, kept me excited about the work, and has provided helpful encouragement and problem solving skills at each and every roadblock. If it weren't for writing camp, this thesis would still exist only in my mind. And if it weren't for the tea and cookies (and cake)…I shudder to think.

Lastly, I must thank my family: my sisters Therese and Christine who have always been there for me; my brother-in-law Tony, who is quickly making up for lost time; and my parents Evelyn and Ron, without whom I would not have had the confidence, discipline, skill, or desire to pursue a career in research. You are the best, and you help me to constantly aim to live up to that.

Table of Contents

List of Tables

List of Figures

List of Appendices

Chapter 1

1 Introduction and Literature Review

Meteorite impact craters are the dominant surface feature on most terrestrial planetary bodies and, as such, they can provide fundamental information about planetary evolution through excavating large amounts of material and providing windows into the subsurface. It is, therefore, important to have a good understanding of exactly how impact events modify the rocks and minerals of the target body. By studying impact craters on Earth, we gain context for geological samples collected at various locations in and around impact craters on other planetary bodies. This will provide insight into the geological foundations of all rocky planetary bodies and meteorites, and contribute to the growing body of knowledge about the origins of our Solar System.

One of the most distinctive outcomes of hypervelocity impact events are the metamorphic features, which develop in rocks and minerals of the target material during passage of the impact-generated shockwave. This shock metamorphism causes distinctive and diagnostic changes to the target materials, which can provide us with information about the amount of pressure to which these materials were exposed during impact. The goal of this thesis is to further our understanding of shock metamorphic effects in plagioclase feldspar, one of the most common minerals throughout the Solar System. Below, I provide a brief introduction to the importance of impact craters, the crater-forming process, the products of that process, the current state of knowledge of shock effects in feldspar group minerals, and an overview of how this thesis will contribute to the field.

This thesis is divided into four chapters. Chapter 1 is meant to provide the necessary background to the reader to understand the importance of the thesis in the context of geological exploration of not only Earth, but the rest of the rocky planets and their development and evolution. Chapters 2 and 3 have been written as stand-alone papers presenting the effects of shock metamorphism in plagioclase feldspar, as observed optically and by micro-X-ray diffraction, respectively. Chapter 4 relates Chapters 2 and 3 to each other, places this work in the context of the wider field of shock metamorphism,

and suggests future work for furthering our understanding of how shock metamorphism affects feldspars.

1.1 Introduction

Due to the ubiquity of impact craters on rocky planetary bodies, an understanding of their formation is crucial to understanding the formation and evolution of the surfaces of these bodies. Through understanding shock metamorphism, we gain information about the peak pressures to which material was exposed during impact, which can help to inform our understanding of the cratering process, about which there are still many unanswered questions.

The effects of shock metamorphism on feldspar group minerals have been little studied thus far, due to the optically complex nature of feldspars, the ease with which they alter making them difficult to study using traditional optical techniques, and the existence of pre-existing planar features (i.e. cleavage planes, twin planes), which could easily mask or preclude the formation of shock-generated planar elements. Feldspar has, therefore, been underutilized as a shock barometer when compared to the optically more simple quartz. Quartz has dominated studies of shock metamorphic effects, due to its resistance to alteration, and more optically simple nature. However in quartz-limited, feldspar-rich systems, such as the surfaces of the Moon and Mars, and many meteorites and asteroids, a greater understanding of shock metamorphism in feldspars is required. Thus far, the shock scale for feldspar is currently limited, and purely qualitative, despite some studies having suggested that feldspar can be just as useful for shock barometry as quartz, especially at the lower end of the shock pressure scale (e.g., Jaret et al., 2009).

In addition to optical petrography, the main technique that will be used in this work is *in situ* micro-X-ray diffraction (μXRD), in an effort to quantify the amount of deformation experienced by the crystal structure as a result of shock compression. Optical determination of shock level in various minerals, terrestrial and meteoritic, has been done for many years. Determination of shock level through use of μXRD is a significantly

more recent development. Use of μXRD to quantify the level of crystal deformation through the measurement of streak length on 2D General Area Detector Diffraction System (GADDS) images (Flemming, 2007), has thus far been applied to pyroxenes (Izawa et al., 2011), olivine (McCausland et al., 2010; Vinet et al., 2011) and zircon (Moser et al., 2009). It has been successful in evaluating shock level through analyzing deformation of the crystal structure via strain-related mosaic spread, often showing strain before it appears optically (Izawa et al., 2011; Vinet et al., 2011).

This thesis provides input on the effects of shock metamorphism in lunar and terrestrial plagioclase feldspar, through the use of optical, and scanning electron microscopy, cathodoluminescence imaging, and *in situ* micro-X-ray diffraction for a comparative study of samples from terrestrial craters and those returned from the Moon by the Apollo program (1969-1972). Specifically, two sample suites will be discussed: 1) a suite of samples from the Mistastin Lake impact structure, some of which have been well characterized in terms of shock metamorphism of quartz, and some of which are nearly pure anorthosite; and 2) a subsection of the Apollo samples, some of which have been well characterized in terms of shock metamorphism, and some of which have not. Investigating these suites using both petrographic and μXRD techniques will expand the use of feldspars as shock barometers, by contributing to the development of a more robust and quantitative series of shock criteria in feldspars and assist in subdividing the lower end of the shock scale. Given the ubiquity of feldspar, in particular plagioclase, in the lunar highlands, this research will benefit our understanding of the impact record on Earth's moon, and the nature of the lunar surface.

Lunar exploration is a primary goal of space agencies the world over. Specifically, the lunar highlands, primarily composed of heavily cratered anorthosite, have generated the most interest and are on the short list of destinations for future missions. By better understanding how shock affects the crystal structure of feldspar group minerals, we can use them as accurate shock barometers. Understanding shock in feldspars on Earth will prepare us to study samples returned from the Moon and understand the craters from which they originate, thus increasing the scientific return of lunar exploration.

1.2 Impact Craters

Meteorite impact craters are the dominant surface feature on most terrestrial planetary bodies and, as such, they provide important information about planetary evolution. In addition to being nearly ubiquitous on solar system bodies with hard surfaces, their formation excavates large amounts of subsurface material and they, thereby, provide windows into planetary interiors (e.g., Gault et al., 1968; Melosh 1989; Osinski and Pierazzo, 2013).

1.2.1 Formation

When a hypervelocity impact occurs between an object such as an asteroid or comet and the surface of another planetary body, it generates a shockwave that propagates through both the projectile and the target material (Melosh, 1989). This shockwave excavates a crater and causes immense deformation of the target and vaporization of all but the most robust impactors. Signs of the impact such as crater morphology, impactites, and shock metamorphic effects, can be seen at many scales, even billions of years after formation (e.g., French and Koeberl, 2010; Osinski and Pierazzo, 2013).

The crater formation process has been split into three main stages by Gault et al. (1968): contact and compression, excavation, and modification. All three of these stages happen incredibly quickly, faster than any other known geological process, taking seconds to minutes from initial contact for the final crater to form, and only minutes to hours for final deposition of the ejecta blanket (Melosh, 1989).

1.2.1.1 Contact and Compression

The impact cratering process begins with contact of the projectile with the target surface, which establishes a series of shockwaves, which facilitate the transfer of kinetic energy of the projectile into the target material (Gault et al., 1968). One shockwave propagates through the target material, the other through the projectile. When the shockwave reaches a free surface (the surface of the target or projectile), it is reflected back as a rarefaction wave, which serves to relieve the high pressures generated by the shockwave. Passage of the rarefaction wave often results in complete melting or vaporization of the projectile

(Gault et al., 1968; Melosh, 1989). Passage of the shockwave and subsequent rarefaction wave results in shock metamorphism, melting, and vaporization of target material – depending on proximity to the point of contact (Ahrens and O'Keefe, 1972; Grieve et al., 1977; Melosh, 1989; Stöffler and Grieve, 2007). The end of the contact and compression stage is marked by total unloading of the projectile, which usually occurs 10^{-3} to 10^{-1} seconds after initial contact, >1 second for only the largest impacts (Melosh, 1989).

1.2.1.2 Excavation

The gradational transition between the contact and compression stage and the excavation stage is characterized by the development of a hemispherical shockwave that propagates through the target (Gault et al., 1968; Melosh, 1989). The passage of this shock and rarefaction waves loosens and mobilizes material and excavates an initial transient cavity, with a diameter many times larger than the projectile itself (Gault et al., 1968; Melosh, 1989). As the shock wave passes through target material, lithic and mineral fragments become shocked, to decreasing degrees the farther the material is from the point of contact. It is during this stage that some material is ballistically ejected beyond the rim of the transient crater to form the continuous ejecta blanket (Oberbeck, 1975). Further ejecta is emplaced by ground-hugging flows near the end of the excavation stage (Osinski et al., 2011). In addition to forming the ejecta blanket, some melt rock and impactites remain within the transient crater to form crater fill. The excavation stage lasts seconds to minutes depending on crater size, and the end is marked by the point at which the shock- and rarefaction waves no longer have the energy to displace target material (Melosh, 1989).

1.2.1.3 Modification

After the crater has been fully excavated, the modification stage begins. This stage is characterized by the modification of the transient cavity by gravitational forces, and the effects are, therefore, governed by the size of the transient cavity, the properties of the target rock, and the size of the impacted body (Melosh and Ivanov, 1999). In small craters (<2-4 km on Earth), this is manifested as debris sliding down the walls of the cavity and collecting in the bottom (Melosh, 1989). In larger craters, inward and upward

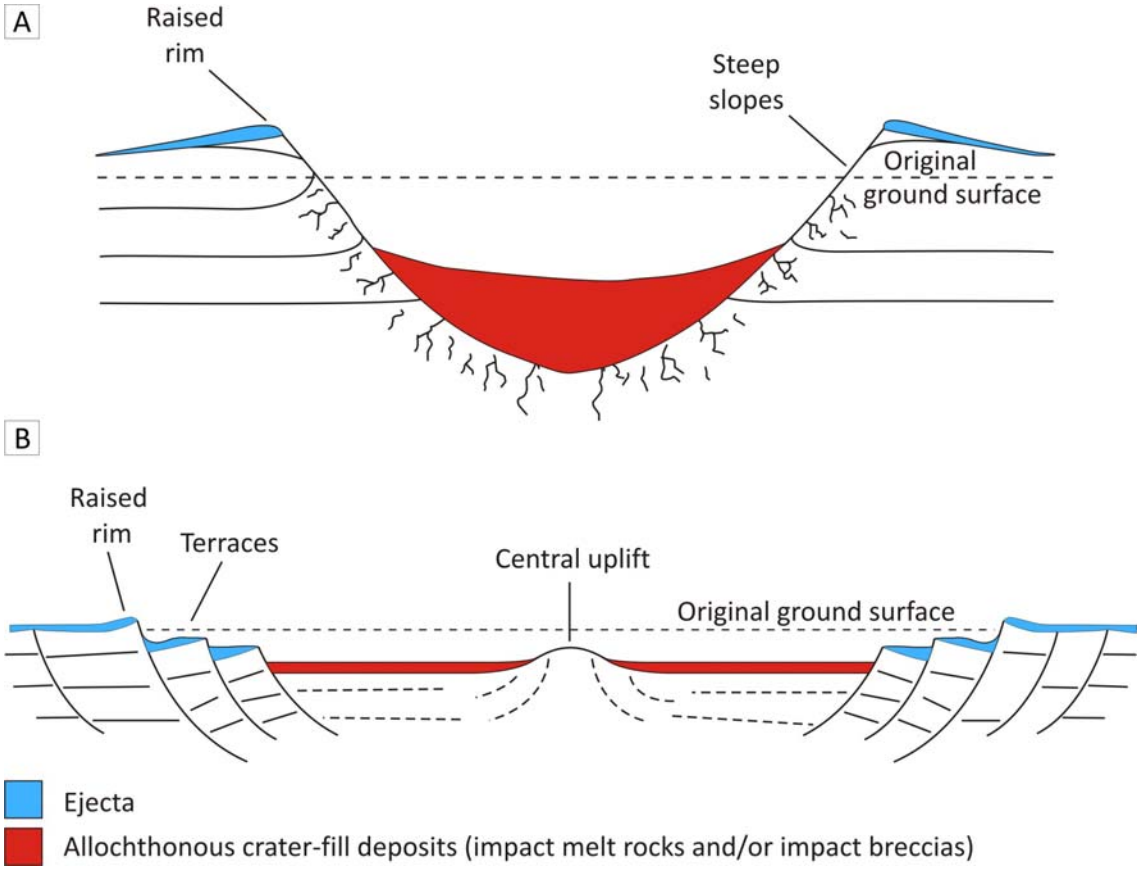

Figure 1-1: Simplified cross sections through a simple crater (A) and a complex crater (B). Both have a raised rim, and a crater floor below the original ground surface but the simple crater has steeper sides and a bowl shape, while the complex crater has terraced walls, a shallower profile, and a central uplift. Modified from Osinski et al. (2011).

movement of material within the transient cavity results in the formation of a central uplift, while the steep walls of the transient cavity undergo gravitational collapse forming slump terraces on the walls (Gault et al., 1968; Melosh, 1989). There is no clearly marked end to this stage of crater formation, as the processes which govern it slowly merge into well-known endogenic processes such as erosion (French, 1998; Osinski and Pierazzo, 2013).

1.2.2 Impact Crater Morphology

Impact craters have been split into two main groups based on final crater morphology. Simple craters are small bowl shaped craters, with a raised rim and steep slopes (steepest near the edge than decreasing towards the centre in a nearly parabolic cross-section, Figure 1-1A) (Melosh, 1989). The depth from rim to floor is usually ~1/5th the crater diameter (Melosh, 1989). As the diameter increases, the crater becomes shallower compared to its diameter, and develops a terraced rim, a morphology termed "transitional craters" for an appearance between simple and complex (Melosh, 1989).

Larger diameter craters have a similar shallow profile to transitional craters, a relatively flat floor, and a terraced rim. They have additionally developed a central uplifted portion, and have a more complex crater rim structure (Figure 1-1B). On other planetary bodies, craters are preserved at even larger diameters than the complex craters we see on Earth. Such craters develop into central-peak basins (with a ring of peaks surrounding a central peak), to peak-ring basins (well developed ring of peaks surrounding the centre of the crater, but no central peak) (Stöffler et al., 2006). Multi-ring basins on the Moon are frequently considered the next size up on the impact crater size scale, but they do not follow the normal scaling relationships of smaller sized craters (Melosh, 1989).

1.2.3 Products

The extreme temperatures and pressures produced by hypervelocity impact generate many characteristic rock types and features (e.g., French and Short, 1968; Roddy et al., 1978; Stöffler and Grieve, 2007; French and Koeberl, 2010). The resulting metamorphosed rocks are grouped under the name impactites – "rocks which have been affected by the hypervelocity impacts generated by colliding planetary bodies" (Stöffler and Grieve, 2007).

1.2.3.1 Shock metamorphism

Shock metamorphic effects are the result of *solid state* deformation of rocks and minerals on a microstructural level. This deformation of the crystal structure is caused by passage of the shockwave through the target material, causing far higher temperatures and

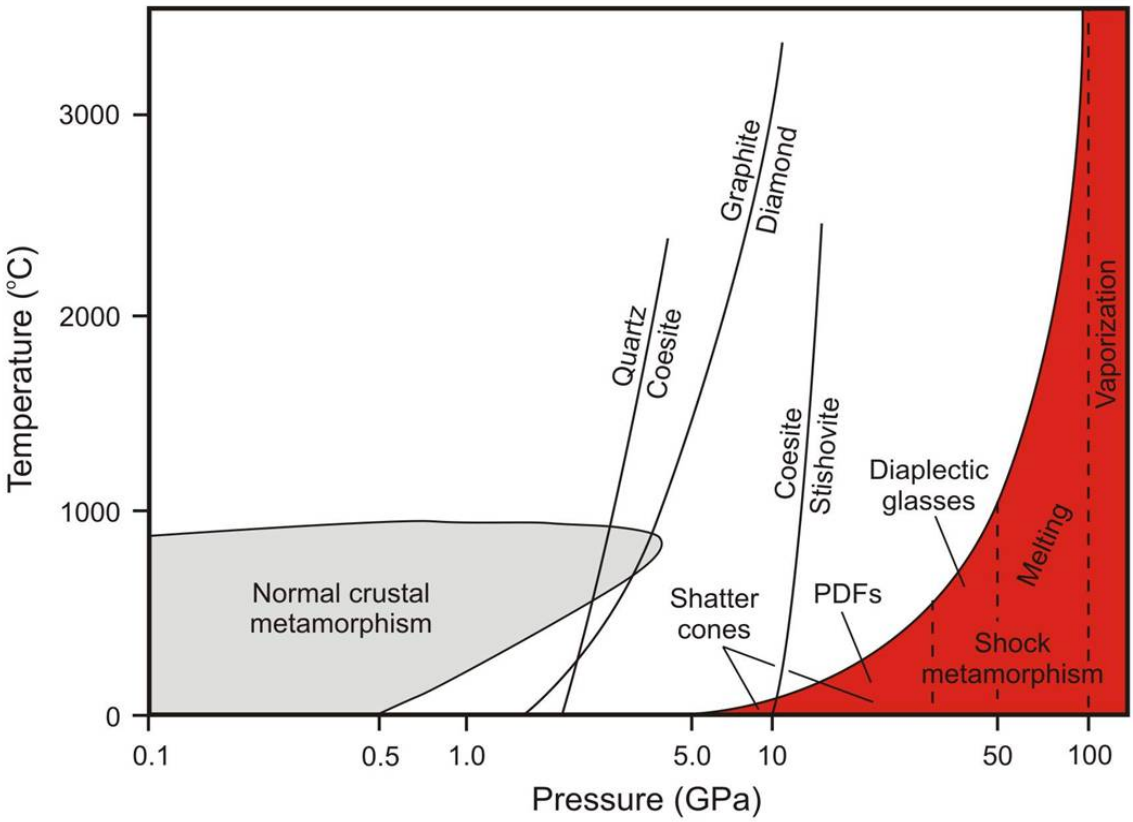

Figure 1-2: Temperature vs. pressure graph of shock metamorphism highlighting major shock indicators. Pressures and temperatures involved in impact processes (dark grey) are far higher than those produced endogenically. Figure from (French, 1998).

pressures than those produced during normal crustal metamorphism on Earth (Figure 1-2). The degree of shock metamorphism of the material is indicative of the peak pressure to which material was exposed during impact. Since the shockwave dissipates as it moves out and away from the point of contact, material located farther from the point of contact is subjected to lower pressures (lower shock level) than material closer to the point of contact (higher shock level). As a result of this pressure gradient, it becomes possible to estimate where in the pre-impact stratigraphy rocks and minerals originated (e.g., Engelhardt, 1990; French and Koeberl, 2010).

Shock effects vary depending on the mineralogical and microstructural nature of the target rock (Ferrière and Osinski, 2013; French and Koeberl, 2010). As a result, there are different shock level classification schemes for quartzofeldspathic rocks, basaltic-gabbroic rocks, dunitic and chondritic rocks, sandstone, and particulate rock material (Stöffler and Grieve, 2007). Shock effects are mineralogically selective, meaning that they will occur in grains of one mineral, but not in grains in of adjacent different minerals (French, 1998). They are also heterogeneous in distribution, meaning that even adjacent minerals of identical composition might display different effects. Shock deformation occurs in all minerals; the extent and exact nature of the deformation depends on crystal structure and mineral composition (Stöffler, 1972). Shock deformation is characterized by progressive destruction of the crystal structure and original textures until melting occurs. Outlined below are the signs of shock metamorphism.

1.2.3.1.1 Shatter cones

Shatter cones are the only accepted macroscopic diagnostic feature of shock metamorphism (Dietz, 1960, 1947; French and Koeberl, 2010). These are roughly conical fracture surfaces with radiating "horsetailing" striations (e.g., French, 1998; Baratoux and Melosh, 2003; French and Koeberl, 2010). They form at relatively low shock pressures, and in large volumes of the target rock (Dietz, 1959; Milton, 1977).

1.2.3.1.2 Planar microstructures

Planar microstructures have long been accepted as indicators of shock in quartz, and can be divided into planar fractures (PFs) and planar deformation features (PDFs) (e.g., French and Short, 1968). The orientation of both are crystallographically controlled and as a result they are parallel to rational crystallographic planes (Ferrière and Osinski, 2013). PFs and PDFs are distinct from each other in that PFs are open cracks, often >3 μm wide and spaced ~15-20 μm apart (Langenhorst, 2002; Stöffler and Langenhorst, 1994). Planar deformation features (PDFs), on the other hand, are closed parallel planar lamellae along which glass is typically found, they are less than 2 μm thick, and typically spaced 2-10 μm apart (Engelhardt and Bertsch, 1969; Stöffler and Langenhorst, 1994). Post-shock annealing of PDFs results in 'decoration' by tiny fluid inclusions aligned with

the original PDF direction (Ferrière and Osinski, 2013; Stöffler and Langenhorst, 1994). Planar deformation features which branch off of PFs are termed feather features (Poelchau and Kenkmann, 2011). Shock loading experiments have correlated peak pressures with number and orientation of PDF sets in quartz, making refined pressure estimates from PDF measurement possible. Planar microstructures have also been observed in other minerals than quartz; such as, olivine, pyroxene, amphibole, sillimanite, garnet, apatite, and feldspars (e.g., Chao, 1967; Stöffler, 1972; French, 1998; Langenhorst, 2002).

1.2.3.1.3 Kink Bands

Kink bands in micas commonly occur at high angles to the prominent direction of cleavage (Chao, 1968). These are unfortunately not shock-diagnostic, as similar features also develop in ordinary metamorphic rocks (e.g., Spry, 1969).

1.2.3.1.4 Mosaicism

Optical mosaicism is an irregular/mottled extinction pattern displayed by crystals comprised of several subdomains, with different optic axes (e.g., Dachille et al., 1968; Stöffler, 1972; Stöffler and Langenhorst, 1994; French and Koeberl, 2010) Mosaicism is different from undulose extinction in which the crystal has not resolved itself into individual subdomains. Kink bands and planar microstructures are commonly associated with optical mosaicism (e.g., Stöffler, 1972). Because a similar extinction pattern can also be developed by endogenic processes (e.g., Spry, 1969), it cannot be used as a diagnostic indicator of shock metamorphism.

1.2.3.1.5 Refractive index, birefringence, and density

Refractive index, birefringence, and density all decrease with increasing shock pressure until the crystal reaches an amorphous state (Stöffler and Langenhorst, 1994; Stöffler, 1974). In quartz and feldspar, this begins to happen at pressures of 20-30 GPa (French, 1998).

1.2.3.1.6 High pressure polymorphs

Some minerals are converted under shock compression into high-pressure polymorphs that are normally only stable in the lower crust or mantle of Earth. While these are uncommon on the surface of the Earth, many can be produced by endogenic processes and so it is only in combination with geologic context that such features are considered shock-diagnostic (French and Koeberl, 2010).

1.2.3.1.7 Diaplectic glass

Diaplectic glasses, sometimes called *thetomorphic glasses*, are glasses which have become optically isotropic, amorphous (to X-rays, Raman, etc), and yet retain the chemical composition, morphology, texture, and internal features of the original mineral grain and, therefore, preserve the original fabric of the rock (French and Koeberl, 2010). They do not show flow textures or vesiculation. They are known to preserve grain boundaries, cleavage, and twin lamellae of their precursor grain. It is not uncommon to find only part of grain which has become diaplectic glass, leaving the remainder birefringent (French, 1998; Stöffler, 1971).

Amorphism suggests that these grains have lost their internal ordered atomic arrangement, however, diaplectic glasses do retain a significant degree of short-range structural order compared to melt glasses (French and Koeberl, 2010). Similarities in the mid- and far- infrared spectra of diaplectic and synthetically fused glasses indicate a similar degree of short-range order and lack of long-range order in their structures (Arndt et al., 1982). Diaplectic glasses typically demonstrate decreasing refractive index and density with increasing shock level. They have higher density and refractive index than compositionally equivalent fused glass, which suggests that diaplectic glasses have more compact structures (Arndt et al., 1982). The structure of diaplectic glasses appears to be inhomogeneous, with different areas showing different degrees of order (Arndt et al., 1982). Upon heating at ambient pressure, diaplectic glasses are known to recrystallize to microcrystalline aggregates that preserve the original shape of the crystal, or to recrystallize back into the original crystal, even sometimes regaining undulose extinction (Arndt et al., 1982). With increasing shock pressure, temperature, and shock pulse

duration the crystalline structure becomes increasingly disordered, as a result the 'frozen-in' memory of diaplectic glass is expected to be increasingly lost until it matches the complete lack of memory of fused glass (Arndt et al., 1982).

Diaplectic glasses are metastable, and apparently cannot survive even mild post-impact thermal effects. As a result, recrystallized feldspars are more common, with textures suggesting plastic deformation, and plumose or spherulitic, microcrystals which are interpreted to indicate post-shock heating or metamorphism of diaplectic feldspar glasses (French, 1998). As a result diaplectic glasses are often outlasted by decorated planar deformation features. In some grains described as diaplectic glasses, plastic behaviour is indicated, such as indentations of matrix into a clast or through bending of original polysynthetic twinning (French, 1998).

Diaplectic glasses generally form from framework silicates, such as quartz and feldspar, but have occasionally been associated with other precursor minerals (e.g., Stähle, 1973). Diaplectic quartz and feldspar glasses form at approximately 30-45 GPa, corresponding to shock level II of Stöffler (1971), and shock level 5 of Singleton et al. (2011). Diaplectic glasses are found in smaller volumes of target rock than planar deformation features and shatter cones, because they require higher pressures to form and are, therefore, more restricted in extent than features that form at lower pressures.

There is ongoing debate about the mechanism by which diaplectic glass forms. While there are several hypotheses, none of them yet explains all of the observations of diaplectic glasses. The glassy state of the material, without evidence of melt or flow, suggests a near instantaneous transition from crystalline texture to glass via solid-state collapse of the crystal structure, without melting (e.g., De Carli and Jamieson, 1959; Engelhardt and Stöffler, 1968). In general, formation hypotheses fall into two main camps: rapidly quenched monomineralic melt, or solid-state structural collapse/ destruction of the ordered internal atomic arrangement of the precursor mineral. Some hypotheses are outlined below:

Langenhorst (2002) found quenching of a liquid more probable than solid-state transformation due to common associations between diaplectic quartz glass and coesite, which crystallizes from a high pressure melt.

Grady (1977) suggested that diaplectic glass is the result of solidification on pressure release of a melted high-density phase, which quenched so quickly as to disallow liquid diffusion that would normally be expected to erase the morphology and texture of the crystals. Melting is attributed to local temperature spikes as a result of the heterogeneous nature of shock compression, allowing for areas of local increased temperature despite bulk rock temperature remaining below the liquidus (Grady, 1980; Grady et al., 1975).

Arndt et al. (1982) found that the most probable formation mechanism for diaplectic glass is that high temperatures induced from shock cause melting in compressed labradorite, but the duration of the high temperature is so brief that the transition to liquid is incomplete. As a result, the disordered transitional state is 'locked in', forming diaplectic glass.

Ahrens et al. (1969) suggested that diaplectic glass is the result of solid-state release from a high-pressure phase during decompression. This interpretation is the result of shock experiments on plagioclase.

1.3 Feldspar Minerals

Feldspar group minerals are the most abundant constituents of igneous rocks and, therefore, commonly occur in sedimentary and metamorphic rocks as well (Deer et al., 2001). The feldspar group is comprised of two series of solid solutions: plagioclase feldspar ($CaAl_2Si_2O_8$-$NaAlSi_3O_8$) and alkali feldspar ($NaAlSi_3O_8$-$KAlSi_3O_8$) (Figure 1-3). The crystal system varies with composition, crystallization temperature, and thermal history. The plagioclase series is triclinic from anorthite to oligoclase, with albite generally triclinic but monoclinic at high temperature. In the alkali series, anorthoclase is triclinic, but may be monoclinic at high temperature, and sanidine is monoclinic. Intergrowths of the two series are common, such as perthite and antiperthite. The most

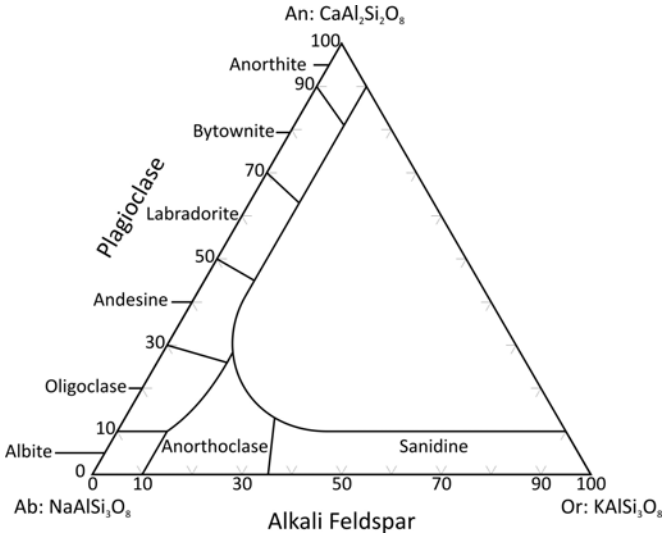

Figure 1-3: A feldspar ternary diagram illustrating the solid solution between anorthite (An) and albite (Ab), and between albite and orthoclase (Or). Modified from (Deer et al., 2001).

common rock-forming mineral series is plagioclase, which is found in most igneous rocks, commonly in metamorphic rocks, and also occurs in sediments as both primary and authigenic minerals (Deer et al., 2001).

Plagioclase feldspars demonstrate two good cleavages {001} and {010} at 93-94° and one poor cleavage, which is generally not noticeable (Nesse, 2004). Polysynthetic twinning in plagioclase is common, whereby alternating lamellae of plagioclase (twins) are produced with crystallographic orientations rotated by 180° to relative to each other (Zoltai and Stout, 1984). Plagioclase commonly alters to sericite, clay, or zeolites, which may be concentrated in the core of grains, along twin lamellae, or uniformly distributed throughout the grain (Nesse, 2004).

Some terrestrial plagioclase contains small dark inclusions, which are often oxides of transition metals, concentrated around intrinsic textural features such as twin boundaries and cleavage planes. This phenomenon is known as “clouded feldspar”. There are many proposed mechanisms for how clouding occurs, often involving water-assisted migration

of elements and a heat source. However, not all clouded feldspar is formed by the same process (Poldervaart and Gilkey, 1954; Smith and Brown, 1988; Whitney, 1972).

1.4 Shock effects in Feldspars

Fracturing is pervasive in impact metamorphosed rocks. Lambert (1979) conducted a study on shock-induced fracturing in quartz and feldspar and found that the density of fractures increases with increasing pressure up to ~20 GPa. Above 20 GPa, fracture density decreases with increasing pressure. However, the correlation between pressure and fracture density was found to be too poor to be of quantitative use in pressure calibration. Feldspars are more intensely effected by shock than quartz. Fractures appear to form at the end of the shock sequence, after diaplectic glasses, and upon pressure release (Lambert, 1979).

At 8-25 GPa, planar deformation features begin to form in feldspars. Planar microstructures have been less well-studied and characterized in feldspar than those in quartz. Feldspars can display various shock-related planar structures, including: planar fractures (PFs), deformation bands, kink bands, and planar deformation features (PDFs) (French and Short, 1968; French, 1998; Stöffler, 1972, 1967). When combined with more widely spaced features, such as twins or deformation bands, PDFs in feldspar can create a ladder texture (French and Short, 1968; Stöffler, 1972, 1967). Another type of planar microstructure observed in plagioclase is mechanical twins, which are sets of parallel bands up to 10 μm in width (Stöffler, 1972).

At 20-30 GPa, feldspar displays reduced refractive indexes and lowered birefringence (French, 1998). High pressure polymorphs with feldspathic composition have been synthesized and found in meteorites. $KAlSi_3O_8$ and $NaAlSi_3O_8$ with hollandite structure were synthesized by Ringwood et al. (1967) and Liu (1978) respectively. Natural $NaAlSi_3O_8$ and $KAlSi_3O_8$ hollandite has been found in chondrites, martian meteorites, and terrestrial rocks by analytical transmission electron microscopy (ATEM), X-ray diffraction, and Raman spectroscopy (El Goresy et al., 2000; Fritz and Greshake, 2009;

Gillet et al., 2000; Langenhorst and Dressler, 2003; Langenhorst and Poirier, 2000; Tomioka et al., 2000). Tomioka et al. (2000) interpreted natural $NaAlSi_3O_8$ hollandite formation from the host feldspar to be a solid-state reaction during shock, which also caused some of the plagioclase to be converted to maskelynite. Formation of $NaAlSi_3O_8$ hollandite is thought to occur stably at temperatures greater than 1200°C and pressures of 22-23 GPa (Yagi et al., 1994) or metastably at relatively low temperature where decomposition is hindered by slow reaction kinetics (Tomioka et al., 2000). The high-pressure phase jadeite (from plagioclase) is also commonly reported in meteorites and attributed to shock (e.g., Ohtani et al., 2004) but has not yet been found associated with terrestrial impact (Ferrière and Osinski, 2013).

At 30-45 GPa, diaplectic glass begins to form in feldspars. Conversion to an isotropic state can be partial or complete at slightly higher pressures. Occasionally, partial isotropization of a crystal occurs when only one set of alternate twin lamellae become isotropic, leaving the other set birefringent (Stöffler, 1966). This is suggested to be an effect of the crystal lattice orientation relative to the shock wave propagation direction (Stöffler, 1966). Thus far, diaplectic feldspar glasses have only been identified in crystalline rocks (Ferrière and Osinski, 2013).

There is significant controversy over the nature and nomenclature of diaplectic feldspar glass. Many authors use the term synonymously with *maskelynite*. Maskelynite was first described by Tschermak (1872) in the Shergotty meteorite as a previously unknown, isotropic mineral, with near labradorite composition. In 1883, Tschermak found the same substance in chondrites, realized that it was pseudomorphous with plagioclase, and subsequently reinterpreted it as a melted or otherwise vitrified glass of plagioclase composition. Then, Binns (1967) suggested a shock origin for maskelynite, and noted differences in the refractive index compared with fused glass of the same composition. Contemporaneously, Engelhardt and Stöffler (1968) and Engelhardt et al. (1967) proposed the use of the term *diaplectic glass* to refer to "amorphous phases produced by shock waves without melting, and [which] are distinguishable from ordinary molten glasses." Many authors began using *maskelynite* as a synonym for *diaplectic plagioclase glass* and, thereby, attached a genetic connotation to the term, while others continued to

use the terms separately. Modern techniques have allowed for observations of maskelynite in meteorites revealing flow textures, plastic deformation, and injection into surrounding crystals (Chen and El Goresy, 2000). As a result, the meaning of the term maskelynite has become ambiguous, and re-evaluation of its use is warranted. In this thesis, we therefore use the term diaplectic feldspar glass to refer to apparently solid-state shock amorphized material of feldspathic composition.

At ~45-50 GPa, feldspars begin to melt in non-porous crystalline rocks forming monomineralic feldspathic melt glass (Stöffler, 1972). Melting occurs at lower shock pressures in sedimentary rocks than crystalline rocks (Stöffler, 1972).

Shock effects in feldspars are more difficult to study than those in quartz because they display more diverse and complex effects, they are more optically complex (biaxial), and they alter easily to other phases resulting in erasure of shock effects.

1.5 Techniques used to study shock effects in feldspar

In addition to standard optical techniques, which are most commonly used to discover and describe the shock effects listed above, a variety of other laboratory techniques have been used to examine shock metamorphosed feldspars.

1.5.1.1 X-Ray Diffraction (XRD)

Kayama et al. (2012) gathered powder X-ray diffraction patterns of shocked and unshocked sanidine. They found almost no change in diffraction peak intensity between the groups, but did find slight peak broadening in 2θ with increased shock pressure, then a sudden change into an amorphous pattern with no detectable peaks.

Hörz and Quaide (1973) conducted shock experiments on oligoclase (3-34 GPa), andesine (4-10 GPa), and other silicates, and then examined the shocked materials with XRD using Debye-Scherrer film techniques, with a single crystal mounted on the tip of glass fibre. They found that the amount of crystal lattice fragmentation is closely related to shock pressure, and that by measuring the length of streaks created by X-ray

diffraction, they could begin to quantify the degree of strain and use it as a proxy for quantifying shock level. Walawender (1977) conducted single crystal X-ray diffraction studies of naturally shocked plagioclase from the Charlevoix impact structure, Quebec, and found increased streak length with increased shock level.

1.5.1.2 Cathodoluminescence (CL)

There have been multiple cathodoluminescence studies on shocked feldspars. Increasing shock pressure seems to result in increased CL intensity, and peaks shifting to lower wavelengths (e.g., Kayama et al. 2012).

1.5.1.3 Raman Spectroscopy

Increased shock pressure results in band broadening and reduced intensity in Raman spectra, in addition to peak shifting of some bands (Fritz et al., 2005; Reynard et al., 1999). Even at pressures < 26 GPa shocked plagioclase has wider full-width-at-half-maximum (FWHM) of characteristic Raman bands and reduced intensity compared to unshocked plagioclase. Amorphization of plagioclase around 26-40 GPa results in a broad plateau in the Raman spectra. With increasing pressure (40-45 GPa), there is further band reduction. At pressures much greater than 45 GPa, high post-shock temperatures lead to recrystallization (Fritz et al., 2005).

1.5.1.4 Thermal Infrared Absorption Spectroscopy

Thermal infrared absorption spectra of naturally shocked feldspars show decreased spectral detail and decreased intensity with increased pressure as a result of lattice disordering and increased glass content (Arndt et al., 1982; Bunch et al., 1967; Lyon, 1963; Ostertag, 1983; Stöffler and Hornemann, 1972; Stöffler, 1974). In experimentally shocked albite and anorthite, Johnson et al. (2003) found that albite shows increased absorption at 8-10 μm and weaker absorption at 14-29 μm. These features were found to persist at higher pressures in albite than anorthite, which agrees with previous thermal IR absorption studies of shocked feldspar (Johnson et al., 2002).

1.5.2 Techniques used in this thesis

This thesis uses the standard petrographic techniques of optical microscopy and scanning electron microscopy to gather information about microscopic textures. Further textural information was gathered using cathodoluminescence imaging. Chemical composition was gathered using electron probe microanalysis (EPMA) (list of standards and operating conditions in Table B-1, Appendix B). The main additional technique is micro-X-ray diffraction, the theory of which is explained in brief below.

1.5.2.1 Micro-X-ray diffraction

X-ray diffraction (XRD) works by the interaction of incident X-rays with a crystal lattice, causing constructive or destructive interference in the diffracted beam, as a function of the lattice spacing of the crystal, governed by Bragg's law: $n\lambda=2d_{hkl}sin\theta$ (Jenkins and Snyder, 1996; Perkins, 1998), where n = order of diffraction (an integer); λ = wavelength of the X-rays; d_{hkl} = interplanar lattice spacing in the crystal; and θ = angle between the diffracted ray and the planes of the crystal off of which the X-rays are diffracting (Figure1-4). The diffracted beam is only detected when constructive interference of the X-rays occurs, and Bragg's law is satisfied. The locations in which the diffracted beam is detected can be used to determine the lattice spacings of the crystal, which are indicative of the crystal structure, and can be used to identify the mineral. One can gather information about the amount of uniform strain in the structure (tension or compression), through shifts in the location of the diffraction peaks (macrostrain), or non-uniform strain (bending), through broadening of the peaks around the original position (microstrain) (Jenkins and Snyder, 1996).

In conventional X-ray diffraction, the incident X-ray beam strikes many different orientations of the sample, in order to maximize the number of *d*-spacings that will satisfy Bragg's law and generate diffracted rays. This is traditionally accomplished by powdering the sample, and allowing the incident beam to interact with a random distribution of crystallites (Perkins, 1998). With *micro*-X-ray diffraction, however, the size of the beam and the geometry of the machine allows for *in-situ* examination of

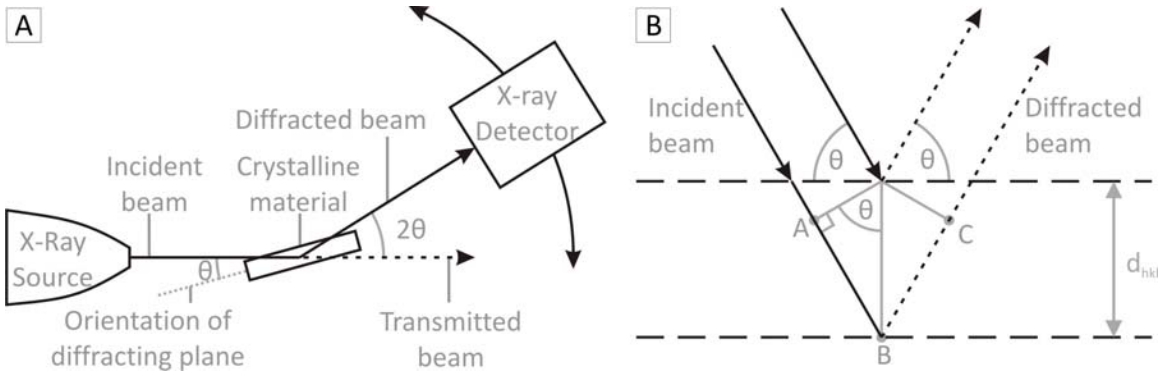

Figure 1-4: A) Geometry of an X-ray diffractometer indicating the X-ray source, the crystal, and the X-ray detector. B) A schematic of the conditions required for satisfying Bragg's Law: $n\lambda=2d\sin\theta$, where $n\lambda=AB+BC$. Modified from Perkins (1998).

crystals, by rotating the source and the detector through various angles, while leaving the crystal stationary. This effectively simulates rotating the crystal, and allows the incident beam to interact with multiple families of planes with d_{hkl} in order to satisfy Bragg's law (Flemming, 2007). As an *in-situ* technique, μXRD has immense value over destructive techniques (such as powder XRD) for examining precious planetary materials.

1.6 Sample Suites

1.6.1 Mistastin Lake impact structure

The Mistastin Lake impact structure derives its name from the local Innu name for the large hill on the west side of the lake, called Discovery Hill by English-speaking explorers, but known to the Innu as Kamestastin, which roughly translates to "the place where the wind blows very hard and never stops". The impact structure is located in central Labrador, Canada (55°53'N; 63°18'W) (Figure 1-5) and is comprised of an oval-shaped lake located in a large depression that is enclosed by a ring of hills approximately 28 km in diameter – generally regarded as being the remnant apparent crater rim (Grieve, 2006).

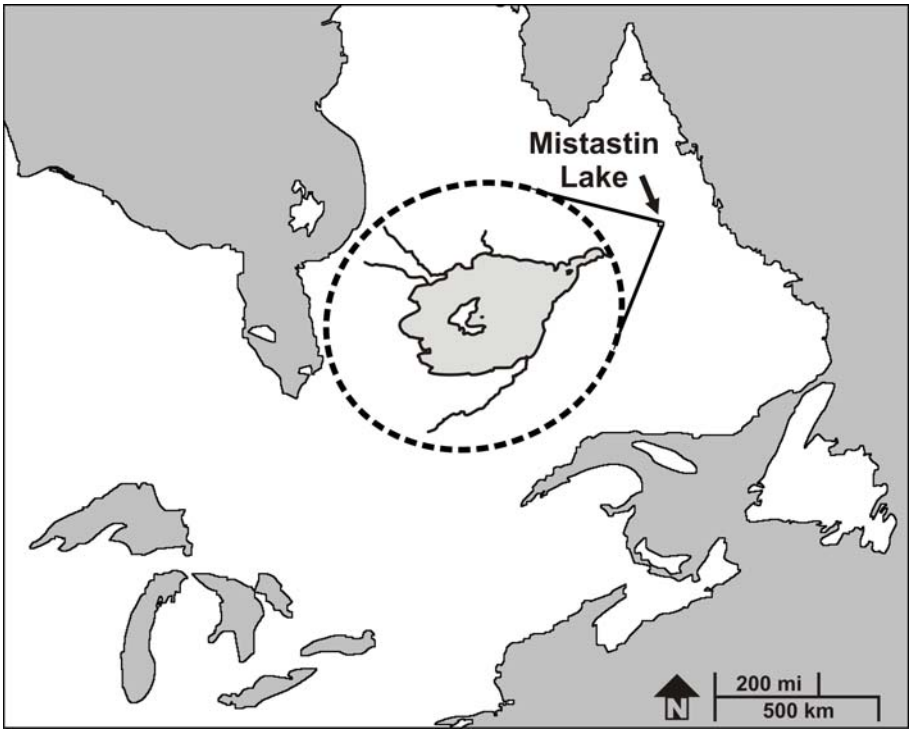

Figure 1-5: Location of the Mistastin Lake impact structure, Labrador; Canada (55°53'N; 63°18'W). Inset shows schematic map of Mistastin Lake. Hudson Bay, the Great Lakes, and Newfoundland are included for context (author's adaptation from Google Earth).

There is a horseshoe-shaped island near the centre of the lake, which is interpreted as being the central uplift of the complex crater structure. Topographic similarities to other impact structures suggested a meteorite impact origin (Taylor and Dence, 1969), which was subsequently confirmed by the discovery of shock metamorphosed rocks and minerals including planar deformation features (PDFs) in quartz and feldspar, diaplectic feldspar glasses, and poorly developed shatter cones (Taylor and Dence, 1969). Whole rock isotopic age dating techniques using $^{40}Ar/^{39}Ar$ methods using the updated decay constants of Steiger and Jäger (1977), have given the Mistastin Lake impact structure an age of 36 ± 4 Ma (Mak et al., 1976). In 2013, new age data using (U-Th)/He thermochronology reported an age of 32.7 ± 1.2 Ma (Young et al., 2013).

The Mistastin structure is located within the Mistastin Lake batholith, a part of the Canadian shield, composed of three main lithologies: anorthosite, granodiorite, and mangerite – a pyroxene-rich quartz monzonite (Currie, 1971; Emslie et al., 1980). The presence of anorthosite in the target rock makes the Mistastin Lake impact structure interesting in a planetary context, because anorthosite is also the main constituent of the Moon's highland crust.

1.6.2 Apollo Landing sites

The Moon is widely believed to have formed when a large (approximately Mars-sized) object collided with the Earth ejecting large amounts of material which, while caught in orbit of Earth, re-accreted to form the Moon (Shearer et al., 2006). Due to the observed geochemical characteristics of the Moon, it is believed that the majority of the lunar forming material came from the outer portions of the impactor and the outer portions of Earth. The immense heat generated by this event caused large-scale melting, and the development of a magma ocean on the Moon. This, in turn, resulted in the least dense minerals floating to the surface and solidifying as a plagioclase-rich crust (Hiesinger and Head, 2006). During the subsequent several hundred million years, the Moon was greatly affected by the heavy bombardment, in which it was repeatedly impacted by numerous projectiles, causing large scale melting, release of subsurface material, and the heavily cratered surface we are familiar with today (Ryder, 2002; Ryder et al., 2000; Stöffler et al., 2006).

Samples were returned from the surface of the Moon by six manned Apollo missions (381.7 kg), and three robotic Luna missions (276 g). Lunar materials have been classified into four groups based on texture and chemical composition: 1) pristine highland rocks – not affected by impact mixing; 2) pristine basaltic volcanic rocks; 3) polymict clastic breccias, impact melt rocks, and granulitic breccias; and 4) lunar regolith (Hiesinger and Head, 2006). Most highland rocks have ages of 4.5-4.17 Ga (Taylor et al., 1993).

1.7 Concluding remarks and thesis objectives

Significant research has been conducted on shock effects in feldspars over the past 50 plus years but several major questions still remain due to the optical complexity of the crystal structure and the comparatively rapid rate at which feldspars weather, making them difficult to study using traditional optical techniques. As a result, feldspar is often ignored in favour of quartz for use in determining shock level. This has resulted in a limited, purely qualitative, shock scale for feldspar despite some studies having suggested that feldspar can be just as useful as quartz, especially when studying rocks that contain little or no quartz such as anorthosite, a dominant rock type on Earth's moon. There are three particular areas which require further investigation: 1) the exact nature and formation mechanism of diaplectic glass; 2) the formation of planar deformation features and the reason why they form predominantly in tectosilicates, and within that group more-so in quartz than feldspar; and 3) which techniques are the most informative when analyzing shock in feldspar.

The purpose of this study is to contribute to the above questions by a) developing a more quantitative scale of shock deformation in feldspar group minerals; b) expanding the utility of feldspar for determining shock level in quartz-limited systems; and c) determining the effectiveness of micro-X-ray diffraction as a technique with which to evaluate shock in feldspars.

1.8 Thesis structure

Chapter 1 presents an overview of impact crater formation, morphology, and products, with particular focus on the effects of shock metamorphism, and the importance of impact cratering as a process on rocky planetary bodies. Next, a summary of the work done specifically on shock metamorphosed feldspars, particularly those shock features that behave uniquely in feldspars, including an overview of the main techniques which are currently being used to evaluate shock level in feldspars. It concludes with an introduction to micro-X-ray diffraction and an overview of the geological setting of the

two sample suites: the Mistastin Lake impact structure and the Apollo landing sites. And finally, it makes clear the thesis objectives, and outlines the structure of the thesis.

Chapter 2 is a presentation of the shocked plagioclase feldspars from the Mistastin Lake impact structure, using mainly optical and scanning electron microscopy of polished thin sections. It discusses the formation of planar elements in plagioclase, the nature of diaplectic feldspar glass, and the results of post-impact alteration of shock-induced products.

Chapter 3 focuses on how shock metamorphism affects micro-X-ray diffraction (μXRD) patterns of lunar and terrestrial plagioclase, by incorporating samples returned from Earth's moon during the Apollo missions and comparing them to the Mistastin Lake samples. Measuring strain-related mosaicity using *in situ* micro-X-ray diffraction of shocked materials has been successfully applied to other minerals but is applied to plagioclase for the first time in this chapter. Combining optical and μXRD observations will enable measurement of strain in the crystal structure, and correlation with optically determined shock level.

Chapter 4 ties Chapters 2 and 3 together and relates the new observations presented therein to the previous work done in this field and summarized in Chapter 1. It also presents suggestions for future work, and the further development of μXRD as a technique for quantifying shock level in plagioclase.

1.9 References

Ahrens T. J., Petersen C. F., and Rosenberg J. T. 1969. Shock compression of feldspars. *Journal of Geophysical Research* 74: 2727–2746.

Ahrens T., and O'Keefe J. 1972. Shock melting and vaporization of lunar rocks and minerals. *The Moon* 4: 214–249.

Arndt J., Hummel W., and Gonzalez-Cabeza I. 1982. Diaplectic labradorite glass from the Manicouagan impact crater; I, Physical properties, crystallization, structural and genetic implications. *Physics and Chemistry of Minerals* 8: 230–239.

Baratoux D., and Melosh H. J. 2003. The formation of shatter cones by shock wave interference during impacting. *Earth and Planetary Science Letters* 216: 43–54.

Binns R. A. 1967. Stony meteorites bearing maskelynite. *Nature* 213: 1111–1112.

Bunch T. E., Cohen A. J., and Dence M. R. 1967. Natural terrestrial maskelynite. *American Mineralogist* 52: 244–253.

De Carli P. S., and Jamieson J. C. 1959. Formation of an amorphous form of quartz under shock conditions. *The Journal of Chemical Physics* 31: 1675–1676.

Chao E. C. T. 1967. Impact Metamorphism. In *Researches in Geochemistry, vol. 2*, edited by Abelson P. H. New York: John Wiley & Sons, Ltd. pp. 204–233.

Chao E. C. T. 1968. Pressure and temperature histories of impact metamorphosed rocks, based on petrographic observations. In *Shock metamorphism of natural materials*, edited by French B., and Short N. M. Baltimore, MD: Mono Book Corp. pp. 135–158.

Chen M., and El Goresy A. 2000. The nature of maskelynite in shocked meteorites; not diaplectic glass but a glass quenched from shock-induced dense melt at high pressures. *Earth and Planetary Science Letters* 179: 489–502.

Currie K. L. 1971. Geology of the resurgent cryptoexplosion crater at Mistastin Lake, Labrador. *Bulletin - Geological Survey of Canada* 207: 62.

Dachille F., Gigl P., and Simons P. Y. 1968. Experimental and analytical studies of crystalline damage useful for the recognition of impact structures. In *Shock metamorphism of natural materials*, edited by French B. M., and Short N. M. Baltimore, MD: Mono Book Corp. pp. 555–570.

Deer W. A., Howie R. A., and Zussman J. 2001.*Rock-Forming Minerals, Volume 4a: Framework Silicates - Feldspars*, 2nd ed. London: The Geological Society. 972 p.

Dietz R. S. 1960. Meteorite impact suggested by shatter cones in rock. *Science* 131: 1781–1784.

Dietz R. S. 1947. Meteorite impact suggested by the orientation of shatter-cones at the Kentland, Indiana, disturbance. *Science* 105: 42–43.

Dietz R. S. 1959. Shatter cones in cryptoexplosion structures (meteorite impact?). *Journal of Geology* 67: 496–505.

Emslie R. F., Cousens B., Hamblin C., and Bielecki J. 1980. The Mistastin batholith, Labrador-Quebec: an Elsonian composite Rapakivi suite. *Current Research, Part A, Geological Survey of Canada, Paper 80-1 A* 95–100.

Engelhardt W. von. 1990. Distribution, petrography and shock metamorphism of the ejecta of the Ries Crater in Germany - a review. *Tectonophysics* 171: 259–273.

Engelhardt W. von, Arndt J., Stöffler D., Muller W. F., Jeziorkowski H., and Gubser R. 1967. Diaplektische Gläser in den Breccien des Ries yon Nördlingen als Anzeichen fiir Stosswellenmetamorphose. *Contributions to Mineralogy and Petrology* 15: 93–102.

Engelhardt W. von, and Bertsch W. 1969. Shock induced planar deformation structures in quartz from the ries crater, Germany. *Contributions to Mineralogy and Petrology* 21: 378.

Engelhardt W. von, and Stöffler D. 1968. Stages of shock metamorphism in crystalline rocks of the Ries Basin, Germany. In *Shock metamorphism of natural materials*, edited by French B. M., and Short N. M. Baltimore, MD: Mono Book Corp. pp. 159–168.

Ferrière L., and Osinski G. R. 2013. Shock Metamorphism. In *Impact Cratering: Processes and Products*, edited by Osinski G. R., and Pierazzo E. Wiley-Blackwell. pp. 106–124.

Flemming R. L. 2007. Micro X-ray diffraction (μXRD); a versatile technique for charcterization of Earth and planetary materials. *Canadian Journal of Earth Sciences* 44: 1333–1346.

French B. M. 1998. *Traces of catastrophe, a handbook of shock-metamorphic effects in terrestrial meteorite impact structures*, Houston, TX, United States (USA): Lunar and Planetary Institute, Houston, TX. 120 p.

French B. M., and Koeberl C. 2010. The convincing identification of terrestrial meteorite impact structures: What works, what doesn't, and why. *Earth-Science Reviews* 98: 123–170.

French B. M., and Short N. M. (ed). 1968. *Shock Metamorphism of Natural Materials*, edited by French B. M., and Short N. M. Baltimore: Mono Book Corp. 644 p.

Fritz J., and Greshake A. 2009. High-pressure phases in an ultramafic rock from Mars. *Earth and Planetary Science Letters* 288: 619–623.

Fritz J., Greshake A., and Stöffler D. 2005. Micro-Raman spectroscopy of plagioclase and maskelynite in Martian meteorites: Evidence of progressive shock metamorphism. *Antarctic Meteorite Research* 18: 96–116.

Gault D. E., Quaide W. L., and Oberbeck V. R. 1968. Impact Cratering Mechanics and Structures. In *Shock Metamorphism of Natural Materials*, edited by French B. M., and Short N. M. Baltimore, MD: Mono Book Corp. pp. 87–99.

Gillet P., Chen M., Dubrovinsky L., and El Goresy A. 2000. Natural $NaAlSi_3O_8$-hollandite in the shocked sixiangkou meteorite. *Science (New York, N.Y.)* 287: 1633–6.

El Goresy A., Chen M., Gillet P., and Dubrovinsky L. S. 2000. Shock-induced high-pressure phase-transition of labradorite to hollandite "(Na_{47}-Ca_{51}-K_2)" in Zagami and the assemblage hollandite "(Na_{80}-Ca_{12}-K_8)" + jadeite in L chondrites: constraints to peak-shock pressures edited by Sears D. W. G. et al. *Meteoritics & Planetary Science* 35: A51–A51.

Grady D. E. 1977. Processes occurring in shock wave compression of rocks and minerals. In *High-pressure research: Applications in Geophysics*, edited by Manghnani M. H., and Akimoto S. I. New York: Academic Press. pp. 389–438.

Grady D. E. 1980. Shock deformation of brittle solids. *Journal of Geophysical Research* 85: 913–924.

Grady D. E., Murri W. J., and De Carli P. S. 1975. Hugoniot sound velocities and phase transformations in two silicates. *Journal of Geophysical Research* 80: 4857–4861.

Grieve R. A. F. 2006. *Impact Structures in Canada*, Geological Association of Canada. 210 p.

Grieve R. A. F., Dence M. R., and Robertson P. B. 1977. Cratering processes: As interpreted from the occurrence of impact melts. In *Impact and Explosion Cratering*, edited by Roddy D. J., Pepin R. O., and Merrill R. B. New York: Pergamon Press. pp. 791–814.

Hiesinger H., and Head J. W. 2006. New views of lunar geoscience: an introduction and overview. *Reviews in Mineralogy and Geochemistry* 60: 1–81.

Hörz F., and Quaide W. L. 1973. Debye-Scherrer investigations of experimentally shocked silicates. *The Moon* 6: 45–82.

Izawa M. R. M., Flemming R. L., Banerjee N. R., and McCausland P. J. A. 2011. Micro-X-ray diffraction assessment of shock stage in enstatite chondrites. *Meteoritics & Planetary Science* 46: 638–651.

Jaret S., Kah L. C., and French B. M. 2009. Feldspar deformation as an indicator of low-barometry shock: petrographic investigation of ejecta from the Tenoumer impact crater, Mauritania. In *Geological Society of America Abstracts with Programs*. p. 313.

Jenkins R., and Snyder R. L. 1996.*Introduction to X-Ray Powder Diffraction*, New York: John Wiley & Sons, Ltd. 403 p.

Johnson J. R., Hörz F., Lucey P. G., and Christensen P. R. 2002. Thermal infrared spectroscopy of experimentally shocked anorthosite and pyroxenite; implications for remote sensing of Mars. *Journal of Geophysical Research* 107: 14.

Johnson J. R., Hörz F., and Staid M. I. 2003. Thermal infrared spectroscopy and modeling of experimentally shocked plagioclase feldspars. *American Mineralogist* 88: 1575–1582.

Kayama M., Nishido H., Sekine T., Nakazato T., Gucsik A., and Ninagawa K. 2012. Shock barometer using cathodoluminescence of alkali feldspar. *Journal of Geophysical Research* 117: E09004.

Lambert P. 1979. Fractures induced by shock in quartz and feldspar. *Mineralogical Magazine* 43: 527–533.

Langenhorst F. 2002. Shock metamorphism of some minerals: Basic introduction and microstructural observations. *Bulletin of the Czech Geological Survey* 77: 265–282.

Langenhorst F., and Dressler B. 2003. First observation of silicate hollandite in a terrestrial rock. *LPI Contribution* 1167: 0–Abstract 4046.

Langenhorst F., and Poirier J.-P. 2000. Anatomy of black veins in Zagami; clues to the formation of high-pressure phases. *Earth and Planetary Science Letters* 184: 37–55.

Liu L.-G. 1978. High-pressure phase transformations of albite, jadeite and nepheline. *Earth and Planetary Science Letters* 37: 438–444.

Lyon R. J. P. 1963. Evaluation of infrared spectrophotometry for compositional analysis of lunar and planetary soils. *NASA Technical Note D-1871*.

Mak E., York D., Grieve R. A. F., and Dence M. 1976. The age of the Mistastin Lake crater, Labrador, Canada. *Earth and Planetary Science Letters* 31: 345–357.

McCausland P. J. A., Flemming R. L., and Izawa M. R. M. 2010. Quantitative shock stage assessment in olivine and pyroxene bearing meteorites via in situ micro-XRD. In *American Geophysical Union, Fall Meeting 2010, abstract #P14C-03*.

Melosh H. J. 1989. *Impact Cratering: A Geologic Process*, New York: Oxford University Press. 245 p.

Melosh H. J., and Ivanov B. A. 1999. Impact crater collapse. *Annual Review of Earth and Planetary Sciences* 27: 385–415.

Milton D. J. 1977. Shatter cones; an outstanding problem in shock mechanics. In *Impact and Explosion Cratering*, edited by Roddy D. J., Pepin R. O., and Merrill R. B. New York: Pergamon Press. pp. 703–714.

Moser D. E., Davis W. J., Reddy S. M., Flemming R. L., and Hart R. J. 2009. Zircon U–Pb strain chronometry reveals deep impact-triggered flow. *Earth and Planetary Science Letters* 277: 73–79.

Nesse W. D. 2004. *Introduction to Optical Mineralogy*, 3rd ed. New York: Oxford University Press. 348 p.

Oberbeck V. R. 1975. The role of ballistic erosion and sedimentation in lunar stratigraphy. *Reviews of Geophysics* 13: 337–362.

Ohtani E., Kimura Y., Kimura M., Takata T., Kondo T., and Kubo T. 2004. Formation of high-pressure minerals in shocked L6 chondrite Yamato 791384: constraints on shock conditions and parent body size. *Earth and Planetary Science Letters* 227: 505–515.

Osinski G. R., and Pierazzo E., eds. 2013. *Impact Cratering: Processes and Products*, Wiley-Blackwell. 316 p.

Osinski G. R., Tornabene L. L., and Grieve R. A. F. 2011. Impact ejecta emplacement on terrestrial planets. *Earth and Planetary Science Letters* 310: 167–181.

Ostertag R. 1983. Shock experiments on feldspar crystals. *Journal of Geophysical Research* 88, Suppl.: B364–B376.

Perkins D. 1998.*Mineralogy*, Toronto: Prentice-Hall Inc. 484 p.

Poelchau M. H., and Kenkmann T. 2011. Feather features; a low-shock-pressure indicator in quartz. *Journal of Geophysical Research* 116: B02201.

Poldervaart A., and Gilkey A. K. 1954. On clouded plagioclase. *American Mineralogist* 35: 75–91.

Reynard B., Okuno M., Shimada Y., Syono Y., and Willaime C. 1999. A Raman spectroscopic study of shock-wave densification of anorthite ($CaAl_2Si_2O_8$) glass. *Physics and Chemistry of Minerals* 26: 432–436.

Ringwood A. E., Reid A. F., and Wadsley A. D. 1967. High pressure transformation of alkali aluminosilicates and aluminogermanates. *Earth and Planetary Science Letters* 3: 38–40.

Roddy D. J., Pepin R. O., and Merrill R. B., eds. 1978. *Impact and Explosion Cratering*, Toronto: Pergamon Press. 1301 p.

Ryder G. 2002. Mass flux in the ancient Earth-moon system and benign implications for the origin of life on Earth. *Journal of Geophysical Research. E. Planets* 107: 6–14.

Ryder G., Koeberl C., and Mojzsis S. J. 2000. Heavy bombardment of the Earth at approximately 3.85 Ga; the search for petrographic and geochemical evidence. In *Origin of the Earth and Moon*, edited by Canup R. M., and Righter K. Tucson: University of Arizona Press. pp. 475–492.

Shearer C. K. et al. 2006. Thermal and magmatic evolution of the Moon. *Reviews in Mineralogy and Geochemistry* 60: 365–518.

Singleton A. C., Osinski G. R., McCausland P. J. A., and Moser D. E. 2011. Shock-induced changes in density and porosity in shock-metamorphosed crystalline rocks, Haughton impact structure, Canada. *Meteoritics & Planetary Science* 46: 1774–1786.

Smith J. V, and Brown W. L. 1988. *Feldspar Minerals*, 2nd ed. Berlin: Springer-Verlag. 828 p.

Spry A. H. 1969. *Metamorphic textures*, Oxford, New York: Pergamon Press. 350 p.

Stähle V. 1973. Cordierite glass formed by shock in a cordierite-garnet-gneiss from the Ries crater, Germany. *Earth and Planetary Science Letters* 18: 385–390.

Steiger R. H., and Jäger E. 1977. Subcommission on geochronology: convention on the use of decay constants in geo- and cosmochronology. *Earth and Planetary Science Letters* 36: 359–362.

Stöffler D. 1972. Deformation and transformation of rock-forming minerals by natural and experimental shock processes: I. Behavior of minerals under shock compression. *Fortschritte der Mineralogie* 49: 50–113.

Stöffler D. 1974. Deformation and transformation of rock-forming minerals by natural and experimental shock processes: II. Physical properties of shocked minerals. *Fortschritte der Mineralogie* 51: 256–289.

Stöffler D. 1967. Deformation und Umwandlung von Plagioklas durch Stoßwellen in den Gesteinen des Nördlinger Ries. *Contributions to Mineralogy and Petrology* 16: 51–83.

Stöffler D. 1971. Progressive metamorphism and classification of shocked and brecciated crystalline rocks at impact craters. *Journal of Geophysical Research* 76: 5541–5551.

Stöffler D. 1966. Zones of impact metamorphism in the crystalline rocks of the Nördlinger Ries crater. *Contributions to Mineralogy and Petrology* 12: 15–24.

Stöffler D., and Grieve R. A. F. 2007. Impactites. In *Metamorphic Rocks: A Classification and Glossary of Terms, Recommendations of the International Union of Geological Sciences*, edited by Fettes D., and Desmons J. Cambridge, UK: Cambridge University Press. pp. 82–92, and 111–242.

Stöffler D., and Hornemann U. 1972. Quartz and feldspar glasses produced by natural and experimental shock. *Meteoritics* 7: 371–394.

Stöffler D., and Langenhorst F. 1994. Shock metamorphism of quartz in nature and experiment : I . Basic observation and theory. *Meteoritics* 29: 155–181.

Stöffler D., Ryder G., Ivanov B. A., Artemieva N. A., Cintala M. J., and Grieve R. A. F. 2006. Cratering history and lunar chronology. *Reviews in Mineralogy and Geochemistry* 60: 519–596.

Taylor F. C., and Dence M. R. 1969. A probable meteorite origin for Mistastin Lake, Labrador. *Canadian Journal of Earth Sciences* 6: 39–45.

Taylor S. R., Norman M. D., Esat T., King T. V. V, and Ridley I. 1993. The lunar highland crust; the origin of the Mg suite. *Meteoritics* 28: 448.

Tomioka N., Mori H., and Fujino K. 2000. Shock-induced transition of $NaAlSi_30_8$ feldspar into a hollandite structure in a L6 chondrite. *Geophysical Research Letters* 27: 3997–4000.

Tschermak G. 1883. Beitrag zur Classification der Meteoriten. *Sitzungsberichte der Mathematisch-Naturwissenschaftlichen Klasse der Kaiserlichen Akademie der Wissenschaften, Wien* 88: 347–371.

Tschermak G. 1872. Die Meteoriten von Shergotty und Gopalpur. *Sitzungsberichte der Mathematisch-Naturwissenschaftlichen Klasse der Kaiserlichen Akademie der Wissenschaften, Wien* 65: 122–145.

Vinet N., Flemming R. L., and Higgins M. D. 2011. Crystal structure, mosaicity, and strain analysis of Hawaiian olivines using in situ X-ray diffraction. *American Mineralogist* 96: 486–497.

Walawender M. J. 1977. Shock-produced mosaicism in plagioclase, Charlevoix Structure, Quebec. *Canadian Journal of Earth Sciences = Revue Canadienne des Sciences de la Terre* 14: 74–81.

Whitney P. R. 1972. Spinel inclusions in plagioclase of metagabbros from the Adirondack Highlands. *American Mineralogist* 57: 1429–1436.

Yagi A., Suzuki T., and Akaogi M. 1994. High pressure transitions in the system KAlSi3O8-NaAlSi3O8. *Physics and Chemistry of Minerals* 21: 12–17.

Young K. E., Hodges K. V, van Soest M. C., and Osinski G. R. 2013. Dating the Mistastin Lake impact structure, Labrador, Canada, using zircon (U-Th)/He thermochronology. In *44th Lunar and Planetary Science Conference*.

Zoltai T., and Stout J. H. 1984. *Mineralogy: concepts and principles*, Minneapolis: Burgess Publishing Company. 505 p.

Chapter 2

2 Shock Effects in Plagioclase Feldspar from the Mistastin Lake Impact Structure

Annemarie E. Pickersgill, Gordon R. Osinski, and Roberta L. Flemming

2.1 Introduction

Meteorite impact craters are a dominant surface feature on most terrestrial planetary bodies. Their formation includes the excavation of large amounts of subsurface material, thereby providing important information about the interior, surfaces, and histories of the planets on which they form. The temperatures and pressures that result from crater-forming hypervelocity impact are well above those observed in endogenic geologic processes. As the shockwave generated by impact passes through the target material, lithic and mineral fragments are deformed in characteristic ways resulting in diagnostic shock metamorphic effects (French and Koeberl, 2010).

On the microscopic scale, shock metamorphic effects include planar deformation features (PDFs), high pressure-polymorphs, and diaplectic glass (Engelhardt and Stöffler, 1968; French and Koeberl, 2010; Ostertag, 1983; Stöffler and Hornemann, 1972; Stöffler, 1971, 1966). Planar microstructures are most commonly observed in quartz, but have also been observed in other minerals such as feldspars, sillimanite, cordierite, garnet, apatite, and, zircon (e.g., Bohor et al., 1993; Dressler, 1990; Dworak, 1969; Ferrière et al., 2009; Stöffler, 1974, 1972; Wittmann et al., 2006). Planar features in other minerals are less well studied than those in quartz, due to variations in crystal structure, which results in a greater variation in the types of planar features formed (French and Koeberl, 2010). Diaplectic quartz and feldspar glasses are formed at higher temperatures and pressures than planar microstructures and are unique from monomineralic melt glasses in that they become optically isotropic and produce amorphous X-ray patterns but maintain the external morphology and internal texture (inclusions, etc.) of the original crystal (Chao, 1967; Engelhardt and Stöffler, 1968). The term *maskelynite* is often used interchangeably

with *diaplectic feldspar glass*, however, observations of flow in maskelynite in meteorites (e.g., Chen and El Goresy, 2000), and poorly defined usage of the term over the past century, has brought the definition of maskelynite into question. When maskelynite was first described, it was interpreted as an unknown, isotropic mineral of near labradorite composition (Tschermak, 1872), and later as a monomineralic glass of near labradorite composition (Tschermak, 1883). It was Binns (1967), who first suggested that it had a shock origin and noted differences in refractive index from normal fused glass. Since then, the meaning of the term maskelynite has become ambiguous, therefore, we do not use the term maskelynite further in this paper. Instead, we refer to monomineralic shock-amorphized material, which shows no signs of flow, as diaplectic feldspar glass. As well as the aforementioned shock effects, which are exclusive to impact, features such as undulose extinction, fracturing, and optical mosaicism, which can also be derived from endogenic processes, are indicative of non-uniform strain caused by passage of the shockwave.

Thus far, studies of shock effects in feldspar group minerals have been limited due to the optical complexity of the crystal structure and the comparatively rapid rate at which feldspars weather, making them difficult to study using conventional optical techniques. As a result, feldspar is often ignored in favour of quartz for use as a shock barometer. This has resulted in a limited, purely qualitative, shock scale for feldspar (see Table 2-1) (e.g., Lambert, 1979; Ostertag and Jessberger, 1982; Ostertag, 1983; Stöffler, 1966; Stöffler et al., 1991), despite some studies having suggested that feldspar can be just as useful as quartz (e.g., Jaret et al., 2009; Kayama et al., 2012). An understanding of shock effects in feldspars is vital for planetary studies, which deal with quartz-poor, often feldspar-rich, systems.

This investigation of shock effects in plagioclase feldspar is motivated by the dominance of plagioclase in the anorthositic lunar highlands. This contribution will address solid state shock-related deformation of feldspars at the Mistastin Lake impact structure, Labrador, a unique lunar analogue site with anorthosite target rocks. This forms part of a larger project that is aimed at developing a more quantitative scale of shock deformation

Table 2-1: A summary of shock effects in plagioclase feldspar according to the three main schemes. Stöffler (1971) and Singleton et al. (2011) are based on studies of terrestrial shocked rocks. Stöffler et al. (1991) is based on classification of ordinary chondrites.

Stöffler (1971)			Stöffler et al. (1991)			Singleton et al. (2011)		
Shock stage	Shock effects	Pressure (GPa)	Shock Stage	Shock effects	Pressure (GPa)	Shock level	Shock effects	Pressure (GPa)
0	Fractured		*S1* Unshocked	Sharp optical extinction, irregular fractures	<4-5	0		0
						1		2-5
			S2 Very weakly shocked	Undulose extinction, irregular fractures		2	Fracturing checkerboard	5-10
		10			5-10			
I	Diaplectic feldspar (shocked, but not yet amorphous)		*S3* Weakly shocked	Undulose extinction		3	PDFs, checkerboard	10-20
							PDFs, reduced refractive index, lower birefringence, checkerboard	20-30
			S4 Moderately shocked	Undulose extinction, partially isotropic, PDFs	15-20			
						4	PDFs	30-35
		35			30-35			
II	Diaplectic feldspar glass		*S5* Strongly shocked	Maskelynite		5	Diaplectic to flowed and vesicular, partial melting, normal (melted) glass	35-45
							Diaplectic to flowed and vesicular, partial melting	45-55
		45			45-55			
III	Fused feldspar (vesiculated glass)		*S6* Very strongly shocked	Shock melted (normal glass) restricted to local regions in or near melt zones		6	Flowed to frothy glass, partial melting	55-60
		55-60						
IV	Inhomogeneous rock glasses					7	Complete melting of all minerals, frothy siliceous, and minor mafic glasses	60-80
		>80			75-90			
V	Silicate vapour		Shock melted	Whole rock melting		8	Complete rock vaporization	>80

in feldspar group minerals and thereby expanding the utility of feldspar for determining shock level in quartz-limited systems (e.g., anorthosite, many mafic rocks, and meteorites); and for determining which technique(s) are the most effective in evaluating shock in feldspars.

2.2 Geological setting of the Mistastin Lake impact structure

The Mistastin Lake impact structure, known locally as Kamestastin, located in central Labrador, Canada (55°53'N; 63°18'W), is comprised of an oval-shaped lake located in a large depression that is enclosed by a ring of hills approximately 28 km in diameter – generally regarded as being the remnant apparent crater rim (Grieve, 2006). There is a horseshoe shaped island near the centre of the lake, which is interpreted as being the central uplift of the complex crater structure. Topographic similarities to other impact structures suggested a meteorite impact origin (Taylor and Dence, 1969), which was subsequently confirmed by the discovery of shock metamorphosed rocks and minerals including quartz and feldspar exhibiting planar deformation features (PDFs), diaplectic quartz and feldspar glasses, and poorly developed shatter cones (Taylor and Dence, 1969). Whole rock isotopic age dating techniques using $^{40}Ar/^{39}Ar$ methods using the updated decay constants of Steiger and Jäger (1977), have given the Mistastin Lake impact structure an age of 36 ± 4 Ma (Mak et al., 1976). Recently, a new age estimate using (U-Th)/He thermochronology of 32.7 ± 1.2 Ma has been reported (Young et al., 2013).

The Mistastin Lake impact structure is located within the Mistastin Lake batholith, a part of the Canadian shield, composed of three main lithologies: anorthosite, granodiorite, and mangerite – a pyroxene rich quartz monzonite (Figure 2-1) (Currie, 1971; Emslie and Stirling, 1993). The presence of anorthosite in the target rock makes the Mistastin Lake impact structure a useful planetary analogue because anorthosite is also the main constituent of the lunar highlands crust.

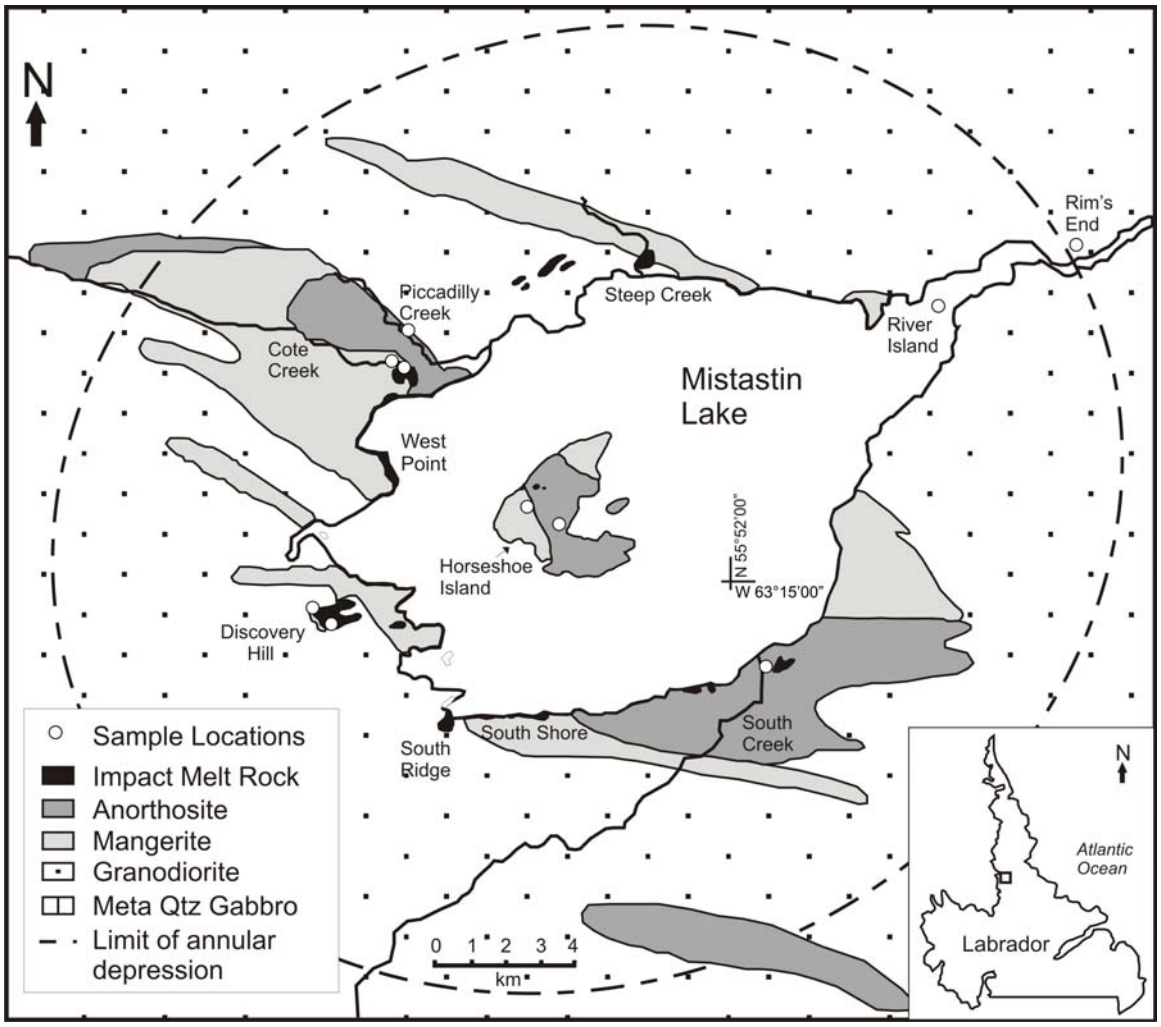

Figure 2-1: A simplified geological map of the Mistastin Lake impact structure showing three main target lithologies (anorthosite, granodiorite, and mangerite). The dashed line indicates the apparent crater rim according to Grieve (1975). Samples for this study were taken from various locations and lithologies around the crater as indicated by white dots; for simplicity, samples from the same area are grouped together (i.e., the number of dots is not representative of the number of samples). Geographic locations of note are labeled and correlate with those in Table 2-2 and Appendix A. Modified from Marion and Sylvester (2010).

Taylor and Dence (1969) report strong irregular fracturing in all minerals and the development of several sets of planar features in quartz and feldspar. Rocks of the central uplift have undergone weak to moderate shock metamorphism and the quartz-monzonite on the shoreline has been weakly shocked, before being thermally metamorphosed by the nearby melt rocks. Inclusions within the melt rocks are reported to display various levels of shock (Taylor and Dence, 1969). In feldspars, Taylor and Dence (1969) note the local development of 1 to 3 sets of planar features and a slight to moderate hydrothermal alteration that has affected the feldspars post-shock. They also report no planar features in the feldspars from the monzonite on the western shore.

2.3 Methods and samples

Samples of shocked feldspar-bearing lithologies were collected over the course of two field seasons by M. Mader, A. Singleton, and A. Pickersgill (2010 and 2011) at the Mistastin structure, from a range of locations throughout the crater: the central uplift, the crater floor, ejecta deposits, terraces, and the rim (Figure 2-1, Table 2-2, Appendix A) – with the intent of obtaining a wide range of shock levels and, therefore, a diverse sampling of shock metamorphic effects. Additional samples for this project were collected during the 2009 field season by M. Mader and R. Dammeier. The majority of samples in this study come from anorthosite target rock or monomict anorthosite breccia; some are individual mineral grains in polymict lithic and melt-bearing breccias, and some are from the granodiorite or pyroxene-rich quartz monzonite that make up the remainder of the three main target rocks.

Polished thin sections were examined for microscopic shock metamorphic effects, using a Nikon Eclipse LV100POL compound petrographic microscope. Follow up work on microtextures was conducted using a Zeiss 1540XB FIB/SEM at the Nanofabrication Laboratory at The University of Western Ontario. Quantitative chemical composition and cathodoluminescence data were collected using a JXA-8530F Field Emission Electron Probe Microanalyzer (FE-EPMA) in the Earth and Planetary Materials Analysis Laboratory. Beam operating conditions were an accelerating voltage of 10 kV-15 kV,

probe current of 20 nA, and a beam diameter of <5 μm. Mineral calibration standards used for wavelength dispersive spectrometry (WDS) analyses were as follows: Albite (CM Taylor) for Na and Si, Orthoclase (CM Taylor) for Si and K, and Anorthite (Smithsonian USNM 137041 - Great Sitkin Island, AL) for Al and Ca.

Mineral identification by micro-X-ray diffraction was carried out on a Bruker D8 Discover diffractometer with theta-theta instrument geometry. It has a sealed cobalt source, Gobel mirror parallel beam optics, a pinhole collimator (100 or 300 μm), and two-dimensional (2-D) general area detector diffraction system (GADDS). Omega scans were used, wherein the source and detector rotate simultaneously, both clockwise, through a specified number of degrees (Omega angle, ω) to simulate rotation of the sample. Counting time was 30 minutes for GADDS frame 1 (θ_1=14.5°, θ_2=16°, ω=6) and 45 minutes for GADDS frame 2 (θ_1=30°, θ_2=40°, ω=23). Observed lattice planes were indexed using ICDD cards: 01-079-1148 (C)-Andesine, and 01-083-1417 (C)-Labradorite.

2.4 Results

Anorthosite samples are dominated by plagioclase feldspar, often altered along fractures to zeolites and clays, with minor amounts of quartz, pyroxene, and sulfides. Ubiquitous small dark rod-like microlites appear along cleavage and twin planes within these feldspar grains (Figure 2-2). These grains were too small to obtain fully quantitative EPMA or μXRD analyses due to beam overlap with surrounding phases. Nevertheless, analyses of their chemical composition revealed increased Fe_2O_3, up to 100 wt% in some cases, with additional Ti and trace Mg (Appendix B, Table B-4). We have, therefore, tentatively identified them as being of the ilmenite-hematite solid solution of iron-oxides. They match in composition, habit, and orientation the microlites reported in clouded feldspars (e.g., Poldervaart and Gilkey, 1954; Whitney, 1972). Pyroxene-rich quartz monzonite (mangerite) and granodiorite samples are also dominated by plagioclase feldspar. The rocks also contain pyroxene, quartz, alteration products infilling fractures, and sulfides. All minerals in each lithology are heavily fractured and exhibit undulose

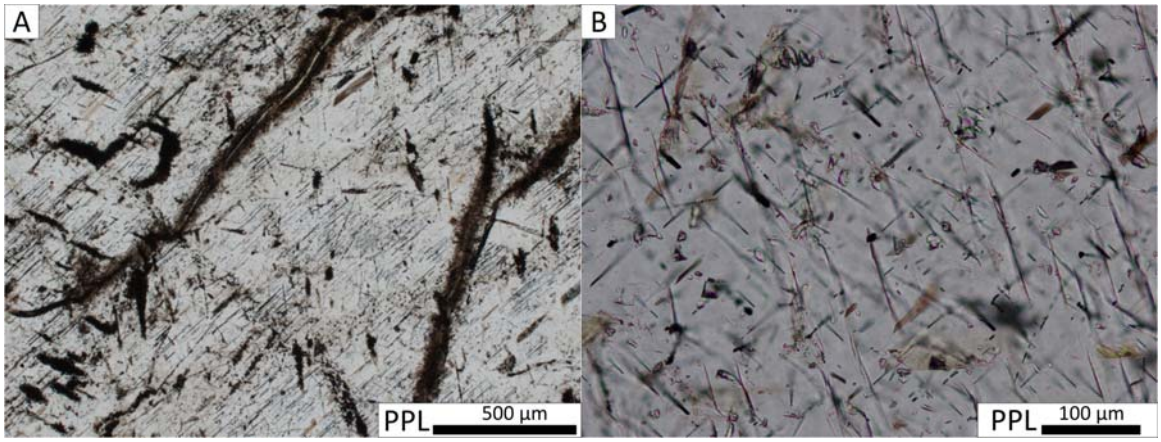

Figure 2-2: Transmitted light photomicrographs of ubiquitous Fe-oxide microlites, which pervade diaplectic plagioclase glass (A) and plagioclase crystals (B) in anorthosite samples. They appear to be aligned with crystallographic planes. When viewed at low magnification (A), they may initially be mistaken for planar deformation features but at higher magnification (B) their linearity and discontinuity throughout the grain becomes apparent.

extinction. In all three lithologies, plagioclase crystals are large (mm-size) and well formed. They exhibit well developed polysynthetic twinning and are heavily fractured throughout. Feldspars display offset twins, kinked twins, undulose extinction, partial to complete conversion to diaplectic feldspar glass, and signs of recrystallizing amorphous material. Individual plagioclase mineral clasts are common in impact breccias throughout the crater and as clasts in the impact melt rocks. Below, we outline the shock effects present in the Mistastin Lake samples. A summary of the geographic distribution of observed shock indicators can be found in Table 2-2.

Curved and kinked twins were observed in several samples from around the crater. Kinked twins resemble kink banding in biotite in that they turn sharply away from normal linear twins (Figure 2-3A, B). Evidence of this kinking is only visible in cross-polarized light. In plane polarized light, the crystals appear normal. Twins that are bent in a smoother curve are more common, and the angle through which they bend can vary

Table 2-2: Geographic distribution of Mistastin samples and their optical characteristics.

Crater location	Geographic location*	Sample Name (individual samples separated by semi-colon)	Rock type	Optical effects							
				Offset twins	Fractures	Undulose	Bent twins	PDFs (quartz)	Levyne-Ca	Diaplectic feldspar glass (partial**)	Diaplectic feldspar glass (complete)
Central uplift	Horseshoe Island	***MHI10:*** 04; 12; 17; 22; 23; 35; 51; 54; 54-2 ***MST09:*** 20; 22; 24; 25; 26	Anorthosite	x	x	x	x	x	x		
Inner terrace (under interpretation)	Coté Creek	***MM09:*** 35A, 35D, 35E ***MM10***: 05-B1; 05-B2; 05-C; 06-A2; 06-A3; 06-D2; 09-B; 10; 11; 12-2; 13-1; 13-2; 16; 17-A; 17-B; 34-A; 34-C2; 34-C5	Clast rich melt		x	x					
			Anorthosite breccia		x	x	x			x	x
			Polymict breccia		x						x
	Piccadilly Creek	***MM10:*** 20; 20-1; 20-2; 24; 25; 28; 30; 32	Anorthosite breccia	x	x	x					
	South Creek	***MM10:*** 36-B1; 36-B2; 38; 39; 40; 41-1; 42; 43; 44; 45; 46-2	Anorthosite breccia		x	x	x		x		x
Inner terrace/melt pond	Discovery Hill	***MM10:*** 01-C	Polymict breccia		x	x					
Terrace	Steep Creek	***MM09:*** 10; 32-B	Polymict breccia		x	x		x		x	x
Rim	River Island	***MM10:*** 32-A; 32-B; 33	Mangerite		x	x					
			Granodiorite		x	x					
	Rim's End	***MM10:*** 47; 48	Mangerite		x						

*These locations are indicated in Figure 2-1. For a list of sample collection coordinates see Appendix A.

**Including alternate twin isotropization.

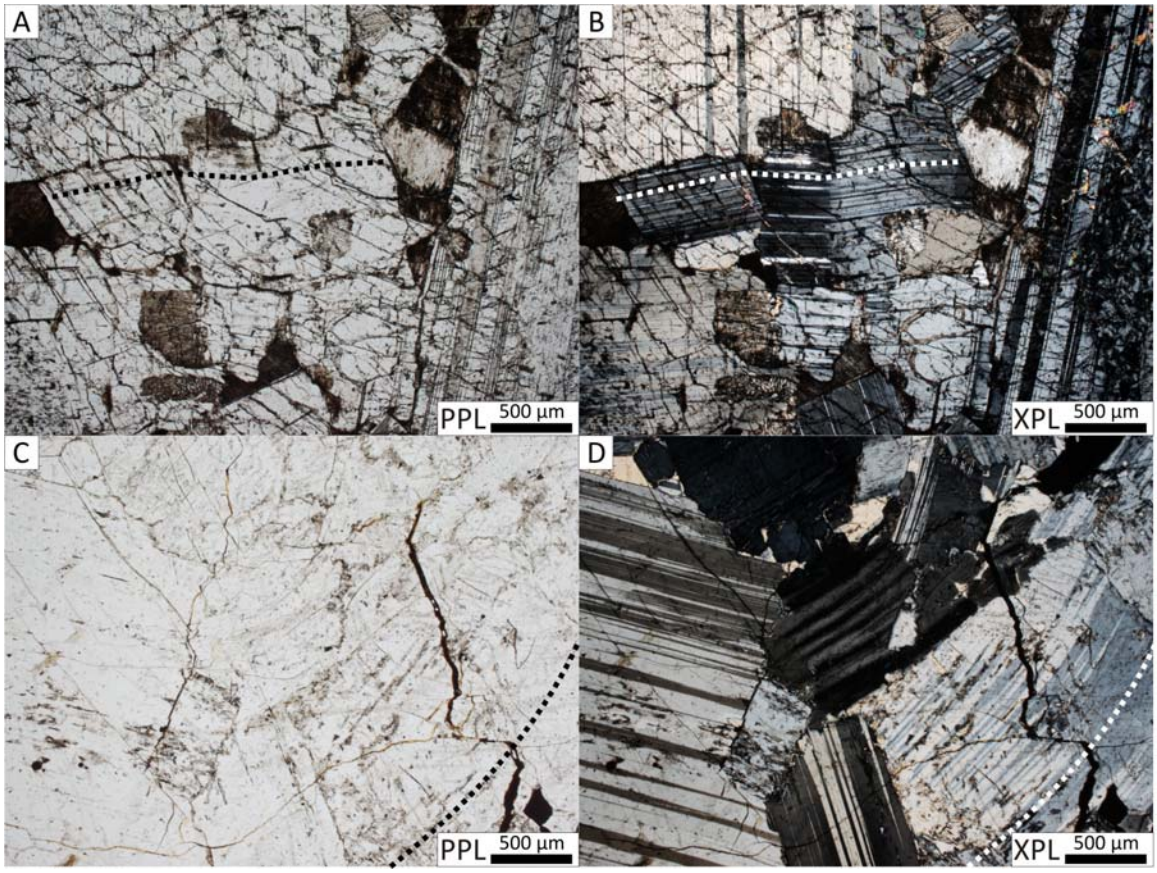

Figure 2-3: Transmitted light photomicrographs of kinked and bent plagioclase twins. A, B) Kinked twins in plagioclase show optical evidence of non-uniform strain. Sharp kinks in the twins are indicated by the dotted line. The different thirds of the crystal go extinct at different times, though fairly uniformly in each section. C, D) Curved twins, indicated by the dotted line, showing a smoother bend in the crystal than the kinked twins. PPL=Plane polarized light; XPL=Cross-polarized light.

significantly from less than 1-2° to ~25° (Figure 2-3C, D). Varying degrees of undulose extinction are exhibited by feldspar grains from throughout the crater. Often the degree of undulose extinction varies even in neighbouring grains.

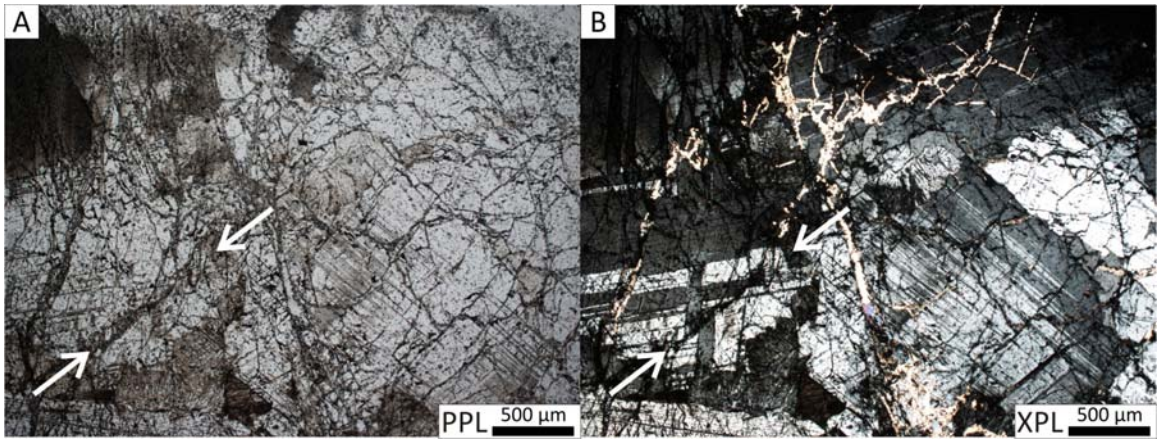

Figure 2-4: Transmitted light photomicrographs of pervasive irregular fracturing in plagioclase. Fracturing occurs throughout all lithologies. Fractures offset twins as seen in bottom left quadrant of (B) (Fracture causing offset is indicated by arrows). PPL=Plane polarized light; XPL=Cross-polarized light.

Fractures are ubiquitous and tend to be relatively elongated but not planar. They cross crystal boundaries and are often at high angles to twins (Figure 2-4). Alteration to clays and zeolites tends to be concentrated along fractures. Twins are offset up to 30 µm by fractures (Figure 2-4b). Samples from outside the central uplift are less fractured than those from the central uplift.

2.4.1 Planar Elements

Pristine (i.e., undecorated) planar deformation features (PDFs) were observed in all quartz grains in thin sections from the central uplift (Figure 2-5A). Quartz outside the central uplift contains only decorated PDFs or, more often, no PDFs at all. One of the most surprising results of this study is that no PDFs were observed in feldspar grains, at any location in the crater. Some features in anorthosite from the central uplift might superficially resemble planar deformation features restricted to alternating twin lamellae in transmitted light. They are approximately perpendicular to twin planes, and abruptly change orientation further up the length of the twins to become oblique to twin planes (Figure 2-5B). However, upon closer inspection, it is apparent that these features are

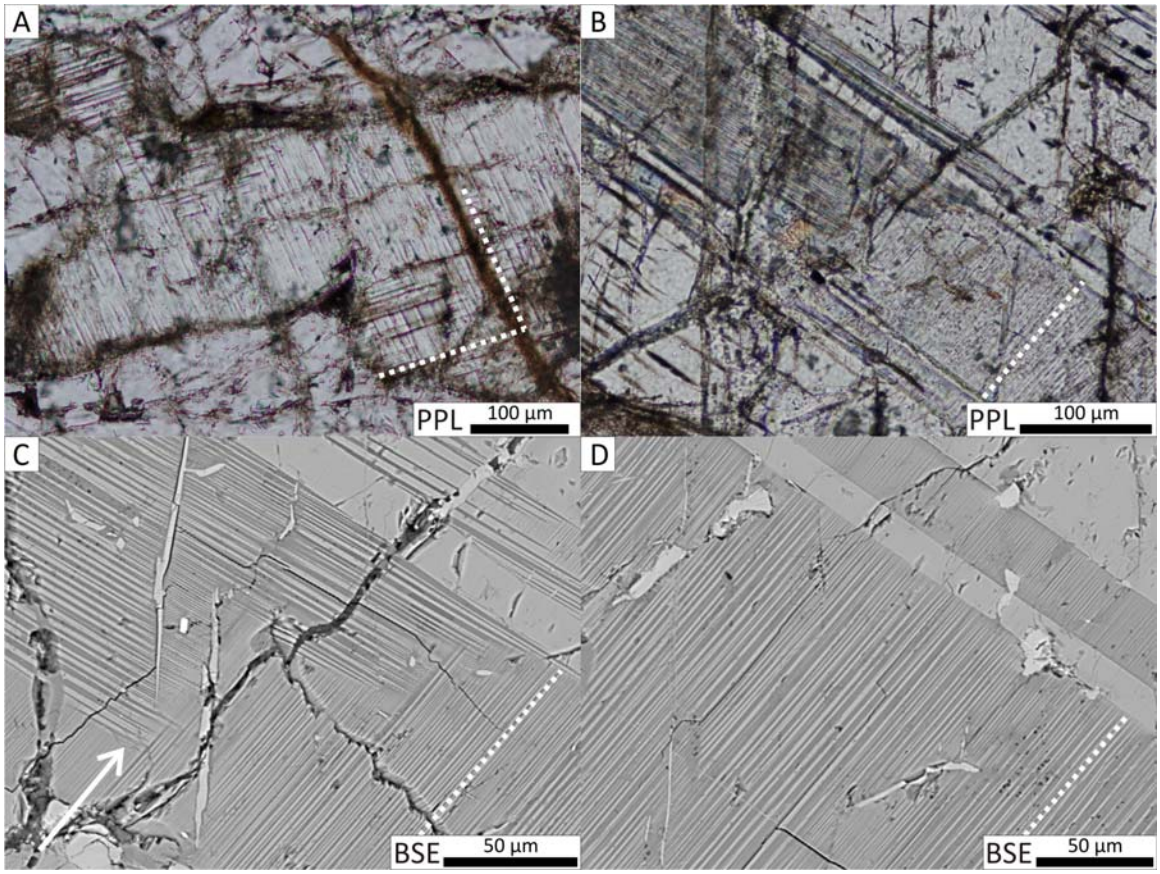

Figure 2-5: Transmitted light photomicrographs of PDFs in quartz, and planar features in alternate plagioclase twins. A) PDFs in quartz from the central uplift. B) Planar features in alternate twins of plagioclase, which superficially resemble planar deformation features. C,D) BSE images showing compositional difference and pinching out (arrow), behaviour which PDFs would not demonstrate. PPL=Plane polarized light; XPL=Cross-polarized light.

actually thin lenses that possess a different composition than the host mineral (Figure 2-5C, D). This differentiates them from PDFs, which are amorphous lamellae of the same composition and consistent thickness across the length (French and Koeberl, 2010). The Fe-oxide microlites mentioned above can also be mistakenly identified as planar deformation features on cursory examination (Figure 2-2). However, on close inspection (with an SEM), they show themselves to be linear rather than planar, to be discontinuous throughout the crystal and to remain birefringent under cross-polarized light.

2.4.2 Diaplectic Glass

The highest level of solid-state shock metamorphism displayed by plagioclase crystals is diaplectic feldspar glass. This can occur in only part of a crystal, while the remainder of the crystal remains birefringent under cross-polarized light (Figure 2-6). However, more commonly, entire grains, or even entire thin sections of plagioclase are isotropic. There are also several instances of only alternate twins becoming diaplectic glass (Figure 2-7), a phenomenon first reported by Stöffler (1966) at the Ries structure, Germany.

All diaplectic feldspar glasses discussed here meet the following three criteria (as suggested by French and Koeberl (2010)): 1) identification of grains as isotropic and pseudomorphous to plagioclase; 2) composition that matches monomineralic plagioclase feldspar as seen by EPMA; and 3) an amorphous state as confirmed by μXRD.

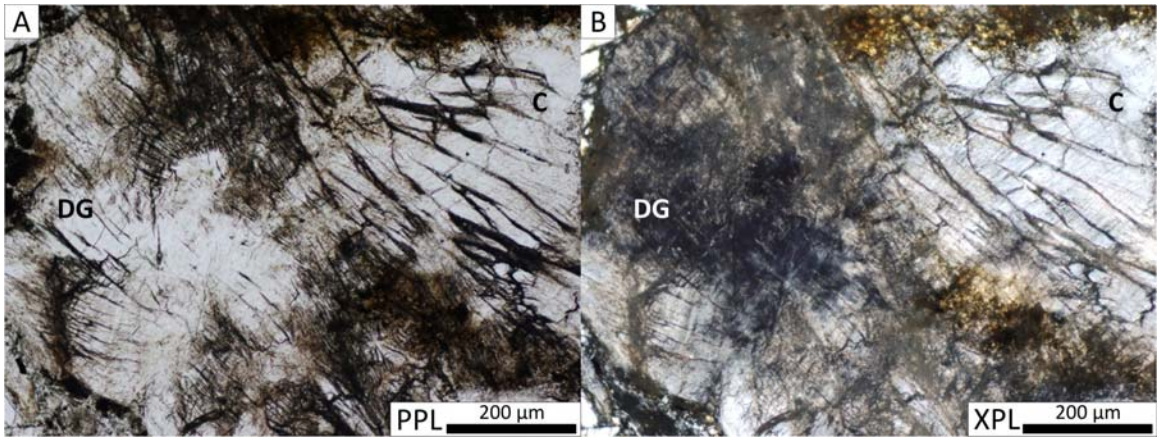

Figure 2-6: Transmitted light photomicrographs of a plagioclase grain showing partial isotropization of feldspar (part of the crystal has been converted to diaplectic feldspar glass). In this case, the area which has become isotropic does not appear to be crystallographically controlled. A) The grain appears clear and transparent with significant fracturing in plane polarized light. B) A portion of the grain is isotropic (glass), remaining extinct on rotation under XPL (left, labeled 'DG'), while the crystalline portion remains birefringent (not glass) in cross-polarized light (right, labeled 'C'). PPL=Plane polarized light; XPL=Cross-polarized light.

2.4.2.1 Partial Isotropization

Several grains appear to have been only partially converted to diaplectic glass. This is evident in that part of a crystal that appears cohesive in plane polarized light will remain extinct on rotation of the stage in cross-polarized light, while the rest of the crystal is birefringent (Figure 2-6). In these grains, there do not appear to be any crystallographic restrictions on which part has become amorphous (Figure 2-6). In some cases, the partial isotropization of plagioclase grains does appear to be crystallo-graphically controlled, manifesting in the isotropization of only alternate twin lamellae (Figure 2-7). EPMA analyses of these twins showed no appreciable change in the composition between crystalline and diaplectic glass twins (Table 2-3). Micro-X-ray diffraction (μXRD) General Area Detector Diffraction System (GADDS) images of diaplectic glass twins show an amorphous band and crystalline streaks, which is an effect of the X-ray beam hitting crystalline material on either side of the glass twin, resulting in constructive interference from diffraction off of those parts of the grain.

2.4.2.2 Complete Isotropization

In several thin sections, all of the feldspars have become diaplectic glass. Electron Probe Microanalysis (EPMA) results show that the chemical composition is homogenous over various points and grains in these sections (Table 2-3). In plane polarized light, isotropic grains (Figure 2-8A) are clear and do not appear any more altered than the crystalline plagioclase of other samples from the area. They appear to be equally as fractured as crystalline grains from other samples. Like much of the plagioclase throughout anorthosite samples at Mistastin, the isotropic grains appear to include many aligned Fe-oxide microlites. They have maintained their external morphology, and appear to be crystalline until examined under crossed polars. Under cross-polarized light, these grains are completely isotropic (Figure 2-8B) (i.e., they remain extinct on rotation). The microlites are all aligned in the same direction, and do not appear to have been disrupted. They match the morphology and optical properties of similar microlites in crystalline feldspathic grains from other samples.

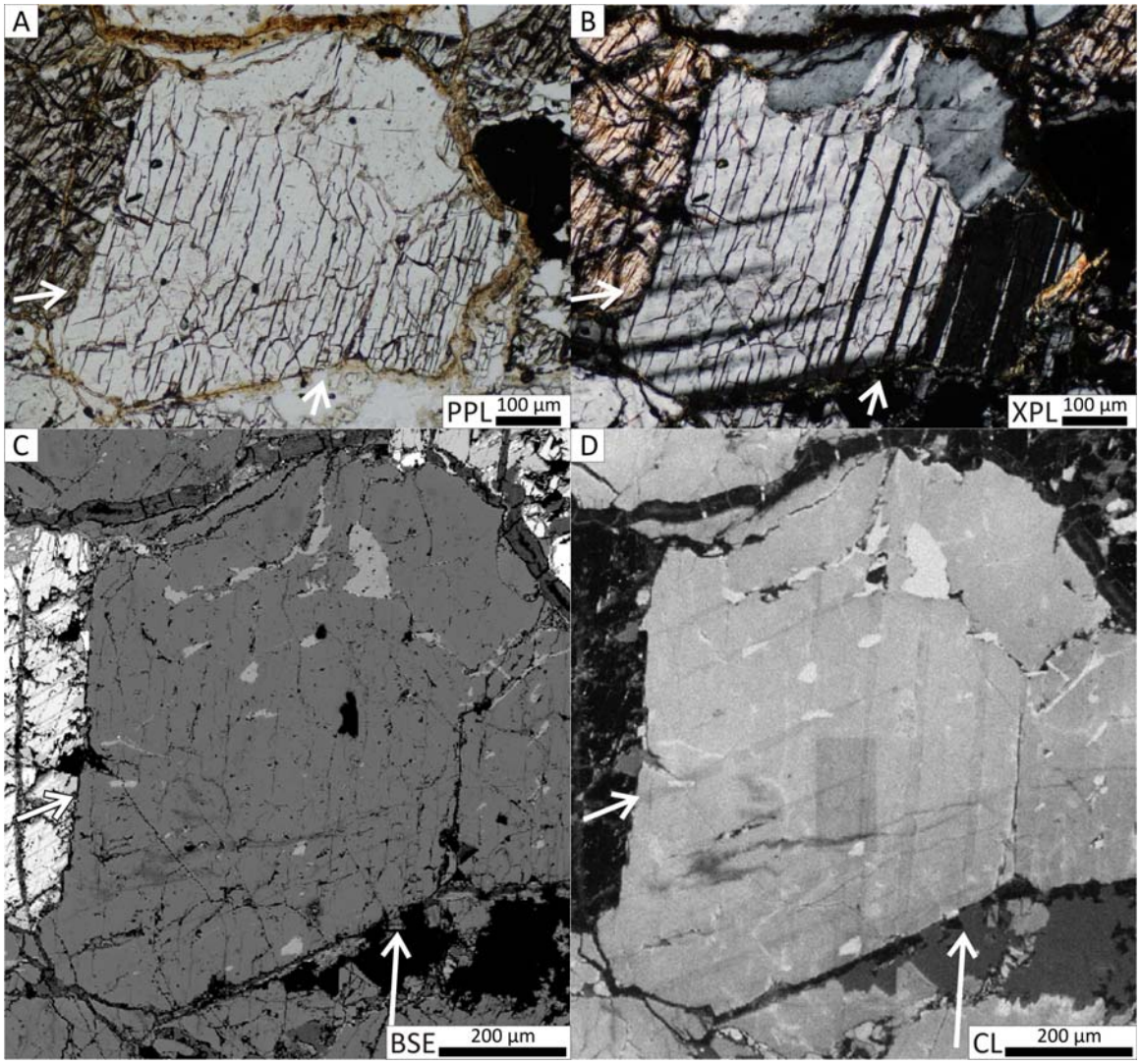

Figure 2-7: Transmitted light photomicrographs, BSE image, and CL image of a plagioclase grain displaying alternate twin isotropization. A-B) A grain displaying two sets of twins that have been converted to diaplectic glass. In (B) the sets of twins that are black remain extinct on rotation of the stage. C) BSE image showing no features that correlate with the isotropic twins. Brighter areas within the grain are patches of potassium feldspar. D) CL image shows thick lines of decreased luminescence (arrows) which correlate with the isotropic twins in (B). PPL=Plane polarized light; XPL=Cross-polarized light; BSE=Back-scatter electron image; CL=Cathodoluminescence image.

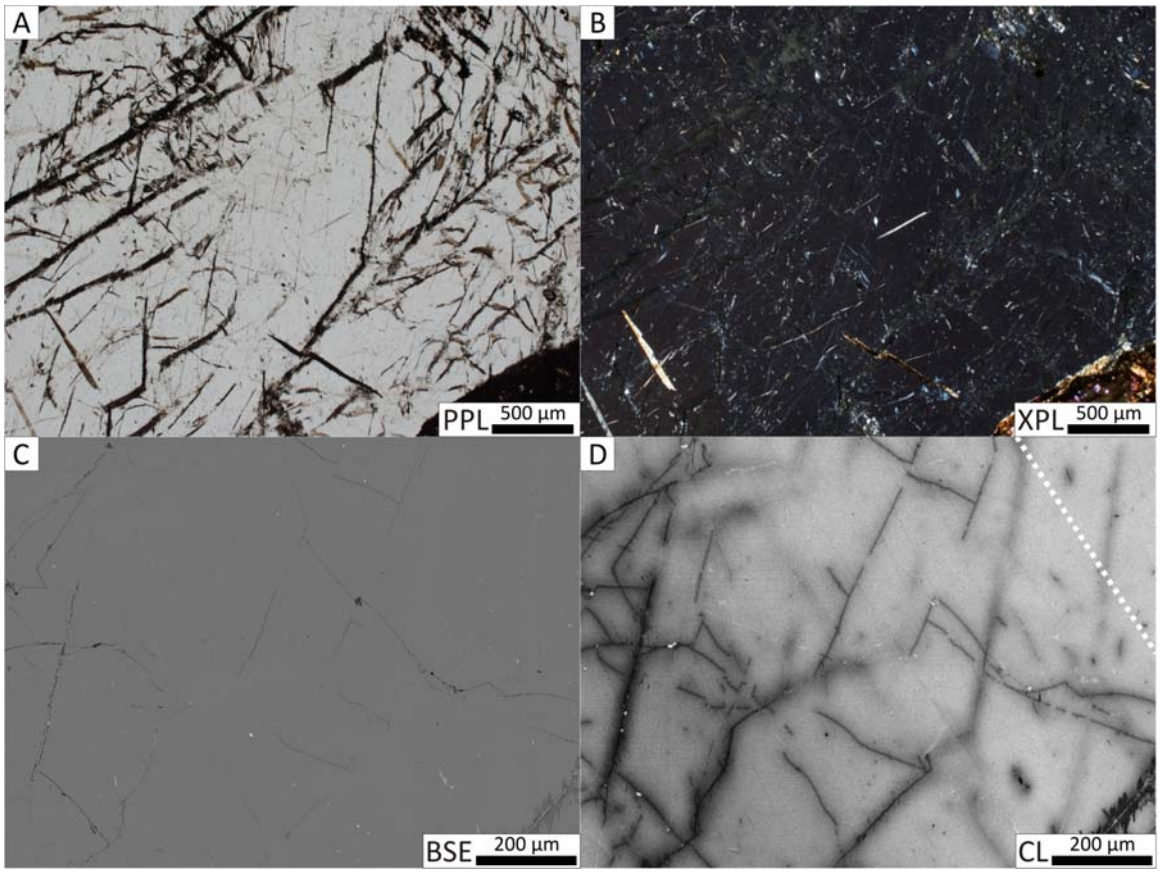

Figure 2-8: Transmitted light photomicrographs, BSE image, and CL image of diaplectic plagioclase glass. A-B) Except for inclusions the grain remains extinct on rotation of the stage under crossed polarized light. C) No linear features are apparent in BSE images. D) There are some linear features apparent in CL that are aligned with the dotted line that might be relict evidence of twins. PPL=Plane polarized light; XPL=Cross-polarized light; BSE=Back-scatter electron image; CL=Cathodoluminescence image.

Table 2-3: Average composition of plagioclase feldspars, levyne-Ca, diaplectic feldspar glasses, and alkali feldspars from Mistastin Lake.

Phase	Feldspar		Feldspar		Feldspar		Feldspar		Feldspar**		Levyne-Ca	
Sample #	MM10-011		MM10-048		MM10-032b		MM10-040		MHI10-17		MHI10-17	
Grain count	5		3		1		9		5		3	
Rock Type	Anorthosite breccia		Granodiorite		Mangerite		Anorthosite Breccia		Anorthosite		Anorthosite	
Location	Coté Creek 1		Rim's End		River Island		South Creek		Central Uplift		Central Uplift	
# of analyses	24		15		5		45		20		12	
An content	An_{47}		An_{31}		An_{31}		An_{49}		An_{55}		N/A	
	wt %	s.d.	wt %	s.d.	wt %	s.d.	wt %	s.d.	wt %	s.d.	wt %	s.d.
SiO_2	56.73	1.07	60.89	0.29	60.94	0.49	56.29	0.56	54.59	0.57	47.85	0.75
Na_2O	5.80	0.36	7.75	0.08	7.79	0.32	5.48	0.20	5.39	0.16	0.27	0.05
Al_2O_3	27.43	0.57	25.17	0.17	25.37	0.56	28.36	0.35	27.82	0.40	22.89	0.41
K_2O	0.47	0.09	0.34	0.03	0.21	0.05	0.37	0.07	0.40	0.02	0.63	0.06
CaO	9.07	0.59	6.11	0.17	6.17	0.43	10.00	0.40	10.03	0.43	11.02	0.09
Total	99.90	0.87	100.45	0.44	100.67	0.27	100.92	0.58	98.22	0.35	82.67	1.18
Cations												
SiO_2	7.65	0.10	8.09	0.02	8.07	0.07	7.53	0.05	7.50	0.07	7.73	0.03
Na_2O	1.52	0.09	2.00	0.02	2.00	0.08	1.42	0.05	1.44	0.04	0.09	0.01
Al_2O_3	4.36	0.11	3.94	0.02	3.96	0.08	4.47	0.05	4.51	0.07	4.36	0.03
K_2O	0.08	0.02	0.06	0.00	0.04	0.01	0.06	0.01	0.07	0.00	0.13	0.01
CaO	1.31	0.09	0.87	0.02	0.88	0.06	1.43	0.06	1.48	0.06	1.91	0.03
Total	14.96	0.02	14.97	0.01	14.97	0.02	14.97	0.02	15.00	0.02	14.20	0.02

*Abbreviations: wt% = mean composition in weight%; s.d. = standard deviation

**These feldspars are from parts of the crystal adjacent to the zeolite levyne-Ca

(Table 2-3 continued)

Phase	Diaplectic Glass		Diaplectic Glass		Diaplectic Glass		Diaplectic Glass		K-Feldspar		K-Feldspar	
Sample #	MM10-34C-5		MM10-38		MM09-035D		MM10-13-2		MM10-048		MM10-032b	
Grain count	3		8		5		8		3		2	
Rock Type	Polymict Breccia		Anorthosite Breccia		Anorthosite		Anorthosite		Granodiorite		Mangerite	
Location	Coté Creek		South Creek		Coté Creek		Coté Creek		Rim's End		River Island	
# of analyses	15		40		25		40		13		8	
An content	N/A		An_{44}		An_{47}		An_{50}		N/A		N/A	
	wt %	s.d.	wt %	s.d.	wt %	s.d.	wt %	s.d.	wt %	s.d.	wt %	s.d.
SiO_2	46.40	2.04	56.17	0.81	54.85	0.74	55.94	0.63	65.35	0.85	64.97	0.48
Na_2O	3.81	1.30	3.14	0.48	3.26	0.46	3.16	0.46	2.13	1.31	1.85	1.29
Al_2O_3	22.57	4.09	28.19	0.82	28.19	0.49	29.17	0.38	19.53	0.43	19.48	0.42
K_2O	0.50	0.45	0.48	0.04	0.61	0.10	0.41	0.04	13.22	2.42	13.61	2.25
CaO	6.75	1.00	9.59	0.56	9.38	0.50	10.30	0.40	-0.77	0.30	-0.86	0.31
Total	80.26	6.69	97.94	1.01	96.71	1.15	99.31	0.40	100.21	0.52	100.30	0.19
Cations												
SiO_2	7.76	0.42	7.65	0.11	7.59	0.07	7.54	0.07	8.95	0.02	8.94	0.03
Na_2O	1.23	0.39	0.83	0.13	0.87	0.13	0.83	0.12	0.56	0.34	0.49	0.34
Al_2O_3	4.39	0.54	4.53	0.10	4.60	0.06	4.63	0.06	3.15	0.03	3.16	0.04
K_2O	0.11	0.10	0.08	0.01	0.11	0.02	0.07	0.01	2.32	0.45	2.39	0.41
CaO	1.20	0.14	1.40	0.08	1.39	0.06	1.49	0.06	-0.11	0.04	-0.13	0.05
Total	14.72	0.29	14.53	0.11	14.60	0.10	14.59	0.10	14.91	0.08	14.92	0.03

*Abbreviations: wt% = mean composition in weight%; s.d. = standard deviation

**These feldspars are from parts of the crystal adjacent to the zeolite levyne-Ca

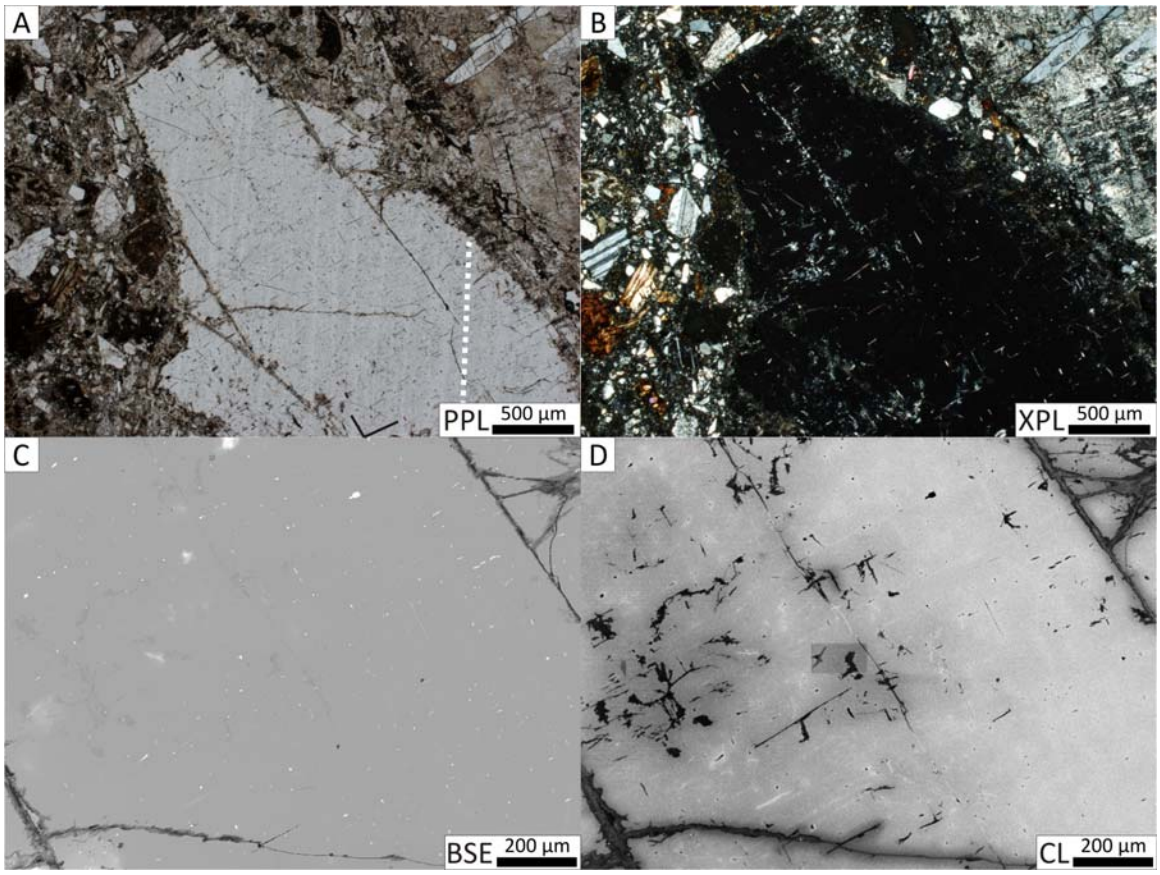

Figure 2-9: Transmitted light photomicrographs, BSE image, and CL image of a diaplectic plagioclase glass clast in a breccia. A) PPL shows remnant lamellae aligned with the dotted line. They appear to show remnant structure within the grain. There is no evidence of these in either XPL (B), BSE (C), or CL (D). PPL=Plane polarized light; XPL=Cross-polarized light; BSE=Back-scatter electron image; CL=Cathodoluminescence image.

One clast of diaplectic glass in a polymict impact breccia shows lamellar features with the appearance of relict twins in plane polarized light (Figure 2-9). The surface of the lamellar features in the diaplectic glass was examined using secondary electron imaging, and no surficial artefacts were observed that would explain them. This grain was also imaged in CL, but no trace of the lamellae was found (Figure 2-9D). Cathodo-luminescence images of some other diaplectic glass grains showed possible evidence of

remnant twins (Figure 2-8D). These linear features are slightly less luminescent than the surrounding crystal. They are faint, narrow, and line up with the microlites visible in the photomicrographs. Unlike the Fe-oxide microlites, they are continuous across the grain and they are not visible in the BSE images.

2.4.3 Alteration

An unusual extinction pattern was observed first in anorthosite from the central uplift, and, subsequently, in clasts and in the matrix of brecciated target rocks from South Creek. This pattern was first described as an odd mosaic/pseudo-fibrous patchy extinction pattern Pickersgill et al. (2013), which is mottled and when rotated under cross-polarized light shows a pseudo-fibrous radial extinction pattern similar to that described as plumose by McIntyre (1968) (Figure 2-10).

Micro-X-ray diffraction (μXRD) studies show the crystalline structure of the plumose material to be the zeolite levyne-Ca (Figure 2-11), known to occur naturally only in cavities of basaltic rocks or synthesized from basaltic glass (Deer et al., 2004). Electron probe microanalysis (EPMA) results (summarized in Table 2-3) confirm the μXRD findings, through a chemical composition consistent with the zeolite levyne-Ca (Deer et al., 2004). In the case of the zeolitized twins, it is important to note that the extensions of the zeolitized twins vary in composition compared to the surrounding crystal by less than 1%. This means that chemical change is associated with the zeolite only, and not just with the twins (an observation which is confirmed by chemistry of the vein-like zeolite).

In one sample, this pattern is sometimes restricted to alternate twin lamellae (Figure 2-10 C-F), sometimes truncated by crystal boundaries, and sometimes has a more vein-like texture cross-cutting crystal boundaries (Figure 2-10 A,B). In other samples, the same pattern is observed as pseudomorphous with entire feldspar clasts, and rimming plagioclase clasts in polymict and monomict impact breccias.

In plane polarized light, these zeolites are easily mistaken for plagioclase crystals. They bear every resemblance to clear, unaltered, well-formed plagioclase crystals, often

Figure 2-10: Transmitted light photomicrographs, and BSE images, of the pseudomorphous zeolite phase levyne-Ca. Levyne-Ca appears pseudomorphous to the surrounding plagioclase in both transmitted light (A-D) and BSE (E-F). Note that in PPL (A, C) the zeolitized area is clear and has fewer fractures than the surrounding plagioclase. A-B) zeolitization which appears vein like; on the right side of the image it crosses a crystal boundary, while on the left it is abruptly halted by the same. C-D) preferential zeolitization of alternate twin lamellae. Note in the plagioclase twins the perpendicular fractures, which do not exist in the zeolitized twins. E-F) BSE images of the alternate altered twins showing compositional difference and highlighting the fractures, which are truncated by the zeolitized twins. PPL=Plane polarized light; XPL=Cross-polarized light; BSE=Back-scatter electron image; CL=Cathodoluminescence image.

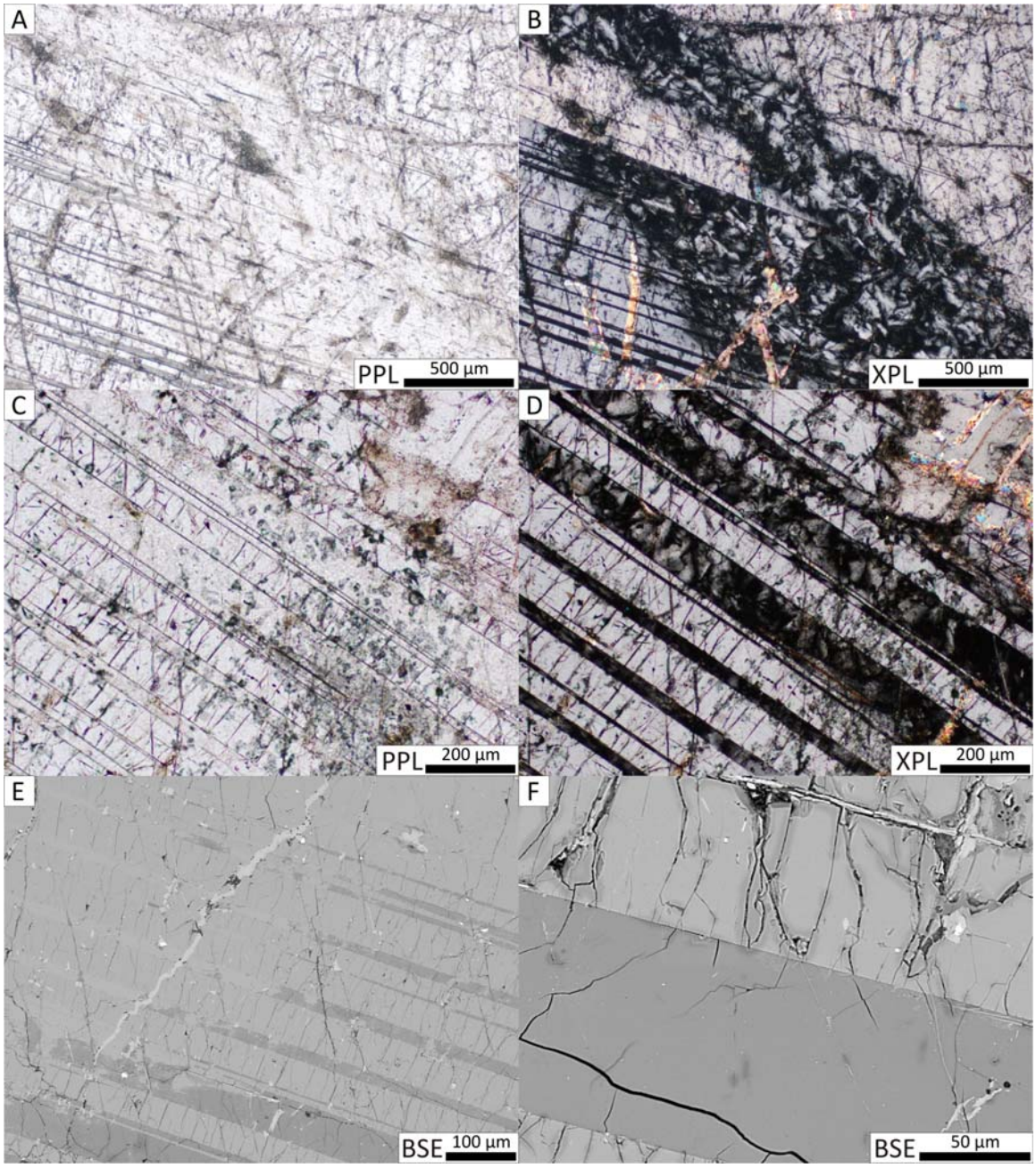
A
PPL
500 µm
B
XPL
500 µm
C
PPL
200 µm
D
XPL
200 µm
E
BSE
100 µm
F
BSE
50 µm

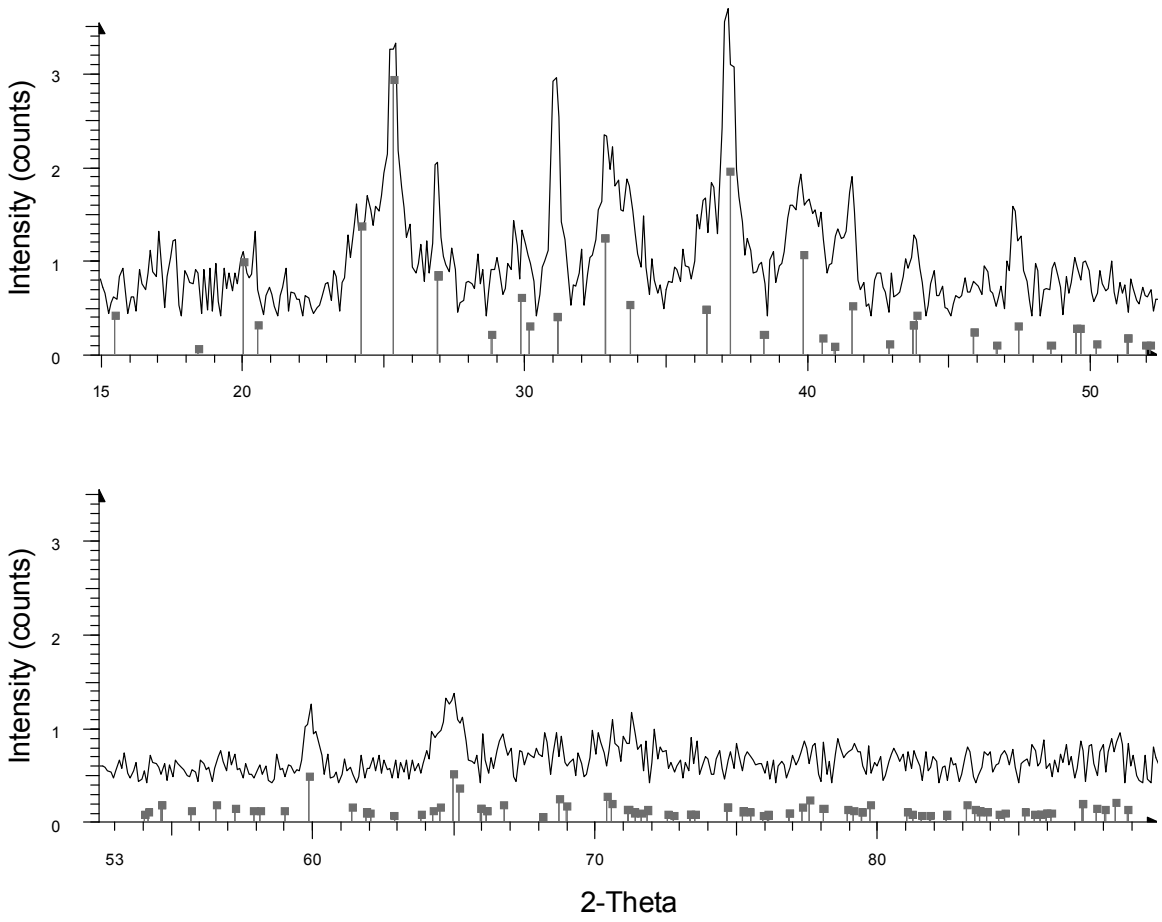

Figure 2-11: µXRD plot of intensity versus 2θ for levyne-Ca. The pattern matches the zeolite levyne-Ca (ICDD card 00-046-1263(C)).

preserving evidence of twinning and the aligned Fe-oxide microlites present in plagioclase crystals of the surrounding material. In the case in which zeolites are restricted to only alternate twin lamellae, there is a fracture set which is abruptly truncated by the deformed twins. The perpendicular fractures exist in the normal twins, next to the unaltered extensions of the zeolitized twins, as well. There are multiple other instances of alternate twins altering to other products more readily than their neighbours. In these cases, the alteration is visible as grey-brown darkening of the twins visible in plane polarized light, and reduced transmission of light in both plane- and cross-polarized light.

2.5 Discussion

2.5.1 Planar Elements

Many of the petrographic observations in this paper corroborate those of previous studies at Mistastin Lake, reporting pervasive irregular fracturing throughout minerals, lateral displacement along fractures (offset twins, etc.), and planar deformation features in quartz (Taylor and Dence, 1969). However, in contrast to Taylor and Dence (1969), no planar deformation features were found in plagioclase anywhere in the crater structure. In several instances, the discovery of planar deformation features was thought to have occurred but on closer inspection with an SEM, these textures turned out to be zeolitization along pre-existing crystal planes (Figure 2-5), or faint clouding (Fe-oxide microlites) in plagioclase grains (Figure 2-2).

French and Koeberl (2010) report from references therein that PDFs in quartz and feldspar form at approximately the same pressures (~10–30 GPa). In this study, samples from the central uplift invariably showed well-developed, pristine planar deformation features in quartz grains (Figure 2-5A,B), while the plagioclases showed none at all. The presence of PDFs in quartz in these sections, coupled with their absence in neighbouring plagioclase, implies one or more of the following explanations: 1) PDFs form in plagioclase much less frequently than in quartz and than previously thought; and/or 2) that PDFs in feldspars are more difficult to recognize than in quartz; and/or 3) that PDFs are more easily destroyed in plagioclase than in quartz. The pristine nature of PDFs in quartz grains (Figure 2-5) and the general lack of alteration in many of the feldspars suggests that these samples have not been affected by annealing or any major post-impact alteration. Therefore, it seems unlikely that alteration or annealing could be the cause for lack of PDFs in feldspars.

The composition of PDF-containing feldspars is unfortunately often not reported in the literature, but when compositional data are provided, the feldspars are more often of the low-Ca ($An_{<30}$) plagioclase or K-feldspar series rather than Ca-rich plagioclase (Gibson and Reimold, 2005; Nagy et al., 2008; Trepmann et al., 2003). The plagioclase at Mistastin is $An_{31\text{-}55.}$ This may imply that there is a structural and/or compositional

control that encourages PDF development in the Ca-poor plagioclase and alkali series over the Ca-rich plagioclases. The plagioclase series is consistently triclinic (>An_{10}), the albite endmember can be monoclinic (at >980°C) (Deer et al., 2001). In the alkali series, anorthoclase is also triclinic at room temperature, but can be monoclinic at crystallization temperatures, and sanidine is always monoclinic (Deer et al., 2001). We hypothesize that the higher symmetry of monoclinic feldspars may encourage formation of PDFs in Ca-poor plagioclase and potassium feldspars over Ca-rich plagioclase. Other mineral systems in which planar deformation features have been reported include: monoclinic (diopside), orthorhombic (sillimanite, cordierite, olivine, orthopyroxene), isometric (garnet), hexagonal (apatite, quartz), and tetragonal (zircon) (e.g., Bohor et al., 1993; Dressler, 1990; Dworak, 1969; Nesse, 2004; Stöffler, 1974, 1972; Stöffler et al., 1991; Wittmann et al., 2006). It is imperative then that chemical composition be reported for studies of feldspars, as the shock effects appear to vary widely with chemical composition, but this is poorly constrained due to the lack of compositional data provided in many previous shock studies. Variation in the development of PDFs with changing composition within the plagioclase series is also currently unknown.

The exact processes which cause the development of PDFs are unclear (French and Koeberl, 2010). However, a possible explanation for the lack of PDFs in plagioclase feldspar could be related to pre-existing planes of weakness in plagioclase along which to "relieve" the pressure caused by passage of the shockwave, and that this mechanism of pressure release precludes – or greatly inhibits – the formation of planar amorphous lamellae such as PDFs. This does not necessarily mean that plagioclase feldspars can never form PDFs, only that they are far less common than perhaps originally reported, and that they likely form under a much narrower range of pressure conditions, as is supported by Ostertag (1983) particularly in labradorite.

In order to address the effect(s) that crystal symmetry has on PDF formation, a detailed study of naturally and experimentally shocked feldspars of various compositions and predicted peak pressures should be conducted. If amorphous lamellae are, indeed, forming along pre-existing planes of weakness in feldspars then the use of finer scale instruments (e.g., transmission electron microscopy) is required.

2.5.2 Diaplectic Glass

In diaplectic feldspar glasses such as Figure 2-8, the remnants of pre-existing structure are still visible, through the arrangement of the Fe-oxide microlites. Microlites provide deeper insight than just looking at the exterior of the crystal, because they are small and not held in place by external forces such as surrounding minerals.

Crystallographically controlled alignment of Fe-oxide microlites, the possible preservation of twins, and the preservation of outward crystal boundaries (Figures 2-8, 2-9) support the interpretation that these glasses formed as the result of a solid-state transition between crystalline and amorphous material. This evidence precludes the possibility of low-viscosity melting, as microlites would certainly be disrupted in all but the most viscous, and temporary melts. It supports a lack of flow, which has been suggested to occur in meteoritic maskelynite (Chen and El Goresy, 2000), calling on the surrounding crystals to contain the apparent mineral melt, resulting in a glass which seems to have maintained an external crystal form. No glasses were found that appeared to be the result of highly viscous melts, as one might expect as a transitional state between diaplectic and natural melt glasses.

The preferential shock deformation of only alternate twin lamellae has been discussed previously by Gibson and Reimold (2005), Stöffler (1966), and Short and Gold (1996). Our observations of diaplectic glass forming in only alternate twin lamellae support these observations and support the hypothesis that the orientation of the shockwave relative to the orientation of the crystal affects the degree and type of shock effects that occur (Stöffler, 1966).

2.5.3 Alteration

Variable alteration of plagioclase to zeolite was found in this study. The selective alteration of alternate twins is reminiscent of the way in which diaplectic feldspar glass sometimes occurs only in alternate twins. A possible explanation for this is that the zeolites in these cases are preferentially altering the twin converted to diaplectic feldspar glass and not the crystalline twin, consistent with the metastable nature of diaplectic glass. Indeed, the identification of the area of plumose extinction as the zeolite levyne-Ca

by μXRD has led to the interpretation that zeolitization, in this case, is the result of preferential alteration of a shock-weakened crystal structure. No other circumstance, as far as we are aware, results in deformation of only alternate twin lamellae; speculation on the reason for this in shock metamorphism usually centres around orientation of the crystal structure relative to the direction of shockwave propagation (Stöffler, 1966).

Metastable feldspathic glass, produced through melting or solid state amorphization would be particularly susceptible to alteration and recrystallization as a zeolite. This hypothesis matches the reported synthesis of levyne-Ca from basaltic glass (Deer et al., 2004), the pseudomorphous vitrification of plagioclases, as a result of shock, and the observation of alternate twin lamellae becoming isotropic, as a result of shock. Therefore, it seems probably that much of the zeolitization observed in these samples is the result of secondary processes enabled by shock metamorphism.

2.6 Concluding remarks

The most widely recognized diagnostic shock metamorphic feature in plagioclase feldspars in the samples studied here is diaplectic feldspar glass. Inferences about the degree of shock can be made based on the degree to which single crystals have been isotropized (the entire crystal, part of the crystal, only alternate twins, etc.). Because diaplectic glasses lose more internal structure with increasing shock level (e.g., Lambert and Grieve, 1984), it is possible that at higher pressures evidence of twinning is less evident and the degree of chemical homogenization increases – as they get closer to being monomineralic melt glasses. Other features, such as fracturing and undulose extinction, can be indicative of shock metamorphism but are not diagnostic.

Further investigation into the nature of planar deformation features in plagioclase needs to involve the investigation of twin and cleavage planes by finer scale techniques to identify if glass is present along those planes, indicating PDFs forming, as in quartz, parallel to rational crystallographic planes but masked by co-incidence with pre-existing planar features in the mineral. Additional studies of diaplectic feldspar glass will determine whether there are different stages of amorphization leading up to melt glass.

2.7 References

Binns R. A. 1967. Stony meteorites bearing maskelynite. *Nature* 213: 1111–1112.

Bohor B. F., Betterton W. J., and Krogh T. E. 1993. Impact-shocked zircons: discovery of shock-induced textures reflecting increasing degrees of shock metamorphism. *Earth and Planetary Science Letters* 119: 419–424.

Chao E. C. T. 1967. Impact Metamorphism. In *Researches in Geochemistry, vol. 2*, edited by Abelson P. H. New York: John Wiley & Sons, Ltd. pp. 204–233.

Chen M., and El Goresy A. 2000. The nature of maskelynite in shocked meteorites; not diaplectic glass but a glass quenched from shock-induced dense melt at high pressures. *Earth and Planetary Science Letters* 179: 489–502.

Currie K. L. 1971. Geology of the resurgent cryptoexplosion crater at Mistastin Lake, Labrador. *Bulletin - Geological Survey of Canada* 207: 62 p.

Deer W. A., Howie R. A., Wise W. S., and Zussman J. 2004.*Rock-Forming Minerals, Volume 4B: Framework Silicates - Silica Minerals, Feldspathoids and Zeolites*, 2nd ed. London: The Geological Society. 982 p.

Deer W. A., Howie R. A., and Zussman J. 2001.*Rock-Forming Minerals, Volume 4a: Framework Silicates - Feldspars*, 2nd ed. London: The Geological Society. 972 p.

Dressler B. 1990. Shock metamorphic features and their zoning and orientation in the Precambrian rocks of the Manicouagan Structure, Quebec, Canada. *Tectonophysics* 171: 229–245.

Dworak U. 1969. Stoßwellenmetamorphose des Anorthosits vom Manicouagan Krater, Quebec, Canada. *Contributions to Mineralogy and Petrology* 24: 306–347.

Emslie R. F., and Stirling J. A. R. 1993. Rapakivi and related granitoids of the Nain plutonic suite: geochemistry, mineral assemblages and fluid equilibria. *The Canadian Mineralogist* 31: 821–847.

Engelhardt W. von, and Stöffler D. 1968. Stages of shock metamorphism in crystalline rocks of the Ries Basin, Germany. In *Shock metamorphism of natural materials*, edited by French B. M., and Short N. M. Baltimore, MD: Mono Book Corp. pp. 159–168.

Ferrière L., Morrow J. R., Amgaa T., and Koeberl C. 2009. Systematic study of universal-stage measurements of planar deformation features in shocked quartz: Implications for statistical significance and representation of results. *Meteoritics & Planetary Science* 44: 925–940.

French B. M., and Koeberl C. 2010. The convincing identification of terrestrial meteorite impact structures: What works, what doesn't, and why. *Earth-Science Reviews* 98: 123–170.

Gibson R. L., and Reimold W. U. 2005. Shock pressure distribution in the Vredefort impact structure, South Africa. In *Special Paper - Geological Society of America*, edited by Kenkmann T., Hörz F. P., and Deutsch A. Geological Society of America (GSA), Boulder, CO. pp. 329–349.

Goltrant O., Leroux H., Doukhan J.-C., and Cordier P. 1992. Formation mechanisms of planar deformation features in naturally shocked quartz. *Physics of the Earth and Planetary Interiors* 74: 219–240.

Grieve R. A. F. 2006.*Impact Structures in Canada*, Geological Association of Canada. 210 p.

Grieve R. A. F. 1975. Petrology and chemistry of the impact melt at Mistastin Lake crater, Labrador. *Geological Society of America Bulletin* 86: 1617–1629.

Jaret S., Kah L. C., and French B. M. 2009. Feldspar deformation as an indicator of low-barometry shock: petrographic investigation of ejecta from the Tenoumer impact crater, Mauritania. In *Geological Society of America Abstracts with Programs*. p. 313.

Kayama M., Nishido H., Sekine T., Nakazato T., Gucsik A., and Ninagawa K. 2012. Shock barometer using cathodoluminescence of alkali feldspar. *Journal of Geophysical Research* 117: E09004.

Lambert P. 1979. Fractures induced by shock in quartz and feldspar. *Mineralogical Magazine* 43: 527–533.

Lambert P., and Grieve R. A. F. 1984. Shock experiments on maskelynite-bearing anorthosite. *Earth and Planetary Science Letters* 68: 159–171.

Mak E., York D., Grieve R. A. F., and Dence M. 1976. The age of the Mistastin Lake crater, Labrador, Canada. *Earth and Planetary Science Letters* 31: 345–357.

Marion C. L., and Sylvester P. J. 2010. Composition and heterogeneity of anorthositic impact melt at Mistastin Lake crater, Labrador. *Planetary and Space Science* 58: 552–573.

McIntyre D. B. 1968. Impact Metamorphism at Clearwater Lake, Quebec. In *Shock metamorphism of natural materials*, edited by French B. M., and Short N. M. Baltimore: Mono Book Corp. pp. 363–366.

Nagy S., Gucsik A., Bérczi S., Ninagawa K., Nishido H., Kereszturi A., Hargitai H., and Okumura T. 2008. K-feldspar and biotite as shock indicator minerals from Bosumtwi impact crater. *Abstracts of Papers Submitted to the Lunar and Planetary Science Conference* 39: Abstract 1144.

Nesse W. D. 2004. *Introduction to Optical Mineralogy*, 3rd ed. New York: Oxford University Press. 348 p.

Ostertag R. 1983. Shock experiments on feldspar crystals. *Journal of Geophysical Research* 88, Suppl.: B364–B376.

Ostertag R., and Jessberger E. K. 1982. Shock-effects on the K-Ar system of plagioclase feldspar and the age of anorthosite inclusions from North-Eastern Minnesota. *Geochimica et Cosmochimica Acta* 46: 1465–1471.

Pickersgill A. E., Osinski G. R., and Flemming R. L. 2013. Shock Metamorphism in Plagioclase from the Mistastin Lake Impact Structure, Canada. *44th Lunar and Planetary Science Conference* Abstract #2471.

Poldervaart A., and Gilkey A. K. 1954. On clouded plagioclase. *American Mineralogist* 35: 75–91.

Short N. M., and Gold D. P. 1996. Petrography of shocked rocks from the central peak at the Manson impact structure. In *Special Paper - Geological Society of America*, edited by Koeberl C., and Anderson R. R. Geological Society of America (GSA), Boulder, CO. pp. 245–265.

Singleton A. C., Osinski G. R., McCausland P. J. A., and Moser D. E. 2011. Shock-induced changes in density and porosity in shock-metamorphosed crystalline rocks, Haughton impact structure, Canada. *Meteoritics & Planetary Science* 46: 1774–1786.

Steiger R. H., and Jäger E. 1977. Subcommission on geochronology: convention on the use of decay constants in geo- and cosmochronology. *Earth and Planetary Science Letters* 36: 359–362.

Stöffler D. 1972. Deformation and transformation of rock-forming minerals by natural and experimental shock processes: I. Behavior of minerals under shock compression. *Fortschritte der Mineralogie* 49: 50–113.

Stöffler D. 1974. Deformation and transformation of rock-forming minerals by natural and experimental shock processes: II. Physical properties of shocked minerals. *Fortschritte der Mineralogie* 51: 256–289.

Stöffler D. 1971. Progressive metamorphism and classification of shocked and brecciated crystalline rocks at impact craters. *Journal of Geophysical Research* 76: 5541–5551.

Stöffler D. 1966. Zones of impact metamorphism in the crystalline rocks of the Nördlinger Ries crater. *Contributions to Mineralogy and Petrology* 12: 15–24.

Stöffler D., and Hornemann U. 1972. Quartz and feldspar glasses produced by natural and experimental shock. *Meteoritics* 7: 371–394.

Stöffler D., Keil K., and Scott E. R. D. 1991. Shock metamorphism of ordinary chondrites. *Geochimica et Cosmochimica Acta* 55: 3845–3867.

Taylor F. C., and Dence M. R. 1969. A probable meteorite origin for Mistastin Lake, Labrador. *Canadian Journal of Earth Sciences* 6: 39–45.

Trepmann C., Whitehead J., and Spray J. 2003. Shock effects in target rocks from the Charlevoix impact structure, Quebec, Canada.

Tschermak G. 1883. Beitrag zur Classification der Meteoriten. *Sitzungsberichte der Mathematisch-Naturwissenschaftlichen Klasse der Kaiserlichen Akademie der Wissenschaften, Wien* 88: 347–371.

Tschermak G. 1872. Die Meteoriten von Shergotty und Gopalpur. *Sitzungsberichte der Mathematisch-Naturwissenschaftlichen Klasse der Kaiserlichen Akademie der Wissenschaften, Wien* 65: 122–145.

Whitney P. R. 1972. Spinel inclusions in plagioclase of metagabbros from the Adirondack Highlands. *American Mineralogist* 57: 1429–1436.

Wittmann A., Kenkmann T., Schmitt R. T., and Stöffler D. 2006. Shock-metamorphosed zircon in terrestrial impact craters. *Meteoritics & Planetary Science* 41: 433–454.

Young K. E., Hodges K. V, van Soest M. C., and Osinski G. R. 2013. Dating the Mistastin Lake impact structure, Labrador, Canada, using zircon (U-Th)/He thermochronology. In *44th Lunar and Planetary Science Conference*. Abstract #2426.

Chapter 3

3 Strain-Related Mosaicity in Chi (°χ) from Micro-X-Ray Diffraction Patterns of Shocked Lunar and Terrestrial Plagioclase

Annemarie E. Pickersgill, Roberta L. Flemming, and Gordon R. Osinski

3.1 Introduction

Studies of shocked minerals from terrestrial impact craters, meteorites, and returned lunar samples have answered many questions regarding the formation of impact craters, the expulsion history of meteorites, and processes that have affected not only the surface of the Moon, but the surface of the other rocky planets as well. In terrestrial samples, the "go-to" mineral for shock barometry is quartz (e.g., Ferrière et al., 2009; French and Koeberl, 2010), as it is optically simple, resistant to alteration, and present in many common surface rocks. As a result, the effects of shock metamorphism on quartz have been extensively studied and it is an excellent tool by which to determine pressure histories of shock metamorphosed rocks. However, in many of the systems listed above, such as meteorites, the surface of the Moon, and the surface Mars, which have been extensively modified by impact, quartz is a much less prevalent mineral. One of the most promising but understudied minerals for this purpose is the feldspar group, particularly the plagioclase series, which is nearly ubiquitous in most planetary systems.

Thus far, studies of shock effects in the feldspar group have been limited, due to their relatively complex crystal structure and the rapid rate at which they weather, making them difficult to study using conventional optical techniques. As a result, the effects of shock on feldspar are being increasingly investigated using a wider range of investigative techniques such as Raman spectroscopy (e.g., Fritz et al., 2005; Jaret et al., 2009), and cathodoluminescence (e.g., Gucsik et al., 2004; Kayama et al., 2012). In micro- and single-crystal X-ray diffraction (XRD) studies, increasing strain causes XRD patterns to extend along the Debye rings or chi (χ) direction forming streaks (Figure 3-1), progressing from single equant spots, to short streaks, to longer streaks, to short rows of

spots (asterism), ultimately to full rings and amorphous bands (Flemming, 2007; Hörz and Quaide, 1973; Izawa et al., 2011; Vinet et al., 2011). *In-situ* micro-X-ray diffraction (μXRD) has immense value over destructive techniques for examining precious planetary materials. This contribution adds to the growing body of knowledge about shock in feldspars using μXRD to quantify the level of strain-related mosaicity experienced by shock-metamorphosed plagioclase feldspar through measurement of the full-width-at-half-maximum of streaks in °chi (FWHMχ) and correlation with optically derived signs of shock metamorphism. This is a technique that has been previously applied successfully to enstatite (Izawa et al., 2011) and olivine (McCausland et al., 2010; Vinet et al., 2011), but is being applied to plagioclase for the first time in this paper.

3.2 Geological Setting

3.2.1 Mistastin Lake impact structure

The Mistastin Lake impact structure is located in central Labrador, Canada (55°53'N; 63°18'W). It is a complex crater structure of approximately 28 km diameter (Grieve, 2006). It's age is 32.7 ± 1.2 Ma according to (U-Th)/He thermochronology of zircons (Young et al., 2013); this is a slightly younger age than the $^{40}Ar/^{39}Ar$ age of 36 ± 4 Ma (Mak et al., 1976). Its hypervelocity impact origin was confirmed by Taylor and Dence (1969) through the discovery of planar deformation features (PDFs) in quartz and feldspar, diaplectic quartz and feldspar glasses, and poorly developed shatter cones. The structure is located within the Mistastin Lake batholith, which is composed of three main lithologies: anorthosite, granodiorite, and mangerite – a pyroxene-rich quartz monzonite (Currie, 1971; Emslie and Stirling, 1993). While all three lithologies are feldspar rich, both the granodiorite and the mangerite are heavily weathered and prone to alteration, while the anorthosite has remained reasonably coherent. It is the presence of this large anorthosite body that makes the Mistastin Lake structure an excellent scientific lunar analogue, as anorthosite is also the main constituent of the lunar highlands.

3.2.2 Apollo Missions

Earth's moon is our nearest planetary neighbour, and has preserved millennia of geological history, due to minimal erosion and lack of crustal recycling. It is a primary exploration target for space agencies the world over and the only planetary body, other than Earth, from which samples have been purposefully collected and returned to Earth. Between 1969 and 1972 six Apollo missions returned 2196 individual samples (381.7 kg) from the near-side surface of the Moon (Hiesinger and Head, 2006). Samples from five of these missions (11, 12, 15, 16, and 17) were used in this study. A brief summary of the geological setting of each mission's landing site is given below.

Apollo 11 (July 1969) landed at Mare Tranquilitatis (0.7°N, 24.3°E) and largely collected basalt samples but also included pieces of anorthosite that are interpreted to be from the nearby highlands. These samples precipitated the interpretation of the lunar crust as being largely feldspathic in composition, and contributed to the development of the first concepts of lunar differentiation (e.g., Smith et al., 1970; Wood et al., 1970). The majority of samples collected at this location are interpreted to be ejecta from West Crater (Beaty and Albee, 1978).

Apollo 12 (November 1969) landed in southeastern Oceanus Procellarum (3.2°N, 23.4°W), near the Surveyor 3 landing site. This site is interpreted to be younger than the Apollo 11 site, based on the relative abundance of craters. At this location there is a relatively thin layer of basalt over nonmare lithologies (Head, 1977; Hiesinger and Head, 2006). Non-volcanic rocks here originate from a prominent ray from Copernicus crater, which crosses the landing site. The majority of the samples collected from this site are basalts (Hiesinger and Head, 2006).

Apollo 15 (July-August 1971) landed in the Hadley-Apennine region (26.1°N, 3.7°E). Samples were collected from the massifs and highlands of the Imbrium rim, and mare of Palus Putredinis (Hiesinger and Head, 2006). The site is largely basalts, overlain by rays from Autolycus and Aristillus craters. Both mare and nonmare rocks were collected here, including two types of lava, anorthosites, plutonic rocks, impact melt rocks, granulites, and regolith breccias.

Apollo 16 (May 1972) landed near Descartes Crater (9°S, 15.5°E) in the lunar highlands, the only true highland landing site of the Apollo program (Hiesinger and Head, 2006). There are numerous overlapping old craters, and two young craters, at this site. As a result, all of the returned samples are impactites, most are impact melt rocks or fragmental breccias, with some anorthosite samples. Samples from this site are largely interpreted to be ejecta from the Imbrium, Serenitatis, and Nectaris basin forming events (e.g., Haskin et al., 2002; Spudis, 1984).

Apollo 17 (December 1972) landed at the Taurus-Littrow Valley (20.2°N, 30.8°E). This site is at the highland/mare boundary near the southeastern rim of the Serenitatis basin. Samples collected from this site include basalts, impact melt rocks (presumably from Serenitatis), and plutonic rocks (Haskin et al., 2002; Head, 1974; Hiesinger and Head, 2006).

3.3 Methods and Samples

Twenty-two polished thins sections from lunar samples were selected from those returned from Apollo missions 11, 12, 15, 16, and 17. Sample selection was based on proportion of plagioclase contained within each thin section, as determined from a literature review, review of the lunar sample catalogue, and personal inspection of prospective samples while visiting the NASA Johnson Space Centre. The samples are mainly anorthosite, but some gabbro, basalt, impact melt rock, and breccia are also included (see Table 3-1). Samples were specifically selected to collect the widest possible range of optical deformation (shock effects).

All lunar plagioclase grains observed were perfect structural matches for anorthite by μXRD, which matches with reported compositions of An_{89-99} for these samples (e.g., Dixon and Papike, 1975; Steele and Smith, 1973; Warren and Wasson, 1978, 1977; Warren et al., 1982). Plagioclase grains from Mistastin varied between andesine (An_{31-49}) and labradorite (An_{50-55}) (Chapter 2).

Table 3-1: Apollo sample list: signs of strain; number of grains in each group per thin section; and FWHMχ measurements.

Sample number	Origin (Apollo mission)	Rock type	Optical effects					Optical Group (# of grains)				Average FWHM (°χ)
			Fracture	Undulose extinction	Mosaicism	Bent twins	Partially Isotropic	A	B	C	D	
10047,16	Adjacent to LM (11)	Ilmenite basalt		x					1			0.79
12054,126	Surveyor Crater (12)	Ilmenite basalt	x	x						2		6.19
15362,11	Spur Crater (15)	Anorthosite (F)	x	x					1	4		1.76
15415,90	Spur Crater (15)	Anorthosite (F)	x	x		x				4		1.59
15684,4	Station 9A (15)	Basalt	x	x			x			1	3	3.41
60015,114	~30 m from LM* (16)	Anorthosite	x	x	x					6		6.76
60025,230	~15 m from LM (16)	Anorthosite	x	x	x					3		1.53
60055,4	~170 m from LM (16)	Anorthosite	x	x						6		0.89
60215,13	Station 10 (16)	An breccia	x	x	x	x			1	4		1.52
60618,4	~70 m from LM (16)	Anorthosite	x	x		x				5		2.41
60619,2	70 m from LM (16)	Anorthosite	x					6	3			0.75
60629,2	Near LM (16)	Anorthosite (F)	x	x		x				3		3.26
62237,21	Buster Crater, St. 2 (16)	Anorthosite (F)	x	x					2	15		1.62
67075,41	North Ray Crater (16)	Anorthosite (F)	x	x		x			1	4		1.47
67415,113	North Ray Crater (16)	Anorthosite (N)	x	x				1	5	1		0.89
67746,12	North Ray Crater (16)	Anorthosite (N)		x					6			0.57
68035,6	Station 8 (16)	Anorthosite	X	x		x				7		3.12
69955,27	Station 9 (16)	Anorthosite	x	x	x					6		4.99
69955,29	Station 9 (16)	Anorthosite	x	x	x					6		5.13
73215,193	Lara Crater (17)	Impact melt breccia	x	x				1	1	5		3.41
76335,55	Station 6 (17)	Anorthosite (M)	x	x						6		1.97
79155,58	Station 9 (17)	Gabbro	x	x			x				6	4.81

Abbreviations: LM=Lunar Module; F=Ferroan; M=Magnesian; N=Noritic; An=Anorthosite

*Probably collection location, but details of its collection, situation, and orientation are not known

Polished thin sections were examined for microscopic shock metamorphic effects, using a Nikon Eclipse LV100POL compound petrographic microscope. Chemical compositions of lunar samples were taken from values reported by previous authors.

Micro-X-ray diffraction (μXRD) analyses were carried out on a Bruker D8 Discover diffractometer with theta-theta instrument geometry, which enabled the sample to remain horizontal and stationary while the source and detector rotated. It has a sealed Cobalt source, Gobel mirror parallel beam optics, an exchangeable pinhole collimator (100 or 300 μm), and two-dimensional (2-D) General Area Detector Diffraction System (GADDS). Omega scans were used, wherein the source and detector rotate simultaneously, both clockwise, through a specified number of degrees (Omega angle, ω) to simulate rotation of the sample. Counting time was 30 minutes for GADDS frame 1 (θ_1=14.5°, θ_2=16°, ω=6) and 45 minutes for GADDS frame 2 (θ_1=30°, θ_2=40°, ω=23). Large grains of plagioclase (generally >300 μm) were selected for analysis in order to ensure that the X-ray beam was interacting with only (or mainly) the chosen mineral, enabling optically observed signs of strain-related mosaic spread (undulose extinction) to be directly correlated with μXRD patterns. This allowed for observation of the same effect with two techniques, enabling quantification of optical observations of strain.

Using 2D GADDS images, spots or streaks were integrated along the length of the Debye rings (chi dimension, χ). The resulting lineshapes had their background subtracted and were smoothed by a factor of 0.15 using a Savitzky-Golay algorithm (Savitzky and Golay, 1964) to reduce interference of the noise with measuring the FWHMχ (Figure 3-1). Streak length was quantified by measuring peak full-width at half maximum chi (FWHMχ) using Bruker AXS Diffracplus EVA software in the manner of Izawa et al. (2011). In cases of asterism, the FWHMχ of each individual peak was measured and then the individual values for a single row were summed to reconstruct the width of the original peak prior to subdomain formation, as a proxy for determining the original strain-related mosaic spread, in the manner of Vinet et al. (2011). The smoothing and FWHMχ measurement functions are built-in operations of the Bruker AXS DiffracPLUS EVA software. Further details of the technique and μXRD are given by Flemming (2007) and Izawa et al. (2011).

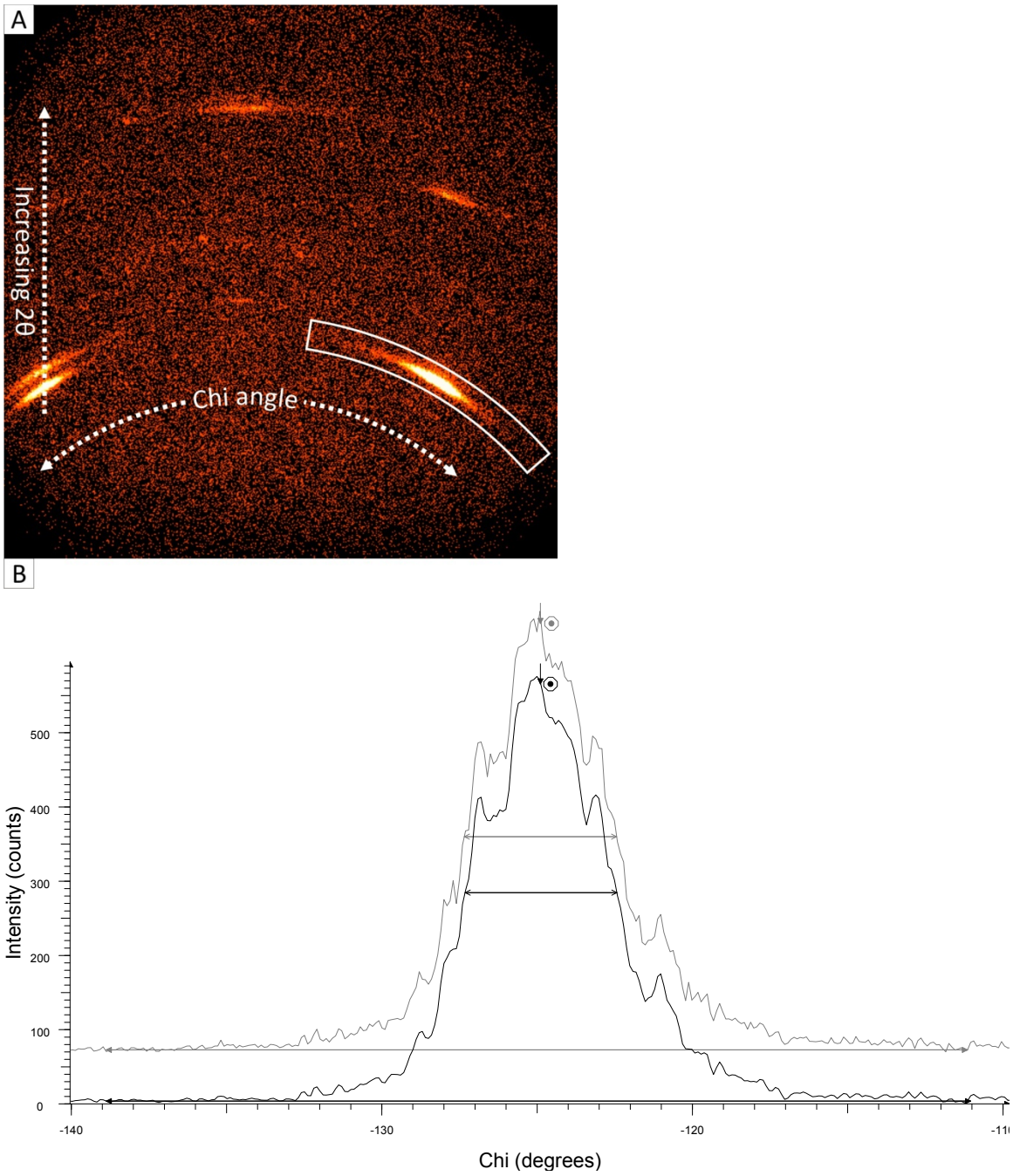

Figure 3-1: µXRD GADDS image and stacked plots of intensity vs. °χ. A) µXRD GADDS image of an anorthite crystal in Apollo sample 60015,114. Arrows indicate the direction of chi and increasing 2θ. White box highlights the streak, which is integrated in 2θ and displayed in figure B. B) Stacked plots of intensity vs. °χ showing raw (grey), smoothed and background subtracted (black) lineshapes, and streak length measurement (FWHMχ) for both. In this case, the raw (grey) FWHMχ is 4.92° and the processed (black) FWHM chi is 4.90°.

Error in the FWHMχ values comes from systematic measurement error of ±0.01 °χ, based on the measurement resolution of the software, and from the signal to noise ratio, based on the crystallinity of the sample and the diffraction run-time. Signal to noise error was calculated by measuring the FWHMχ with the baseline at three different locations: the top of the noise, the middle of the noise, and the bottom of the noise. The difference between the maximum/minimum measured FWHMχ and the middle FWHMχ was taken for the positive/negative error, respectively. Error is reduced to near 0 with high signal to noise, as with high intensity spots or streaks. However, intensity decreases with increased strain related mosaicity (increased streak length), so the longer streaks tend to have a lower signal to noise ratio and, therefore, greater error associated with the measurement of the FWHMχ. The average error is less than 0.5°, with the maximum error being 2.5°.

Observed lattice planes were indexed using the following ICDD cards: 01-079-1148 (C)-Andesine; 00-041-1486 (*)-Anorthite; and 01-083-1417 (C)-Labradorite. Eight Miller indices were analyzed in total: $(\bar{2}02)$, (004), $(1\bar{5}2)$, $(53\bar{6})$, $(\bar{3}14)$, $(42\bar{4})$, $(0\bar{6}4)$, and $(2\bar{7}3)$, these were chosen because they are the most frequently occurring peaks in all collected data.

3.4 Results

A wide variety of optical signs of strain were observed in both Mistastin and Apollo samples, ranging from uniform extinction to fully isotropic (diaplectic plagioclase glass). Individual crystals of andesine, labradorite, and anorthite were divided into 5 groups (A-E) based on common optical indicators of strain (see sections 3.4.1-3.4.5, Figure 3-2). Letters assigned to the groups purposely increase from A to E in order of increasing apparent degree of deformation.

The $FWHM_{\chi}$ of streaks from the eight most commonly detected Miller indices of andesine, labradorite, and anorthite grains were measured to quantify shock-induced strain-related mosaic spread in a similar manner to that employed for enstatite by Izawa et al. (2011). The results of these measurements are summarized in Figure 3-3 and Tables 3-1, and 3-2. As there is significant overlap each group compared, we report only average values, not upper or lower boundaries for each group (Table 3-2).

Figure 3-2: Representative photomicrographs in cross-polarized light of each optical group, correlated with GADDS images from each grain pictured. Note how the pattern on the GADDS images goes from spots (A) to short streaks (B) to long streaks (C & D) to an amorphous diffuse band (E). The location of the analysis is indicated by a circle on each image, the circle represents the beam diameter of 300 µm. A) Apollo sample 60619,2 shows uniform extinction under cross polarized light, and spots on the GADDS image. B) Apollo sample 15415,90 shows slight undulose extinction, and the beginning of streaks on the GADDS image in which the bright spots are slightly longer than they are wide – 'lozenge-shaped'. C) Apollo sample 76335,55 shows extremely undulose, bordering on mosaic extinction, and long streaks with the start of asterism on the GADDS image. D) i) Apollo sample 79155,58 shows a grain which has become partially isotropic (black), while part remains birefringent (centre of circle); the GADDS image, which was centred on the remaining birefringent part of the crystal, shows longer streaks than those in A-C. D) ii) Mistastin sample MM10-11 shows a partially isotropic grain from the demonstrating crystallographic control of isotropization, with two sets of alternate twins being diaplectic glass. The GADDS image shows medium length streaks. In this case, orientational effects from beam overlap with multiple twins is negated by the amorphous nature of the twins. E) Mistastin sample MM10-38 has had all plagioclase converted to diaplectic glass. The left photomicrograph shows preservation of textures in plane polarized light and the right image shows total extinction of plagioclase under cross-polarized light. The GADDS image shows an amorphous band through the centre of the image, indicative of an amorphous XRD pattern.

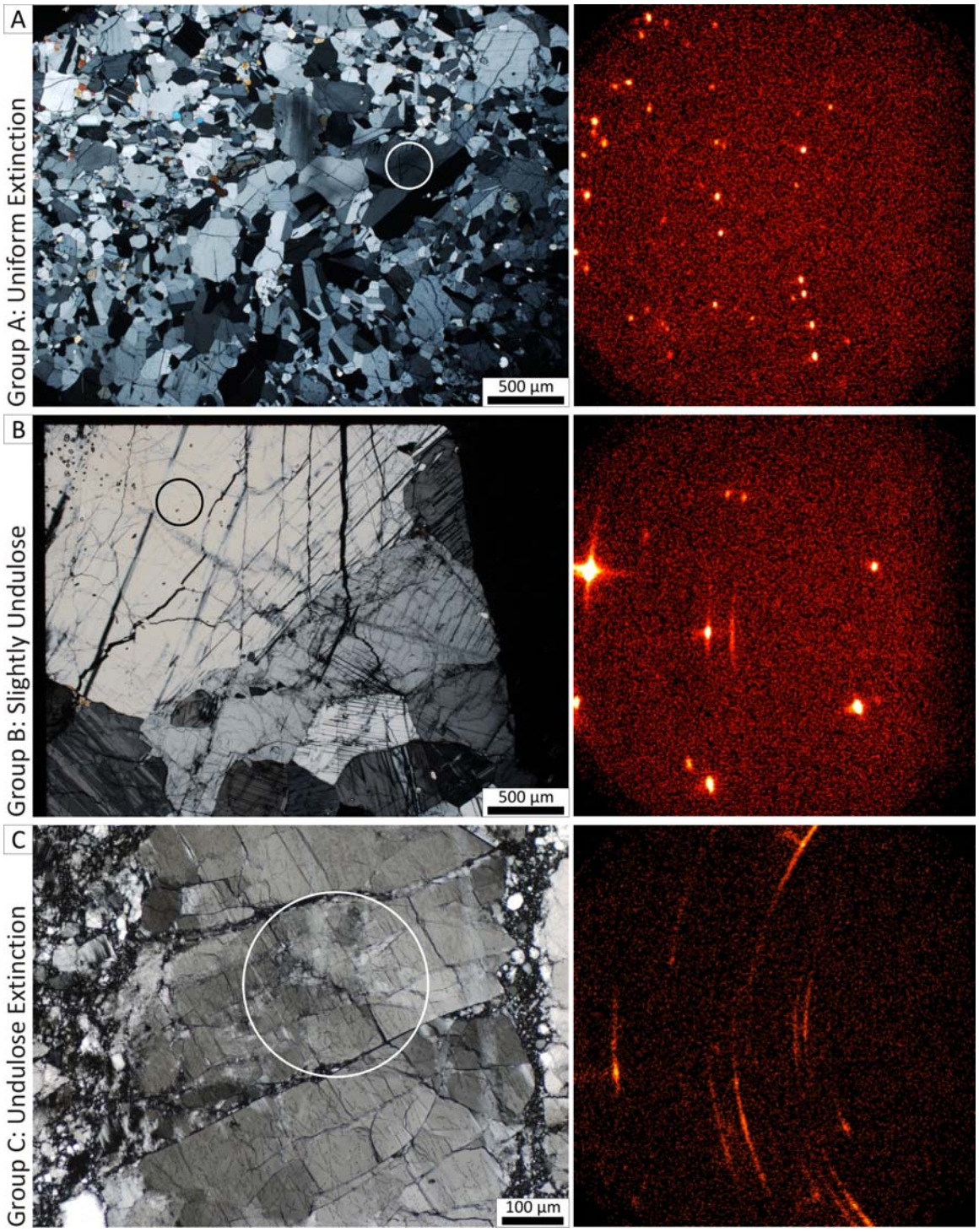
A
Group A: Uniform Extinction
500 µm
B
Group B: Slightly Undulose
500 µm
C
Group C: Undulose Extinction
100 µm

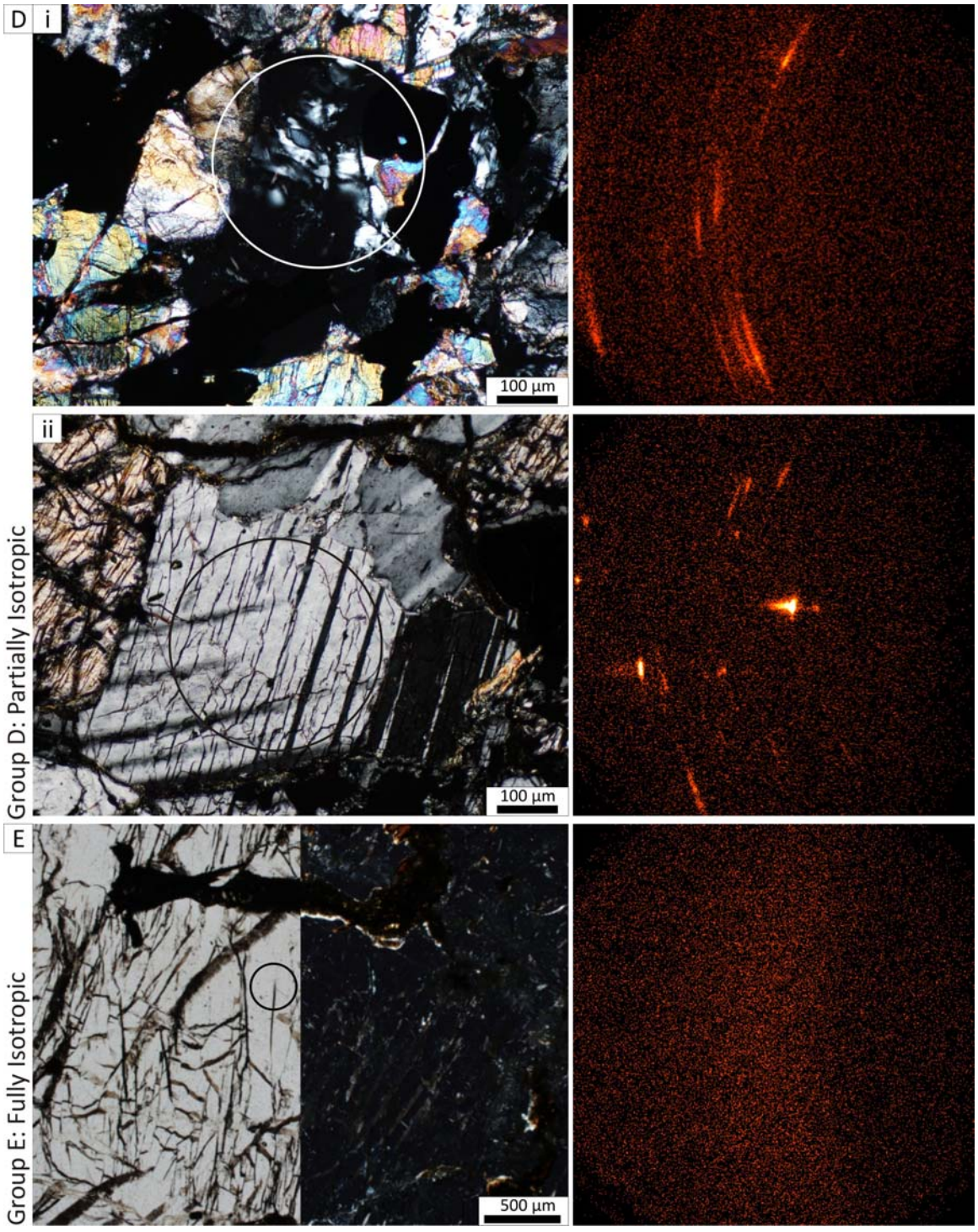
D
i
100 µm
ii
100 µm
Group D: Partially Isotropic
E
500 µm
Group E: Fully Isotropic

Table 3-2: Average across all Miller indices of FWHMχ measurements for optical groups.

O.G.	Description	Average FWHMχ (°χ) Apollo	s.d.	Mistastin	s.d.	Number of Spots Apollo	Mistastin
A	Uniform extinction	0.79	0.32	0.67	0.23	16	8
B	Slight undulose extinction	0.93	0.40	0.89	0.46	10	18
C	Undulose extinction	2.58	2.03	1.07	0.80	65	15
D	Partially isotropic	3.14	1.39	2.54	1.77	8	8
E	Diaplectic glass	N/A		N/A		N/A	N/A

Abbreviations: O.G.=Optical Group; s.d. = standard deviation (1σ); N/A = Not applicable

3.4.1 Group A – Uniform Extinction

Grains exhibiting uniform extinction are characterized by the entire grain becoming extinct at the same time on rotation of the stage under cross-polarized light (Figure 3-2A). All grains in this group showed low degrees of fracturing, distinctly less than those of other groups. GADDS images of grains in this group show clear individual spots (Figure 3-2A). The average FWHMχ was 0.67°χ for Mistastin Lake, and 0.79°χ for Apollo.

3.4.2 Group B – Slight Undulose Extinction

Grains exhibiting slightly undulose extinction are characterized by rotation of the stage by only 1-2°, causing a wave of extinction to pass through the entire grain (Figure 3-2B). Most grains in this group show irregular fracturing. GADDS images of grains in this group show spots, which are beginning to streak out into 'lozenges' that are slightly longer than they are wide. The average FWHMχ was 0.89°χ for Mistastin Lake, and 0.93°χ for Apollo.

3.4.3 Group C – Undulose Extinction

Grains exhibiting undulose extinction are characterized by a wave of extinction passing through the grain on rotation of the stage by ~5-30° (Figure 3-2C), typical of 'classic' undulose extinction. The upper limit to this group is grains that are beginning to show

signs of mosaic extinction, in which waves of extinction pass through different parts of the grain in different directions. The majority of these grains exhibit irregular fracturing; approximately half show bent and/or offset twins. GADDS images of grains in this group clearly show streaks, which are much longer than they are wide, and some have begun to show asterism, in which the streaks have resolved into short rows of spots (Figure 3-2C). The average FWHMχ was 1.07°χ for Mistastin Lake, and 2.58°χ for Apollo.

3.4.4 Group D – Partially Isotropic

Grains that have become partially isotropic are characterized by only part of the crystal being isotropic, while the remainder remains birefringent under cross-polarized light. In the Apollo samples for this group, there appears to be no crystallographic control on which parts are isotropic (Figure 3-2Di), meaning that the isotropic areas are not confined by linear or planar elements. In the Mistastin samples, there is generally no apparent crystallographic control on which part of the grain becomes isotropic but, occasionally, it is only the alternate twins that are amorphized, leaving the remainder of the crystal birefringent (Figure 3-2Dii). These grains exhibit irregular fracturing and undulose extinction in the remaining birefringent part. GADDS images of grains in this group show clear streaks, very similar to those exhibited by Group C. The average FWHMχ was 2.54°χ for Mistastin Lake, and 3.14°χ for Apollo.

3.4.5 Group E – Diaplectic Glass

Grains that have become fully isotropic were not found in any of the Apollo samples examined for this study, but were present in many of the Mistastin thin sections (Figure 3-2E). They are characterized by complete extinction of the grain on rotation under cross-polarized light, the production of an amorphous X-ray pattern, and a homogenous chemical composition matching that of plagioclase feldspar (Chapter 2, Table 2-3). Due to the amorphous pattern produced by μXRD, no streaks or spots occur in the resulting GADDS image; as a result no measurement in chi or 2-theta is possible with these samples.

3.4.6 $FWHM_{\chi}$ Measurements

As seen in Figure 3-3, there is significant overlap in FWHMχ between the various groups; however, the maximum values in each optical group, and the averages in each optical group, form a general upward trend in both Apollo and Mistastin suites. Optical groups have been purposely arranged in order of increasing apparent deformation (based on petrographic observations). A deviation in the trend of maximum values is clear in Group C of the Apollo suite, in which the maximum value is nearly twice the maximum value of Group D. However, the average values for Group C and D are the same within error. In each optical group, the maximum streak length is higher in the Apollo suite than in the Mistastin suite, though the difference is so slight as to be dwarfed by the measurement error in all but Group C. There is significant scatter in Group C in both suites.

The biggest variation in streak length with optical group is apparent in these Miller indices: $(\bar{2}02)$, (004), $(1\bar{5}2)$, and $(53\bar{6})$. The Miller indices displayed in Figure 3-3 were chosen based on which occurred in all optical groups and which showed the widest range in streak lengths (e.g., those indices which varied over >1-2° FWHMχ across optical groups (Appendix C)). Some indices plotted demonstrated very little variation, and these were commonly those with higher integers as part of their Miller index (e.g., $(2\bar{7}3)$, $(42\bar{4})$).

The average values for FWHMχ are very similar between the Apollo and Mistastin suites (Table 3-2). The variations between sample suites in Groups A and C, however, suggest that further study is required to constrain the significance of these values (see section 3.6). There is an overall correlation between increased strain and increased average streak length (Figure 3-3).

Figure 3-3: Graphs of FWHMχ vs. optical group for samples from the Mistastin suite and the Apollo suite. The four Miller indices displayed (in brackets) are those which are represented in every optical group. Different symbols indicate the Miller index of streaks measured from diffraction of different sets of crystal planes. The average of each set is indicated by a black bar. A=Uniform extinction; B=Slight undulose extinction; C=Undulose extinction; D=Grains which have become partially isotropic; and E=Grains which have become fully isotropic (not shown due to amorphous nature of the μXRD pattern). Also indicated is the shock level of each set according to Stöffler (1971). Note that in both suites there is a general upward trend from group A to group D (which are arranged in order of increasing apparent optical deformation). In Group C, there is significant difference between FWHMχ measurements in the Apollo suite compared to the Mistastin suite. There is significant scatter in the FWHMχ values for group C in the Apollo suite. Error bars are the difference between the widest/narrowest possible FWHMχ (baseline set to bottom/top of noise, respectively) and the average FWHMχ (baseline set to middle of noise).

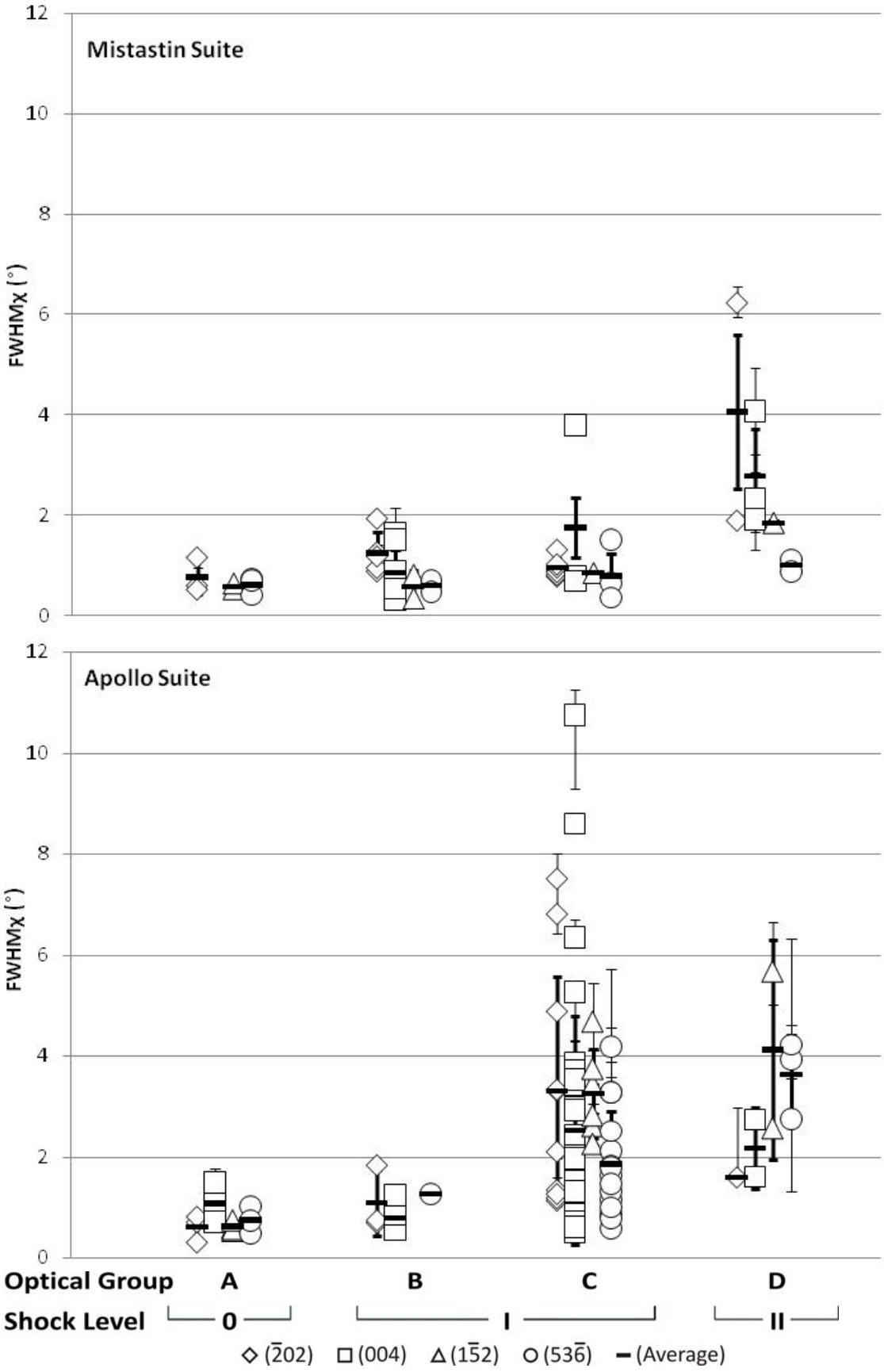
Mistastin Suite
Apollo Suite
FWHMχ (°)
0
2
4
6
8
10
12
Optical Group
A
B
C
D
Shock Level
0
I
II
◇ (2̄02)
□ (004)
△ (1 5̄2)
○ (53 6̄)
– (Average)

Due to the large beam size, relative to the width of most polysynthetic twins, it is apparent that several GADDS images picked up both sets of twins. This is evidenced by repetition of the pattern at lower intensity slightly offset from the higher intensity spots or streaks from the twin taking up the majority of the space with which the beam interacted. In these cases, or when adjacent twins were both analyzed on purpose, in order to determine if alternate twins deform differently from each other under shock conditions, the GADDS images indicate that alternating twins typically exhibit the same amount of strain-related mosaicity as one another. Notable exceptions to this are cases in which alternate twin deformation is optically apparent such as preferential isotropization or zeolitization of alternate twin sets (Chapter 2, Figure 3-2D).

3.5 Discussion

As evidenced by Figure 3-3, FWHMχ measurements along the Debye rings of $(\bar{2}02)$, (004), $(1\bar{5}2)$, and $(53\bar{6})$ show a general upward trend with optically observed indicators of increasing strain. The Miller indices that demonstrated very little variation across optical groups (not plotted in Figure 3-3, but shown in Appendix C) were those that were not represented in every optical group and frequently those that had higher integers as part of their Miller index: $(\bar{3}14)$, $(42\bar{4})$, $(0\bar{6}4)$, $(2\bar{7}3)$. We hypothesize that the decreased variation in streak length with higher integers in the Miller index is a result of the smaller interplanar lattice spacing resulting in less deviation under non-uniform strain.

Comparisons of FWHMχ measurements of neighbouring twins indicate that twins generally deform in a similar fashion, as evidenced by matching streak lengths from each twin. This suggests that the difference in lattice orientation relative to the shockwave that allows some twins to isotropize or develop planar deformation features (e.g., Stöffler, 1966; Taylor and Dence, 1969), while leaving others crystalline, occurs over a very narrow range of orientations. This phenomenon warrants further investigation.

3.5.1 Scatter in FWHMχ measurements

There is a high degree of scatter in FWHMχ measurements from groups B to D. Scatter seems to increase with increasing apparent optical shock level. There are two explanations for this: subjectivity of optical group determination, and orientation of the sample.

Subjectivity of optical group determination: The optical groups created for this study were based on observations of commonly occurring characteristics across the 189 grains examined in this study (102 from the Apollo suite, 87 from the Mistastin Lake suite). Overlap in streak lengths is accounted for by the highly gradational difference between categories, such as uniform extinction (Group A) and slight undulose extinction (Group B) and between slight undulose extinction (Group B) and undulose extinction (Group C).

Orientation of the sample: A result of the geometry of μXRD, as applied to *in-situ* samples, is that the possible orientations of the crystal lattice relative to the X-ray beam are necessarily restricted by the orientation of the crystal within the sample and, in the case of thin sections, by the orientation of the crystal relative to the plane of the cut sample surface. This necessarily induces scatter in the measurements, because not only is passage of the shockwave through materials known to be inhomogeneous, but the degree to which the crystal lattice is strained is also anisotropic. As a result, if the X-ray beam is interacting with the crystal lattice perpendicular to the direction of primary stress, the degree of streaking will be more extensive than if the X-ray beam is in the same plane as the direction of stress. The use of randomly oriented crystals in this study means that statistically speaking the bulk of the FWHMχ measurements will fall somewhere between this minimum value (X-rays parallel to direction of strain) and the maximum value (X-rays perpendicular to the direction of strain). As the crystals are not all oriented in the same way relative to the X-rays, this undoubtedly creates a great deal of scatter in the measured FWHMχ.

3.5.2 Subdivision of the lower end of the shock scale

The wide variation in streak length exhibited by grains in Group C (undulose extinction), particularly in the Apollo sample suite, indicates that there is more variation in

crystallographic strain and, therefore, shock pressure than is apparent using conventional optical microscopy. Micro-X-ray diffraction (μXRD) is therefore be an excellent mechanism by which to subdivide the lower end of the shock scale. This is of particular importance as the currently most widely used shock scale for plagioclase consists of only essentially three categories: 0 – unshocked; I – undulose extinction, PDFs; II – diaplectic glass (Stöffler, 1971). This means that we have only a limited ability to constrain shock information prior to isotropization, although the majority of samples fall into this intermediate zone.

Streak lengthening in χ on 2-dimensional μXRD GADDS images displaying strain-related mosaicity demonstrate that there is a wide range of streak lengths displayed by grains, consistent with optical undulose extinction (Group C). While this is not a unique indicator of shock metamorphism, this technique has the possibility to enable subdivision of the low end of the pressure scale due to the high range of streak lengths. A consistent, quantifiable, and easily applicable system to define the level of undulosity is currently lacking. One method could be to record the angular difference between when one part of the grain is extinct and when the next part is extinct; however, this would need to take into account the size of the grain in question as well, as smaller grains would necessarily be rotated less than larger grains, in order to sweep through the entire range of extinction angles.

3.5.3 Comparison of deformation in Lunar and Terrestrial Plagioclase

As seen in Figure 3-3, the samples from the Apollo suite show much higher levels of strain-related mosaicity in Group C than those of the Mistastin suite. It seems likely that the higher level of strain in lunar samples, as compared with terrestrial samples, is a result of multiple impacts which undoubtedly affected all of the Apollo samples; whereas, we know that the Mistastin samples have only experienced one impact and that there was no other tectonic activity to account for multiple generations of strain-related mosaicity. In thinking about the question of why lunar samples would be able to strain more than terrestrial samples without becoming isotropic (maximum in Group C of Apollo suite is nearly twice that of Group D in Apollo suite), the answer seems to lie with

composition. Apollo samples are all anorthite, while Mistastin samples are labradorite or andesine.

The increased maxima in Group C of the Apollo suite (Figure 3-3) is thought to be tied to multiple impact events resulting in higher overall strain and to the increased Ca content of the Apollo suite as compared to the Mistastin suite. Due to the smaller maximum streak lengths in Group D as compared to Group C in the Apollo suite, we suggest that the partial isotropization of these has crystals relieved enough pressure to allow the remaining birefringent part of the grain to remain relatively unstrained.

3.6 Concluding Remarks/Future Work

We have shown that the degree of strain in plagioclase feldspar can be quantified through the use of *in-situ* micro-X-ray diffraction. One should be mindful, however, that streaking in chi can result from non-uniform strain caused by multiple factors, including endogenically, and not only by the passage of a shockwave during meteorite impact.

An ideal follow-up would be to experimentally shock each composition of feldspar to various peak pressures and then conduct μXRD and petrographic studies on those samples to see how shock of known pressures affects each group and compare the results of each group to each other, in order to better understand how composition (and therefore mineral structure) affects shock as seen by strain-related mosaicity. Additionally, examining the same spots as in this study, but with different techniques would provide an excellent additional quantitative dataset with which to compare the μXRD-generated FWHMχ values reported herein. Raman spectra, for example, show increased peak broadening and decreased intensity with increasing shock level (Fritz et al., 2005); if Raman spectra were to be gathered from the same spots as used in this study, the FWHM of the Raman bands could be plotted against the FWHMχ of the μXRD patterns and this might better constrain the groups used in this study; as well as, possibly illuminating trends or clusters which are not currently distinguishable. It is possible that a follow-up

study of this kind would result in clear natural divisions becoming apparent for the lower end of the shock scale (level I according to Stöffler, 1971).

Pursuant to increasing the statistical reliability of this technique for quantification of shock and shock scale subdivision, measuring more grains may help to constrain which Miller indices are most useful, and to better define ranges of streak lengths for each optical group.

3.7 References

Beaty D. W., and Albee A. L. 1978. Comparative petrology and possible genetic relations among the Apollo 11 basalts. *Proceedings of the 9th Lunar and Planetary Science Conference* 359–463.

Currie K. L. 1971. Geology of the resurgent cryptoexplosion crater at Mistastin Lake, Labrador. *Bulletin - Geological Survey of Canada* 207: 62 p.

Dixon J. R., and Papike J. J. 1975. Petrology of anorthosites from the Descartes region of the moon: Apollo 16. *Proceedings of the 6th Lunar Science Conference* 263–291.

Emslie R. F., and Stirling J. A. R. 1993. Rapakivi and related granitoids of the Nain plutonic suite: geochemistry, mineral assemblages and fluid equilibria. *The Canadian Mineralogist* 31: 821–847.

Ferrière L., Morrow J. R., Amgaa T., and Koeberl C. 2009. Systematic study of universal-stage measurements of planar deformation features in shocked quartz: Implications for statistical significance and representation of results. *Meteoritics & Planetary Science* 44: 925–940.

Flemming R. L. 2007. Micro X-ray diffraction (μXRD); a versatile technique for charcterization of Earth and planetary materials. *Canadian Journal of Earth Sciences* 44: 1333–1346.

French B. M., and Koeberl C. 2010. The convincing identification of terrestrial meteorite impact structures: What works, what doesn't, and why. *Earth-Science Reviews* 98: 123–170.

Fritz J., Greshake A., and Stöffler D. 2005. Micro-Raman spectroscopy of plagioclase and maskelynite in Martian meteorites: Evidence of progressive shock metamorphism. *Antarctic Meteorite Research* 18: 96–116.

Grieve R. A. F. 2006.*Impact Structures in Canada*, Geological Association of Canada. 210 p.

Gucsik A., Ninagawa K., Nishido H., Toyoda S., Tsuchiyama A., Bidló A., and Brezsnyánszky K. 2004. Cathodoluminescence (CL) spectral study of experimentally shock-deformed plagioclase. In *Workshop on Chondrites and Protoplanetary Disk*. Houston, TX, United States (USA): Lunar and Planetary Institute, Houston, TX. p. Abstract #9012.

Haskin L. A., Korotev R. L., Gillis J. J., and Jolliff B. L. 2002. Stratigraphies of Apollo and Luna highland landing sites and provenances of materials from the perspective of basin impact ejecta modeling. In *Lunar and Planetary Science Conference XXXIII*. Abstract #1364.

Head J. W. 1974. Lunar dark-mantle deposits-Possible clues to the distribution of early mare deposits. *Proceedings of the Fifth Lunar Conference (Supplement 5, Geochimica et Cosmochimica Acta)* 1: 207–222.

Head J. W. 1977. Some geologic observations concerning lunar geophysical models edited by Pomeroy J. H., and Hubbard N. J. *NASA Special Publication* 370 (Part 1), 407–416.

Hiesinger H., and Head J. W. 2006. New views of lunar geoscience: an introduction and overview. *Reviews in Mineralogy and Geochemistry* 60: 1–81.

Hörz F., and Quaide W. L. 1973. Debye-Scherrer investigations of experimentally shocked silicates. *The Moon* 6: 45–82.

Izawa M. R. M., Flemming R. L., Banerjee N. R., and McCausland P. J. A. 2011. Micro-X-ray diffraction assessment of shock stage in enstatite chondrites. *Meteoritics & Planetary Science* 46: 638–651.

Jaret S., Kah L. C., and French B. M. 2009. Feldspar deformation as an indicator of low-barometry shock: petrographic investigation of ejecta from the Tenoumer impact crater, Mauritania. In *Geological Society of America Abstracts with Programs*. p. 313.

Kayama M., Nishido H., Sekine T., Nakazato T., Gucsik A., and Ninagawa K. 2012. Shock barometer using cathodoluminescence of alkali feldspar. *Journal of Geophysical Research* 117: E09004.

Mak E., York D., Grieve R. A. F., and Dence M. 1976. The age of the Mistastin Lake crater, Labrador, Canada. *Earth and Planetary Science Letters* 31: 345–357.

McCausland P. J. A., Flemming R. L., and Izawa M. R. M. 2010. Quantitative shock stage assessment in olivine and pyroxene bearing meteorites via in situ micro-XRD. In *American Geophysical Union, Fall Meeting 2010, abstract #P14C-03*.

Savitzky A., and Golay M. J. E. 1964. Smoothing and Differentiation of Data by Simplified Least Squares Procedures. *Analytical Chemistry* 36: 1627–1639.

Smith J. V, Anderson A. T., Newton R. C., Olsen E. J., Wyllie P. J., Crewe A. V, Isaacson M. S., and Johnson D. 1970. Petrologic history of the moon inferred from petrography, mineralogy and petrogenesis of Apollo 11 rocks. *Proceedings of the Apollo 11 Science Conference* 1: 897–925.

Spudis P. D. 1984. Apollo 16 site geology and impact melts: Implications for the geologic history of the lunar highlands. *Proceedings of the 15th Lunar and Planetary Science Conference* C95–C107.

Steele I. M., and Smith J. V. 1973. Mineralogy and petrology of some Apollo 16 rocks and fines: General petrologic model of moon. *Proceedings of the 4th Lunar Science Conference* 1: 519–536.

Stöffler D. 1971. Progressive metamorphism and classification of shocked and brecciated crystalline rocks at impact craters. *Journal of Geophysical Research* 76: 5541–5551.

Stöffler D. 1966. Zones of impact metamorphism in the crystalline rocks of the Nördlinger Ries crater. *Contributions to Mineralogy and Petrology* 12: 15–24.

Taylor F. C., and Dence M. R. 1969. A probable meteorite origin for Mistastin Lake, Labrador. *Canadian Journal of Earth Sciences* 6: 39–45.

Vinet N., Flemming R. L., and Higgins M. D. 2011. Crystal structure, mosaicity, and strain analysis of Hawaiian olivines using in situ X-ray diffraction. *American Mineralogist* 96: 486–497.

Warren P. H., Taylor G. J., Keil K., Marshall C., and Wasson J. T. 1982. Foraging westward for pristine nonmare rocks-Complications for petrogenetic models. *Proceedings of the 12th Lunar and Planetary Science Conference* 21–40.

Warren P. H., and Wasson J. T. 1978. Compositional-petrographic investigation of pristine nonmare rocks. *Proceedings of the 9th Lunar and Planetary Science Conference* 185–217.

Warren P. H., and Wasson J. T. 1977. Pristine nonmare rocks and the nature of the lunar crust. *Proceedings of the 8th Lunar Science Conference1* 2215–2235.

Wood J. A., Dickey J. S., Marvin U. B., and Powell B. N. 1970. Lunar anorthosites and a geophysical model of the moon. *Proceedings of the Apollo 11 Science Conference* 1: 965–988.

Young K. E., Hodges K. V, van Soest M. C., and Osinski G. R. 2013. Dating the Mistastin Lake impact structure, Labrador, Canada, using zircon (U-Th)/He thermochronology. In *44th Lunar and Planetary Science Conference*. Abstract #2426.

Chapter 4

4 Discussion and Conclusions

4.1 Introduction

The objectives of this thesis were to: a) develop a more quantitative scale of shock deformation in feldspar group minerals; b) expand the utility of feldspar for determining shock level in quartz-limited systems; and c) determine whether micro-X-ray diffraction is effective in evaluating shock in feldspars. To achieve these objectives, a comprehensive optical examination of shocked plagioclase from the Mistastin Lake impact structure was conducted in conjunction with follow-up scanning electron microscopy, cathodoluminescence, and electron-probe microanalysis (Chapter 2). Measurement of strain-related mosaicity from two-dimensional micro-X-ray diffraction (μXRD) images of shocked lunar and terrestrial plagioclase was correlated to optical observations of strain (Chapter 3). Below, I outline how the objectives of this thesis have been met, and suggest follow-up work that will contribute to the further development of feldspars, plagioclase in particular, as a shock barometer.

4.2 Developing a quantitative scale of shock deformation in feldspars

Currently the most widely used scheme for assigning shock level is that suggested by Stöffler (1971). According to that scheme, feldspars can be shock level: 0 – unshocked; I – shocked, but not yet diaplectic glass (e.g., undulose extinction, planar deformation features); II – diaplectic glass. This largely stems from the lack of diversity of optical features that are displayed by shocked feldspar prior to becoming diaplectic glass. However, the wide variation in FWHMχ measurements of plagioclases in this group (optical groups B and C of Chapter 3) demonstrates that there are microstructural changes occurring as pressure increases until the point of isotropization. Chapter 3 successfully shows that the degree of strain in plagioclase feldspar can be quantified through use of *in-situ* micro-X-ray diffraction (μXRD). Within the scope of this work, quantification of the

optical groups was accomplished through use of FWHMχ measurements of strain-related mosaic spread, and average FWHMχ were shown. Upper and lower boundaries, however, were not determined. With further study, a more quantitative scale can be developed.

The wide variation in streak length exhibited by optical groups which appear to have been exposed to higher pressures (i.e., those exhibiting undulose extinction and partial isotropization), suggests that there is ample room to subdivide the lower end of the shock scale using μXRD. Further development of this technique and division of FWHMχ measurements into smaller groups, along with calibrating this technique using experimentally shocked samples, will allow for a more definitive and quantitative subdivision of the shock scale.

4.3 The utility of feldspar for determining shock level in quartz-limited systems

This preliminary quantitative scale of shock metamorphism of feldspar using micro-X-ray diffraction has already expanded the usefulness of feldspar for determining shock level. This is particularly important for rare and precious samples, such as those returned during the Apollo missions.

Diaplectic glass is still the most widely recognized shock metamorphic feature in plagioclase feldspar. Non-shock diagnostic features, such as fracturing and undulatory extinction, can be indicative of the degree of shock which minerals have experienced, but clearly should not be relied upon unless it is already known that the minerals in question were affected by passage of a shock wave.

4.3.1 Planar deformation features

The scarcity of planar deformation features (PDFs) in plagioclase from both Mistastin Lake and the Apollo samples examined in this study indicates significant compositional and, correspondingly, structural, control over which shock effects develop in the various minerals of the feldspar group. Three possible explanations are put forth to explain the absence of PDFs in plagioclase in close proximity to ubiquitous PDFs in quartz: 1) PDFs

form in plagioclase much less frequently than in quartz; 2) PDFs in plagioclase are more difficult to recognize than PDFs in quartz; 3) PDFs are more easily destroyed in plagioclase than in quartz. However, annealing (and erasure) of PDFs is unlikely at Mistastin Lake, due to the lack of significant post-impact thermal activity (Bielecki et al., 1980; Taylor and Dence, 1969), and the exceptional preservation of PDFs in quartz at Mistastin. It is, therefore, more probable that one or both of the first two hypotheses are true.

Planar deformation features (PDFs) forming less frequently in plagioclase than in quartz might be an effect of crystal symmetry. It is a distinct possibility that higher crystal symmetry than triclinic is a pre-requisite for the development of PDFs, as suggested by reports of PDFs in diopside (monoclinic); olivine, sillimanite, cordierite (orthorhombic); garnet (isometric); zircon (tetragonal); and apatite, quartz (hexagonal) (e.g., Bohor et al., 1993; Dressler, 1990; Dworak, 1969; Nesse, 2004; Stöffler, 1974, 1972; Stöffler et al., 1991). This would explain the lack of PDFs observed in plagioclase feldspars, as compared to those observed in alkali feldspars and other minerals.

PDFs maybe be masked, or their formation prevented, in plagioclase by the presence of pre-existing planes of weakness such as twin and cleavage planes. If PDFs form along these planes, they will be difficult to identify using optical techniques (due to masking). If PDFs form as a mechanism for pressure release in other minerals, as has been suggested by some (e.g., Goltrant et al., 1992), then perhaps the pre-existing planes of weakness in the crystal structure provide the necessary release and preclude the formation of PDFs altogether. All of this is not to say that plagioclase feldspars never form PDFs, only that they are far less common, and that they probably form under a much narrower range of pressure conditions than PDFs in quartz and other minerals (Ostertag, 1983).

4.3.2 Diaplectic Glass

Diaplectic plagioclase glasses retain their internal crystal structure, such as alignment of inclusions with pre-vitrification twin and cleavage planes (relict plagioclase clouding). Additional evidence of a solid-state transformation from crystal to glass is the possible preservation of twins and preservation of outward crystal boundaries, even in diaplectic

glass clasts in breccias. This evidence supports the findings of previous studies which found a “frozen-in” memory of the original crystal structure (e.g., Arndt et al., 1982; Ostertag and Stöffler, 1982; Stöffler and Hornemann, 1972).

The phenomenon of partial isotropization of mineral grains is a sensitive indicator of the ‘cusp’ pressure immediately preceding the formation of full-grain diaplectic glass. Observations of alternate twin isotropization and zeolitization suggest a potentially extremely sensitive tool for determining orientation of the shock wave relative to individual mineral grains (Stöffler, 1966). These effects do seem to be extremely limited in pressure range, however, as FWHMχ measurements from μXRD indicate that alternate twins do not always show different amounts of strain than each other. Pseudomorphous zeolites may be taken, with caution, as a sign of shock-related vitrification causing an environment conducive to post-shock alteration.

The degree of shock can be inferred from how much of a single crystal has become isotropic (the entire grain, only a small portion, only alternate twins, etc.), and from how much short-range order remains in the amorphous material, as with increasing shock level, the internal structure becomes more and more destroyed until it resembles that of fused glass (Arndt et al., 1982), in which case techniques sensitive to internal structure (e.g., Raman spectroscopy, cathodoluminescence) will also provide insight into how much a diaplectic glass has been shocked.

4.4 Determining whether micro-X-ray diffraction is effective in evaluating shock in feldspars

Measurements of the full-width-at-half-maximum (FWHMχ) of intensity vs. chi plots correlate well with optically observed signs of increasing strain. Certain Miller indices seem to be more consistent, and are therefore the recommended indices for future studies: $(\bar{2}02)$, (004), $(1\bar{5}2)$, and $(53\bar{6})$.

Measurements of strain-related mosaicity of neighbouring twins indicates that twins generally react to passage of the shockwave in a similar fashion, as evidenced by

matching FWHMχ measurements from neighbours. This suggests that the difference in crystal lattice orientation relative to the shockwave (Stöffler, 1966) that allows alternate twins to isotropize, in some cases, while leaving others crystalline occurs over a very narrow range of orientations.

Micro-X-ray diffraction has been shown to be an effective method by which to measure strain-related mosaicity as a proxy for shock level in plagioclase feldspars. As an *in-situ* technique, it has immense value over destructive and semi-destructive techniques, when examining precious planetary materials. It is particularly useful in pressure regimes which create only minimal optical variation in plagioclase (prior to isotropization), but more work needs to be done in order to develop this technique to its maximum potential. It is also important to note that strain-related mosaicity cannot yet be used exclusively to differentiate shock-related strain from endogenic-strain; thus, other techniques must used in conjunction with μXRD in order to establish the cause of the strain observed by streak lengthening in chi.

4.5 Recommendations for Future Work

Further investigation into the nature of planar deformation features in plagioclase needs to involve the investigation of twin and cleavage planes by finer scale techniques, such as transmission electron microscopy, to identify if glass is present along those planes. This would indicate that PDFs form, as in quartz, parallel to rational crystallographic planes but are masked by co-incidence with pre-existing planar features in the feldspars. In order to address the effect(s) that crystal symmetry has on PDF formation, a detailed study of naturally and experimentally shocked feldspars of various compositions and predicted peak pressures should be conducted.

A detailed, multi-technique, study of naturally and experimentally shocked feldspars of a wide variety of compositions and pressure ranges is suggested, in order to address the effect of composition, crystal symmetry, and orientation of the shockwave on determining which shock effects develop in which feldspars. Shock experiments and gathering more samples from a range of craters, with more widely varying compositions, will help to inform not only the formation of PDFs in feldspars, but also the effect of

crystal lattice orientation relative to the shockwave, and under what conditions do only alternate twins show shock effects. It is imperative that chemical composition be reported for studies of shocked feldspars, as shock effects appear to vary significantly with chemical composition and, correspondingly, with crystal structure.

Further developing the quantitative scale of shock in plagioclase that has been started here will require examining the same spots with a different technique, such as Raman spectroscopy, which can also be used to quantify strain, and cross-correlating the results in order to remove the current subjectivity of the optical groups. This might also reveal trends in the measurements that are not currently distinguishable, and may result in clear natural divisions becoming apparent for the lower end of the shock scale (Stöffler's level I).

Reducing the high degree of scatter in FWHMχ measurements on shocked feldspars may be possible through investigating the effects of orientation on detected strain-related mosaicity. Reducing the effects of orientation in future studies could be accomplished by collecting multiple μXRD patterns on each grain, while rotating the grain several degrees between each measurement. This should allow the investigator to find the orientation of highest strain, and to then use that measurement for quantification of shock level. Additionally, investigating mainly those Miller indices containing only low integers should help to constrain the data. In order to increase the statistical reliability of FWHMχ measurements to quantify shock, measuring more grains will undoubtedly help to better define ranges of streak lengths for each optical group. Reducing the effects of orientation will also assist in setting lower boundaries to the groups, in addition to the maxima reported in Chapter 3.

Ideally, FWHMχ measurements should be made of experimentally shocked feldspars of varying compositions, and with known peak pressures, in order to calibrate the FWHMχ scale and develop a truly quantitative method of assessing shock level in feldspars. This would have the additional benefit of elucidating differences in strain between high- and low-Ca plagioclase, and between plagioclase and alkali feldspars.

4.6 References

Arndt J., Hummel W., and Gonzalez-Cabeza I. 1982. Diaplectic labradorite glass from the Manicouagan impact crater; I, Physical properties, crystallization, structural and genetic implications. *Physics and Chemistry of Minerals* 8: 230–239.

Bohor B. F., Betterton W. J., and Krogh T. E. 1993. Impact-shocked zircons: discovery of shock-induced textures reflecting increasing degrees of shock metamorphism. *Earth and Planetary Science Letters* 119: 419–424.

Dressler B. 1990. Shock metamorphic features and their zoning and orientation in the Precambrian rocks of the Manicouagan Structure, Quebec, Canada. *Tectonophysics* 171: 229–245.

Dworak U. 1969. Stoßwellenmetamorphose des Anorthosits vom Manicouagan Krater, Quebec, Canada. *Contributions to Mineralogy and Petrology* 24: 306–347.

Emslie R. F., Cousens B., Hamblin C., and Bielecki J. 1980. The Mistastin Batholith, Labrador-Quebec: An Elsonian Composite Rapakivi Suite. In *Current Research, Part A, Geological Survey of Canada, Paper 80-1 A*. pp. 95–100.

Goltrant O., Leroux H., Doukhan J.-C., and Cordier P. 1992. Formation mechanisms of planar deformation features in naturally shocked quartz. *Physics of the Earth and Planetary Interiors* 74: 219–240.

Nesse W. D. 2004. *Introduction to Optical Mineralogy*, 3rd ed. New York: Oxford University Press. 348 p.

Ostertag R. 1983. Shock experiments on feldspar crystals. *Journal of Geophysical Research* 88, Suppl.: B364–B376.

Ostertag R., and Stöffler D. 1982. Thermal annealing of experimentally shocked feldspar crystals. *Proceedings of the 13th Lunar and Planetary Science Conference, Part 1 - Journal of Geophysical Research* 87: A457–A463.

Stöffler D. 1972. Deformation and transformation of rock-forming minerals by natural and experimental shock processes: I. Behavior of minerals under shock compression. *Fortschritte der Mineralogie* 49: 50–113.

Stöffler D. 1974. Deformation and transformation of rock-forming minerals by natural and experimental shock processes: II. Physical properties of shocked minerals. *Fortschritte der Mineralogie* 51: 256–289.

Stöffler D. 1971. Progressive metamorphism and classification of shocked and brecciated crystalline rocks at impact craters. *Journal of Geophysical Research* 76: 5541–5551.

Stöffler D. 1966. Zones of impact metamorphism in the crystalline rocks of the Nördlinger Ries crater. *Contributions to Mineralogy and Petrology* 12: 15–24.

Stöffler D., and Hornemann U. 1972. Quartz and feldspar glasses produced by natural and experimental shock. *Meteoritics* 7: 371–394.

Stöffler D., Keil K., and Scott E. R. D. 1991. Shock metamorphism of ordinary chondrites. *Geochimica et Cosmochimica Acta* 55: 3845–3867.

Taylor F. C., and Dence M. R. 1969. A probable meteorite origin for Mistastin Lake, Labrador. *Canadian Journal of Earth Sciences* 6: 39–45.

Appendices

Appendix A: Complete Mistastin sample list, including collection location

Table A-1: Mistastin Lake sample list

Sample Name	Lithology	Location	Coordinates	
			x	Y
MHI10-04	Anorthosite	Horseshoe Island	478733	6193942
MHI10-12	Anorthosite	Horseshoe Island	479337	6191772
MHI10-17	Anorthosite	Horseshoe Island	479337	6191772
MHI10-22	Mangerite	Horseshoe Island	478805	6192664
MHI10-23	Mangerite	Horseshoe Island	479170	6192991
MHI10-35	Mangerite	Horseshoe Island	477907	6192617
MHI10-51	Anorthosite	Horseshoe Island	479709	6194099
MHI10-54	Anorthosite	Horseshoe Island	480510	6192273
MM09-10	Breccia	Steep Creek	482163	6200564
MM09-32-B	Granodiorite	Steep Creek	482331	6200798
MM09-35-A	Anorthosite	Coté Creek	475465	6197103
MM09-35-D	Anorthosite	Coté Creek	475465	6197103
MM09-35-E	Anorthosite	Coté Creek 1	475465	6197103
MM10-13-1	Anorthosite clast breccia	Coté Creek	475464	6197101
MM10-01-C	Breccia	Discovery Hill	472834	6190592
MM10-05-B-1	Polymict Breccia	Coté Creek 2	475332	6197385
MM10-05-B-2	Polymict Breccia	Coté Creek 2	475332	6197385
MM10-05-C	Clast rich melt	Coté Creek 2	475332	6197385
MM10-06-A-2	Polymict Breccia	Coté Creek 2	475332	6197385
MM10-06-A-3	Polymict Breccia	Coté Creek 2	475332	6197385
MM10-06-D-2	Mng/Grd	Coté Creek 2	475332	6197385
MM10-09-B	Clast rich melt	Coté Creek	475332	6197385
MM10-10	Clast rich melt	Coté Creek 2	475332	6197385
MM10-11	Anorthosite breccia	Coté Creek 1	475464	6197101
MM10-12-2	Polymict breccia	Coté Creek 1	475464	6197101
MM10-13-1	Polymict breccia	Coté Creek 1	475464	6197101
MM10-13-2	Polymict Breccia	Coté Creek 1	475464	6197101
MM10-16	Shocked anorthosite	Coté Creek 1	475450	6197112
MM10-17-A	Mng/Grd breccia	Coté Creek	474955	6197571
MM10-17-B	Mng/Grd breccia	Coté Creek	474955	6197571
MM10-20	Polymict Breccia	Piccadilly Creek	475624	6198198
MM10-20-1	Polymict breccia	Piccadilly Creek	475624	6198198
MM10-20-2	Polymict breccia	Piccadilly Creek	475624	6198198
MM10-24	Polymict Breccia	Piccadilly Creek	475624	6198198
MM10-25	Anorthosite breccia	Piccadilly Creek	475624	6198198
MM10-28	Anorthosite breccia	Piccadilly Creek	475624	6198198
MM10-30	Anorthosite breccia	Piccadilly Creek	475624	6198198

(Table A-1 continued)

Sample Name	Lithology	Location	Coordinates	
			x	Y
MM10-32	Breccia	Piccadilly Creek	475624	6198198
MM10-32-A	Granodiorite	River Island		
MM10-32-B	Mangerite	River Island		
MM10-33	Granodiorite	River Mouth		
MM10-34-A	Polymict breccia	Coté Creek	490098	6199261
MM10-34-C-2	Polymict breccia	Coté Creek	490098	6199261
MM10-34-C-5	Polymict breccia	Coté Creek	490098	6199261
MM10-35-D	Anorthosite Breccia	South Creek		
MM10-36-B-1	Polymict breccia	South Creek		
MM10-36-B-2	Polymict breccia	South Creek		
MM10-38	Anorthosite breccia	South Creek		
MM10-39	Anorthosite breccia	South Creek		
MM10-40	Anorthosite breccia	South Creek		
MM10-41-1	Polymict breccia	South Creek		
MM10-42	Anorthosite breccia	South Creek		
MM10-43	Anorthosite breccia	South Creek		
MM10-44	Anorthosite breccia	South Creek		
MM10-45	Polymict breccia	South Creek		
MM10-46-2	Polymict breccia	South Creek		
MM10-47	Mangerite	Rim's End		
MM10-48	Mangerite/Granodiorite	Rim's End		
MM10-54-2	Anorthosite	Horseshoe Island		
MST09-020	Anorthosite	Horseshoe Island	479613	6193701
MST09-022	Anorthosite	Horseshoe Island	480913	6192613
MST09-024	Anorthosite	Horseshoe Island	481421	6192261
MST09-025	Anorthosite	Horseshoe Island	481025	6192271
MST09-026	Anorthosite	Horseshoe Island		

Appendix B: Microprobe analyses of Mistastin samples

Quantitative chemical analyses of feldspar grains, diaplectic glasses, and mineral inclusions in plagioclase, from the Mistastin Lake impact structure were carried out on a JXA-8530F Field Emission Electron Probe Microanalyzer (FE-EPMA) in the Earth and Planetary Materials Analysis Laboratory at the University of Western Ontario.

Table B-1: Beam operating conditions and calibration standards for microprobe analyses

Session	**1**	**2**	**3**
Accelerating voltage	10 kV	15 kV	10kV
Probe current	20 nA	20 nA	10 nA
Beam diameter	5 µm	<1 µm	<1 µm

Element	**Standard**	**Standard**	**Standard**
Na	Albite (CM Taylor)	Albite (CM Taylor)	Albite (CM Taylor)
Si	Orthoclase (CM Taylor)	Albite (CM Taylor)	Albite (CM Taylor)
Al	Anorthite (Smithsonian USNM 137041 - Great Sitkin Island, AL)	Anorthite (Smithsonian USNM 137041 - Great Sitkin Island, AL)	Anorthite (Smithsonian USNM 137041 - Great Sitkin Island, AL)
K	Orthoclase (CM Taylor)	Orthoclase (CM Taylor)	Orthoclase (CM Taylor)
Ca	Anorthite (Smithsonian USNM 137041 - Great Sitkin Island, AL)	Anorthite (Smithsonian USNM 137041 - Great Sitkin Island, AL)	Anorthite (Smithsonian USNM 137041 - Great Sitkin Island, AL)
Fe	N/A	Hornblende (Smithsonian USNM 143965 - Kakanui, New Zealand)	Haematite (Harvard 92649)
Ti	N/A	Hornblende (Smithsonian USNM 143965 - Kakanui, New Zealand)	Ilmenite (Smithsonian USNM 96189 - Ilmen Mnts., USSR)
Mg	N/A	N/A	Chromite (Smithsonian USNM 117075 - Tiebaghi Mine, New Caledonia)

Table B-2: Microprobe analyses of feldspars

Abbreviations: wt% = mean composition in weight%; N/A = Not Analyzed; S= Session number; G=Grain number; I.D.=Mineral (An=Anorthite, Lb=Labradorite, K=Potassium feldspar)

S	Sample Name	G	I.D.	SiO_2 (wt%)	Na_2O (wt%)	Al_2O_3 (wt%)	K_2O (wt%)	CaO (wt%)	FeO (wt%)	Total (wt%)
2	MM10-011	1	An	58.11	6.10	27.28	0.49	8.78	0.22	101.17
2	MM10-011	1	An	56.82	5.81	27.48	0.48	9.07	0.19	100.10
2	MM10-011	1	An	57.10	6.04	27.45	0.47	8.98	0.20	100.41
2	MM10-011	1	An	58.12	6.08	27.32	0.39	8.76	0.15	100.92
2	MM10-011	1	An	57.01	5.93	27.66	0.42	9.16	0.22	100.43
2	MM10-011	2	An	57.84	6.29	26.62	0.45	8.12	0.36	99.85
2	MM10-011	2	An	57.78	6.45	26.42	0.40	8.31	0.22	99.73
2	MM10-011	2	An	56.63	6.01	26.56	0.39	8.71	0.29	98.71
2	MM10-011	2	An	57.77	6.07	26.41	0.49	8.36	0.20	99.47
2	MM10-011	2	An	62.93	0.73	19.26	15.12	-1.02	0.12	99.60
2	MM10-011	3	An	55.79	5.50	27.71	0.85	8.49	0.23	98.74
2	MM10-011	3	An	55.73	5.65	27.78	0.45	9.77	0.20	99.72
2	MM10-011	3	An	55.65	5.55	28.07	0.41	9.99	0.22	100.05
2	MM10-011	3	An	56.44	5.63	27.69	0.50	9.43	0.23	100.16
2	MM10-011	3	An	55.99	5.43	28.05	0.46	9.78	0.24	100.19
2	MM10-011	4	An	53.63	5.04	28.16	0.39	8.96	0.25	96.79
2	MM10-011	4	An	56.33	5.48	27.94	0.43	9.68	0.20	100.19
2	MM10-011	4	An	55.95	5.32	28.23	0.44	9.85	0.23	100.29
2	MM10-011	4	An	56.51	5.59	27.35	0.46	9.11	0.20	99.48
2	MM10-011	4	An	55.96	5.36	28.08	0.47	9.97	0.25	100.26
2	MM10-011	5	An	57.43	5.94	27.12	0.46	8.74	0.20	100.03
2	MM10-011	5	An	57.37	5.98	27.07	0.52	8.79	0.19	100.18
2	MM10-011	5	An	57.27	5.94	27.14	0.44	8.76	0.26	100.01
2	MM10-011	5	An	56.06	5.51	27.88	0.40	9.87	0.24	100.18
2	MM10-011	5	An	58.23	6.40	26.77	0.50	8.21	0.21	100.55
2	MM10-048	2	An	60.51	7.65	25.31	0.36	6.28	0.07	100.27
2	MM10-048	2	An	60.70	7.61	24.98	0.33	6.20	0.10	100.05
2	MM10-048	2	An	60.85	7.74	25.37	0.28	6.28	0.12	100.76
2	MM10-048	2	An	60.85	7.74	24.94	0.33	5.79	0.14	99.82
2	MM10-048	2	An	61.29	7.83	25.15	0.31	6.01	0.13	100.78
2	MM10-048	3	K	65.51	2.24	19.42	13.41	-0.84	0.03	100.53
2	MM10-048	3	K	65.43	1.42	19.69	13.95	-0.87	0.04	100.41
2	MM10-048	3	K	64.62	0.94	19.24	15.36	-1.05	0.01	100.11
2	MM10-048	3	K	67.88	10.78	21.63	0.04	0.80	0.02	101.22
2	MM10-048	3	K	65.76	9.86	23.06	1.01	0.72	0.10	100.56
2	MM10-048	5	K	64.58	1.72	19.28	13.92	-0.79	0.04	99.35
2	MM10-048	5	K	65.09	3.13	19.45	11.97	-0.50	0.03	99.70
2	MM10-048	5	K	66.79	3.91	20.02	9.26	-0.15	0.09	100.39

(Table B-2 continued)

S	Sample Name	G	I.D.	SiO_2 (wt%)	Na_2O (wt%)	Al_2O_3 (wt%)	K_2O (wt%)	CaO (wt%)	FeO (wt%)	Total (wt%)
2	MM10-048	5	K	64.91	1.45	19.47	14.48	-0.93	0.01	100.13
2	MM10-048	5	K	66.81	4.38	20.25	9.74	-0.42	0.05	101.55
2	MM10-048	6	K	66.61	4.17	20.33	9.05	-0.43	0.01	100.37
2	MM10-048	6	K	64.83	1.56	19.27	14.75	-0.98	-0.04	100.11
2	MM10-048	6	K	65.24	0.84	18.99	15.69	-1.08	0.06	100.34
2	MM10-048	6	K	64.57	0.85	19.02	15.48	-1.00	0.01	99.79
2	MM10-048	6	K	64.55	1.11	19.51	14.86	-0.96	0.02	99.96
2	MM10-048	7	An	61.13	7.86	25.36	0.32	6.15	0.13	101.02
2	MM10-048	7	An	61.10	7.83	25.25	0.36	6.10	0.10	100.79
2	MM10-048	7	An	60.33	7.70	25.20	0.36	6.12	0.12	99.80
2	MM10-048	7	An	61.14	7.73	24.97	0.37	5.97	0.09	100.37
2	MM10-048	7	An	60.47	7.76	24.98	0.34	5.90	0.17	99.63
2	MM10-048	8	An	61.07	7.76	25.25	0.36	6.10	0.15	100.75
2	MM10-048	8	An	60.86	7.70	25.24	0.31	6.26	0.11	100.50
2	MM10-048	8	An	61.30	7.86	24.99	0.33	5.90	0.17	100.57
2	MM10-048	8	An	60.85	7.69	25.45	0.37	6.39	0.12	100.94
2	MM10-048	8	An	60.94	7.80	25.17	0.37	6.17	0.14	100.65
2	MM10-032B	1	K	65.04	1.50	19.32	14.10	-0.92	0.02	100.09
2	MM10-032B	1	K	65.13	1.71	19.34	13.96	-0.94	0.02	100.39
2	MM10-032B	1	K	64.80	2.32	19.81	12.81	-0.77	0.04	100.46
2	MM10-032B	1	K	64.65	0.87	19.07	15.24	-1.06	-0.01	100.14
2	MM10-032B	1	K	65.88	4.74	20.36	8.51	-0.13	0.04	100.29
2	MM10-032B	2	An	60.70	7.80	25.45	0.21	6.32	0.08	100.68
2	MM10-032B	2	An	60.83	7.68	25.38	0.23	6.39	0.05	100.65
2	MM10-032B	2	An	60.71	7.39	26.03	0.29	6.41	0.06	101.00
2	MM10-032B	2	An	61.80	8.27	24.47	0.16	5.40	0.09	100.25
2	MM10-032B	2	An	60.64	7.83	25.53	0.19	6.35	0.12	100.76
2	MM10-032B	3	K	64.46	0.85	19.13	15.30	-1.08	0.08	100.06
2	MM10-032B	3	K	64.48	0.88	19.38	15.31	-1.06	-0.02	100.36
2	MM10-032B	3	K	65.34	1.94	19.42	13.66	-0.88	0.04	100.60
2	MM10-040	1	An	56.87	5.61	28.32	0.00	9.66	0.23	100.91
2	MM10-040	1	An	56.10	5.51	28.49	0.36	10.16	0.22	100.95
2	MM10-040	1	An	56.36	5.61	28.04	0.42	9.67	0.25	100.46
2	MM10-040	1	An	56.14	5.33	28.27	0.41	10.08	0.27	100.70
2	MM10-040	1	An	57.12	5.74	27.88	0.41	9.33	0.39	101.23
2	MM10-040	2	An	56.44	5.70	27.83	0.37	9.39	0.24	100.16
2	MM10-040	2	An	57.14	5.72	27.96	0.43	9.59	0.18	101.11
2	MM10-040	2	An	56.90	5.66	28.05	0.35	9.51	0.28	100.88
2	MM10-040	2	An	56.35	5.53	28.27	0.41	9.85	0.21	100.74
2	MM10-040	2	An	56.62	5.62	28.43	0.35	9.95	0.24	101.47
2	MM10-040	3	An	57.26	5.86	27.64	0.46	9.20	0.21	100.82
2	MM10-040	3	An	56.59	5.72	28.05	0.40	9.56	0.25	100.75
2	MM10-040	3	An	56.58	5.63	28.24	0.36	9.79	0.24	100.99

(Table B-2 continued)

S	Sample Name	G	I.D.	SiO_2 (wt%)	Na_2O (wt%)	Al_2O_3 (wt%)	K_2O (wt%)	CaO (wt%)	FeO (wt%)	Total (wt%)
2	MM10-040	3	An	56.55	5.76	28.27	0.38	9.73	0.21	101.09
2	MM10-040	3	An	56.68	5.78	28.06	0.40	9.47	0.27	100.81
2	MM10-040	4	An	56.40	5.49	28.41	0.36	9.67	0.26	100.74
2	MM10-040	4	An	56.06	5.48	28.49	0.36	9.93	0.21	100.69
2	MM10-040	4	An	55.84	5.23	28.71	0.34	10.13	0.19	100.57
2	MM10-040	4	An	56.03	5.42	28.63	0.39	10.19	0.20	101.08
2	MM10-040	4	An	56.48	5.51	27.99	0.34	9.85	0.20	100.55
2	MM10-040	5	An	55.55	5.19	28.60	0.34	10.56	0.26	100.63
2	MM10-040	5	An	55.54	5.25	28.85	0.35	10.59	0.33	101.04
2	MM10-040	5	An	55.45	5.16	28.74	0.43	10.55	0.26	100.76
2	MM10-040	5	An	56.65	5.73	28.15	0.38	9.61	0.20	100.81
2	MM10-040	5	An	56.29	5.52	28.12	0.42	9.80	0.24	100.47
2	MM10-040	6	An	56.71	5.55	27.95	0.39	9.76	0.24	100.71
2	MM10-040	6	An	56.28	5.46	28.05	0.38	9.71	0.31	100.34
2	MM10-040	6	An	56.39	5.37	28.21	0.38	9.90	0.21	100.65
2	MM10-040	6	An	56.14	5.51	28.26	0.40	10.13	0.29	100.79
2	MM10-040	6	An	56.59	5.69	28.13	0.43	9.93	0.28	101.23
2	MM10-040	7	An	56.20	5.21	28.47	0.35	9.99	0.28	100.63
2	MM10-040	7	An	56.49	5.44	28.34	0.38	10.03	0.31	101.19
2	MM10-040	7	An	56.08	5.29	28.29	0.37	10.27	0.32	100.83
2	MM10-040	7	An	55.67	5.25	28.67	0.31	10.52	0.25	100.90
2	MM10-040	7	An	55.74	5.36	28.58	0.35	10.24	0.26	100.74
2	MM10-040	8	An	55.59	5.35	28.52	0.36	10.46	0.28	100.80
2	MM10-040	8	An	55.89	5.46	28.87	0.29	10.64	0.27	101.52
2	MM10-040	8	An	55.26	5.04	29.00	0.34	10.78	0.32	100.91
2	MM10-040	8	An	55.67	5.22	28.71	0.33	10.49	0.24	100.76
2	MM10-040	8	An	55.79	5.27	28.76	0.33	10.68	0.25	101.23
2	MM10-040	9	An	55.78	5.38	28.36	0.40	10.14	0.25	100.45
2	MM10-040	9	An	56.91	5.73	28.11	0.39	9.84	0.27	101.35
2	MM10-040	9	An	58.08	5.72	29.41	0.39	10.13	0.29	104.23
2	MM10-040	9	An	55.60	5.19	28.61	0.38	10.46	0.19	100.53
2	MM10-040	9	An	56.19	5.47	28.46	0.45	10.18	0.22	101.10
1	MHI10_17	1	Lb	53.36	5.14	28.47	0.38	10.62	N/A	97.96
1	MHI10_17	1	Lb	53.89	5.03	28.48	0.39	10.82	N/A	98.60
1	MHI10_17	1	Lb	54.07	5.15	28.40	0.37	10.71	N/A	98.71
1	MHI10_17	1	Lb	54.56	5.32	28.05	0.42	10.32	N/A	98.67
1	MHI10_17	2	Lb	54.34	5.43	28.05	0.42	10.17	N/A	98.41
1	MHI10_17	2	Lb	54.12	5.42	28.10	0.40	10.10	N/A	98.14
1	MHI10_17	2	Lb	54.63	5.37	28.04	0.39	10.10	N/A	98.53
1	MHI10_17	2	Lb	54.92	5.47	27.94	0.39	9.97	N/A	98.68
1	MHI10_17	3	Lb	55.48	5.52	27.64	0.42	9.61	N/A	98.66
1	MHI10_17	3	Lb	55.26	5.51	27.28	0.42	9.54	N/A	98.01
1	MHI10_17	3	Lb	55.29	5.63	27.47	0.36	9.55	N/A	98.31

(Table B-2 continued)

S	Sample Name	G	I.D.	SiO_2 (wt%)	Na_2O (wt%)	Al_2O_3 (wt%)	K_2O (wt%)	CaO (wt%)	FeO (wt%)	Total (wt%)
1	MHI10_17	3	Lb	54.93	5.46	27.37	0.42	9.77	N/A	97.94
1	MHI10_17	4	Lb	55.18	5.51	27.51	0.37	9.55	N/A	98.12
1	MHI10_17	4	Lb	55.28	5.51	27.04	0.41	9.47	N/A	97.71
1	MHI10_17	4	Lb	54.74	5.64	27.49	0.40	9.52	N/A	97.79
1	MHI10_17	4	Lb	54.96	5.46	27.53	0.35	9.62	N/A	97.91
1	MHI10_17	5	Lb	54.12	5.34	27.79	0.42	10.32	N/A	97.99
1	MHI10_17	5	Lb	54.33	5.31	27.85	0.43	10.40	N/A	98.31
1	MHI10_17	5	Lb	54.04	5.36	27.79	0.41	10.04	N/A	97.64
1	MHI10_17	5	Lb	54.23	5.27	28.06	0.44	10.33	N/A	98.32

Table B-3: Microprobe analyses of diaplectic feldspar glasses

Abbreviations: wt% = mean composition in weight%; N/A = Not Analyzed; S= Session number; G=Grain number; I.D.=Mineral precursor (An=Anorthite, Lb=Labradorite)

S	Sample Name	G	I.D.	SiO_2 (wt%)	Na_2O (wt%)	Al_2O_3 (wt%)	K_2O (wt%)	CaO (wt%)	FeO (wt%)	Total (wt%)
2	MM10-34C-5	1		46.81	2.84	24.75	0.33	7.18	0.13	82.14
2	MM10-34C-5	1		46.46	2.14	24.98	0.34	7.73	0.11	81.86
2	MM10-34C-5	1		46.24	2.66	25.27	0.31	7.67	0.13	82.40
2	MM10-34C-5	1		46.08	3.74	24.76	0.32	7.50	0.10	82.58
2	MM10-34C-5	1		46.81	2.33	25.00	0.31	7.55	0.12	82.23
2	MM10-34C-5	2		45.42	5.48	23.51	0.20	7.35	0.11	82.17
2	MM10-34C-5	2		45.88	5.52	23.66	0.20	7.23	0.12	82.77
2	MM10-34C-5	2		46.42	5.56	23.97	0.20	7.29	0.09	83.59
2	MM10-34C-5	2		48.13	5.17	24.43	0.20	7.32	0.14	85.50
2	MM10-34C-5	2		47.96	5.53	24.48	0.21	7.41	0.10	85.83
2	MM10-34C-5	3		42.27	3.09	12.99	0.78	5.32	0.10	64.66
2	MM10-34C-5	3		41.89	2.84	12.46	0.92	5.32	0.07	63.58
2	MM10-34C-5	3		48.80	2.59	22.71	1.85	5.52	0.13	81.72
2	MM10-34C-5	3		48.48	3.89	22.95	0.50	5.50	0.12	81.60
2	MM10-34C-5	3		48.29	3.76	22.71	0.88	5.35	0.08	81.26
2	MM10-038	1	An	55.22	3.47	23.85	0.54	8.60	0.23	92.07
2	MM10-038	1	An	57.80	2.19	27.69	0.53	8.84	0.26	97.52
2	MM10-038	1	An	57.03	3.60	27.84	0.50	9.03	0.28	98.52
2	MM10-038	1	An	56.50	3.60	28.07	0.49	9.46	0.17	98.44
2	MM10-038	1	An	56.42	3.56	28.08	0.50	9.44	0.24	98.39
2	MM10-038	2	An	57.64	2.43	27.56	0.50	9.65	0.27	98.20
2	MM10-038	2	An	56.74	3.56	27.72	0.57	9.22	0.23	98.11
2	MM10-038	2	An	56.46	3.51	27.82	0.54	9.10	0.21	97.83
2	MM10-038	2	An	56.78	3.56	28.08	0.47	9.08	0.20	98.30

(Table B-3 continued)

S	Sample Name	G	I.D.	SiO_2 (wt%)	Na_2O (wt%)	Al_2O_3 (wt%)	K_2O (wt%)	CaO (wt%)	FeO (wt%)	Total (wt%)
2	MM10-038	2	An	57.50	2.21	28.14	0.55	8.75	0.20	97.52
2	MM10-038	3	An	55.04	3.38	28.91	0.45	10.33	0.25	98.50
2	MM10-038	3	An	55.22	3.34	28.89	0.42	10.53	0.26	98.78
2	MM10-038	3	An	55.04	3.18	28.84	0.44	10.29	0.25	98.24
2	MM10-038	3	An	55.20	2.44	29.19	0.43	10.31	0.25	97.94
2	MM10-038	3	An	54.95	3.20	29.00	0.40	10.59	0.25	98.57
2	MM10-038	4	An	56.79	3.56	27.97	0.48	8.93	0.21	98.12
2	MM10-038	4	An	56.57	3.51	27.75	0.48	9.17	0.19	97.86
2	MM10-038	4	An	57.43	2.14	27.92	0.49	8.86	0.21	97.18
2	MM10-038	4	An	57.00	3.37	27.96	0.50	8.85	0.22	98.02
2	MM10-038	4	An	56.51	3.36	27.95	0.50	9.29	0.19	97.92
2	MM10-038	5	An	55.76	3.30	28.24	0.52	10.12	0.12	98.29
2	MM10-038	5	An	56.48	2.49	28.46	0.45	9.63	0.16	97.78
2	MM10-038	5	An	55.69	3.44	28.36	0.48	9.88	0.18	98.12
2	MM10-038	5	An	55.44	3.43	28.37	0.48	9.95	0.46	98.48
2	MM10-038	5	An	55.61	3.41	28.44	0.50	10.03	0.19	98.26
2	MM10-038	6	An	56.32	2.31	28.58	0.50	9.77	0.18	97.77
2	MM10-038	6	An	55.77	3.36	28.52	0.44	9.82	0.22	98.25
2	MM10-038	6	An	55.73	3.33	28.65	0.45	9.89	0.21	98.40
2	MM10-038	6	An	55.42	3.19	28.65	0.45	9.82	0.22	97.91
2	MM10-038	6	An	56.21	2.41	28.93	0.45	9.81	0.26	98.19
2	MM10-038	7	An	55.31	3.35	28.67	0.43	9.96	0.24	98.11
2	MM10-038	7	An	54.98	3.33	28.36	0.46	10.56	0.19	98.01
2	MM10-038	7	An	55.34	3.15	28.60	0.43	10.20	0.27	98.13
2	MM10-038	7	An	56.13	2.36	28.85	0.45	9.82	0.24	98.04
2	MM10-038	7	An	55.20	3.36	28.70	0.50	9.98	0.23	98.10
2	MM10-038	8	An	56.42	3.40	27.89	0.50	9.10	0.29	97.73
2	MM10-038	8	An	56.50	3.42	28.20	0.48	9.39	0.26	98.42
2	MM10-038	8	An	57.15	2.39	28.01	0.50	9.14	0.21	97.61
2	MM10-038	8	An	56.66	3.41	27.86	0.48	9.26	0.30	98.14
2	MM10-038	8	An	56.71	3.42	27.99	0.52	8.97	0.19	97.92
2	MM09-035D	1	An	37.17	3.33	19.65	0.31	5.73	0.14	66.47
2	MM09-035D	1	An	42.11	2.24	22.37	0.32	5.78	0.11	73.05
2	MM09-035D	1	An	39.32	3.69	21.39	0.28	5.21	0.09	70.08
2	MM09-035D	1	An	38.39	3.80	21.24	0.37	5.27	0.09	69.20
2	MM09-035D	1	An	39.68	3.67	22.14	0.38	5.80	0.06	71.82
2	MM09-035D	2	An	55.71	2.64	28.84	0.48	9.48	0.30	97.56
2	MM09-035D	2	An	54.36	3.58	28.49	0.48	9.45	0.20	96.71
2	MM09-035D	2	An	54.13	3.59	28.42	0.54	9.51	0.30	96.65
2	MM09-035D	2	An	54.09	3.66	28.34	0.55	9.55	0.23	96.56
2	MM09-035D	2	An	55.24	2.53	28.31	0.55	9.29	0.27	96.36
2	MM09-035D	3	An	55.37	3.45	27.78	0.76	9.02	0.29	96.82
2	MM09-035D	3	An	55.65	3.52	27.76	0.75	9.00	0.31	97.10

(Table B-3 continued)

S	Sample Name	G	I.D.	SiO_2 (wt%)	Na_2O (wt%)	Al_2O_3 (wt%)	K_2O (wt%)	CaO (wt%)	FeO (wt%)	Total (wt%)
2	MM09-035D	3	An	55.90	3.54	27.91	0.77	9.03	0.29	97.65
2	MM09-035D	3	An	56.20	2.21	27.80	0.76	8.93	0.34	96.38
2	MM09-035D	3	An	55.51	3.62	27.89	0.77	9.09	0.33	97.35
2	MM09-035D	4	An	55.09	3.41	28.59	0.56	10.11	0.24	98.20
2	MM09-035D	4	An	54.41	3.34	28.48	0.57	10.00	0.21	97.17
2	MM09-035D	4	An	55.04	2.50	28.99	0.63	10.08	0.24	97.65
2	MM09-035D	4	An	55.08	3.39	28.69	0.64	10.08	0.25	98.28
2	MM09-035D	4	An	54.75	3.39	29.03	0.56	10.31	0.28	98.47
2	MM09-035D	5	An	53.66	3.55	27.49	0.54	8.99	0.25	94.67
2	MM09-035D	5	An	54.39	2.67	28.01	0.57	9.21	0.19	95.18
2	MM09-035D	5	An	54.56	3.49	27.38	0.61	8.54	0.17	94.92
2	MM09-035D	5	An	53.94	3.56	27.93	0.60	8.94	0.20	95.29
2	MM09-035D	5	An	53.90	3.54	27.76	0.59	9.04	0.22	95.24
2	MM10-13-2	1	Lb	55.88	2.41	29.78	0.37	10.79	0.20	99.59
2	MM10-13-2	1	Lb	55.04	3.37	29.82	0.36	10.61	0.21	99.60
2	MM10-13-2	1	Lb	54.89	3.36	29.71	0.35	10.92	0.18	99.55
2	MM10-13-2	1	Lb	55.05	3.45	29.47	0.34	10.84	0.21	99.55
2	MM10-13-2	1	Lb	55.55	2.36	29.68	0.37	10.60	0.19	98.91
2	MM10-13-2	2	Lb	56.26	3.46	28.58	0.47	9.93	0.20	99.07
2	MM10-13-2	2	Lb	55.60	3.35	27.92	0.50	9.37	0.43	97.61
2	MM10-13-2	2	Lb	56.44	3.52	28.71	0.48	9.77	0.22	99.29
2	MM10-13-2	2	Lb	56.88	2.40	28.79	0.44	9.79	0.24	98.72
2	MM10-13-2	2	Lb	56.60	3.47	28.74	0.46	9.70	0.18	99.32
2	MM10-13-2	3	Lb	55.88	3.36	29.12	0.41	10.33	0.33	99.59
2	MM10-13-2	3	Lb	55.70	3.36	28.97	0.41	10.24	0.21	99.06
2	MM10-13-2	3	Lb	56.81	2.36	29.15	0.41	10.08	0.23	99.20
2	MM10-13-2	3	Lb	56.02	3.45	29.08	0.40	10.42	0.29	99.79
2	MM10-13-2	3	Lb	55.86	3.42	29.14	0.41	10.64	0.24	99.83
2	MM10-13-2	4	Lb	56.38	3.54	29.05	0.39	10.13	0.15	99.80
2	MM10-13-2	4	Lb	57.33	2.29	29.02	0.39	9.55	0.17	98.88
2	MM10-13-2	4	Lb	55.89	3.52	29.20	0.37	10.40	0.14	99.56
2	MM10-13-2	4	Lb	56.15	3.44	29.03	0.38	10.32	0.21	99.64
2	MM10-13-2	4	Lb	56.47	3.37	28.90	0.40	9.81	0.24	99.28
2	MM10-13-2	5	Lb	55.32	2.39	29.84	0.47	10.84	0.14	99.15
2	MM10-13-2	5	Lb	54.68	3.46	29.55	0.45	10.98	0.13	99.37
2	MM10-13-2	5	Lb	55.40	3.40	29.56	0.45	10.77	0.15	99.82
2	MM10-13-2	5	Lb	55.06	3.42	29.43	0.46	10.90	0.19	99.57
2	MM10-13-2	5	Lb	55.68	2.38	29.66	0.48	10.56	0.14	98.99
2	MM10-13-2	6	Lb	55.99	3.46	29.15	0.39	10.11	0.15	99.37
2	MM10-13-2	6	Lb	55.35	3.39	29.10	0.37	10.35	0.11	98.72
2	MM10-13-2	6	Lb	55.47	3.33	29.25	0.36	10.48	0.13	99.10
2	MM10-13-2	6	Lb	56.60	2.41	29.30	0.37	10.05	0.20	99.04
2	MM10-13-2	6	Lb	56.72	3.67	28.57	0.39	9.97	0.14	99.59

(Table B-3 continued)

S	Sample Name	G	I.D.	SiO_2 (wt%)	Na_2O (wt%)	Al_2O_3 (wt%)	K_2O (wt%)	CaO (wt%)	FeO (wt%)	Total (wt%)
2	MM10-13-2	7	Lb	55.48	3.48	29.23	0.41	10.55	0.12	99.43
2	MM10-13-2	7	Lb	55.63	3.46	29.24	0.39	10.53	0.12	99.46
2	MM10-13-2	7	Lb	56.65	2.36	29.30	0.41	10.26	0.15	99.30
2	MM10-13-2	7	Lb	55.95	3.32	29.04	0.36	10.26	0.15	99.21
2	MM10-13-2	7	Lb	55.33	3.20	29.36	0.37	10.58	0.16	99.16
2	MM10-13-2	8	Lb	56.09	3.37	28.86	0.41	10.28	0.16	99.32
2	MM10-13-2	8	Lb	57.09	2.44	29.17	0.41	9.82	0.21	99.33
2	MM10-13-2	8	Lb	55.98	3.47	29.05	0.41	10.31	0.16	99.57
2	MM10-13-2	8	Lb	56.24	3.36	29.18	0.40	10.02	0.16	99.54
2	MM10-13-2	8	Lb	56.08	3.47	29.10	0.40	10.06	0.16	99.47

Table B-4: Microprobe analyses of Fe-oxide microlite inclusions in feldspar and diaplectic glass grains

Inclusions are less than 2 μm thick, and as a result some analyses incorporate elements from the surrounding feldspar. Abbreviations: wt% = mean composition in weight%; S= Session number; G=Grain number.

S	Sample Name	G	SiO_2 (wt%)	Na_2O (wt%)	Al_2O_3 (wt%)	CaO (wt%)	Fe_2O_3 (wt%)	MgO (wt%)	Cr_2O_3 (wt%)	TiO_2 (wt%)	Total (wt%)
1	MM10-040	1	0.24	0.04	0.56	0.32	99.40	0.02	0.04	0.31	100.95
1	MM10-040	2	0.16	0.01	0.33	0.23	103.15	-0.01	0.01	0.00	103.89
1	MM10-040	3	0.20	0.04	0.33	0.28	99.28	0.03	-0.01	7.12	107.30
1	MM10-040	4	3.69	0.22	4.02	0.64	100.93	-0.01	-0.03	0.06	109.55
1	MM10-040	5	26.70	1.24	9.58	1.16	55.92	0.75	0.04	14.69	110.11
1	MM10-040	6	22.44	0.20	1.38	1.28	52.78	3.75	-0.01	19.41	101.24
1	MM10-038	1	0.19	-0.03	0.43	0.32	98.95	0.08	0.06	0.28	100.27
1	MM10-038	2	2.30	0.09	2.25	0.46	97.25	0.11	-0.05	2.01	104.46
1	MM10-038	3	0.24	0.01	1.11	0.37	100.21	0.03	0.13	2.45	104.57
1	MM10-038	4	0.16	0.04	0.43	0.28	98.86	0.08	0.16	0.04	100.06
1	MM10-038	5	0.15	0.01	0.44	0.30	98.18	0.04	-0.02	0.04	99.15

Table B-5: Microprobe analyses of the zeolite phase levyne-Ca

Abbreviations: wt% = mean composition in weight%; S= Session number; G=Grain number; I.D.=Mineral

S	Sample Name	G	I.D.	SiO_2 (wt%)	Na_2O (wt%)	Al_2O_3 (wt%)	K_2O (wt%)	CaO (wt%)	Total (wt%)
1	MHI10_17	1	Levyne-Ca	46.17	0.25	21.74	0.53	10.93	79.62
1	MHI10_17	1	Levyne-Ca	47.23	0.19	22.66	0.54	11.01	81.63
1	MHI10_17	1	Levyne-Ca	47.72	0.28	23.12	0.66	10.87	82.65
1	MHI10_17	1	Levyne-Ca	47.55	0.32	23.08	0.70	11.08	82.74
1	MHI10_17	2	Levyne-Ca	47.61	0.26	22.84	0.68	11.14	82.53
1	MHI10_17	2	Levyne-Ca	47.73	0.31	22.94	0.63	11.08	82.68
1	MHI10_17	2	Levyne-Ca	47.73	0.28	23.01	0.59	11.00	82.60
1	MHI10_17	2	Levyne-Ca	47.74	0.37	22.95	0.68	10.90	82.63
1	MHI10_17	3	Levyne-Ca	48.83	0.29	23.40	0.62	11.03	84.16
1	MHI10_17	3	Levyne-Ca	48.41	0.24	23.12	0.64	11.14	83.54
1	MHI10_17	3	Levyne-Ca	48.69	0.24	23.04	0.62	11.01	83.60
1	MHI10_17	3	Levyne-Ca	48.79	0.28	22.85	0.72	11.01	83.65

Appendix C: Complete μXRD FWHMχ measurements

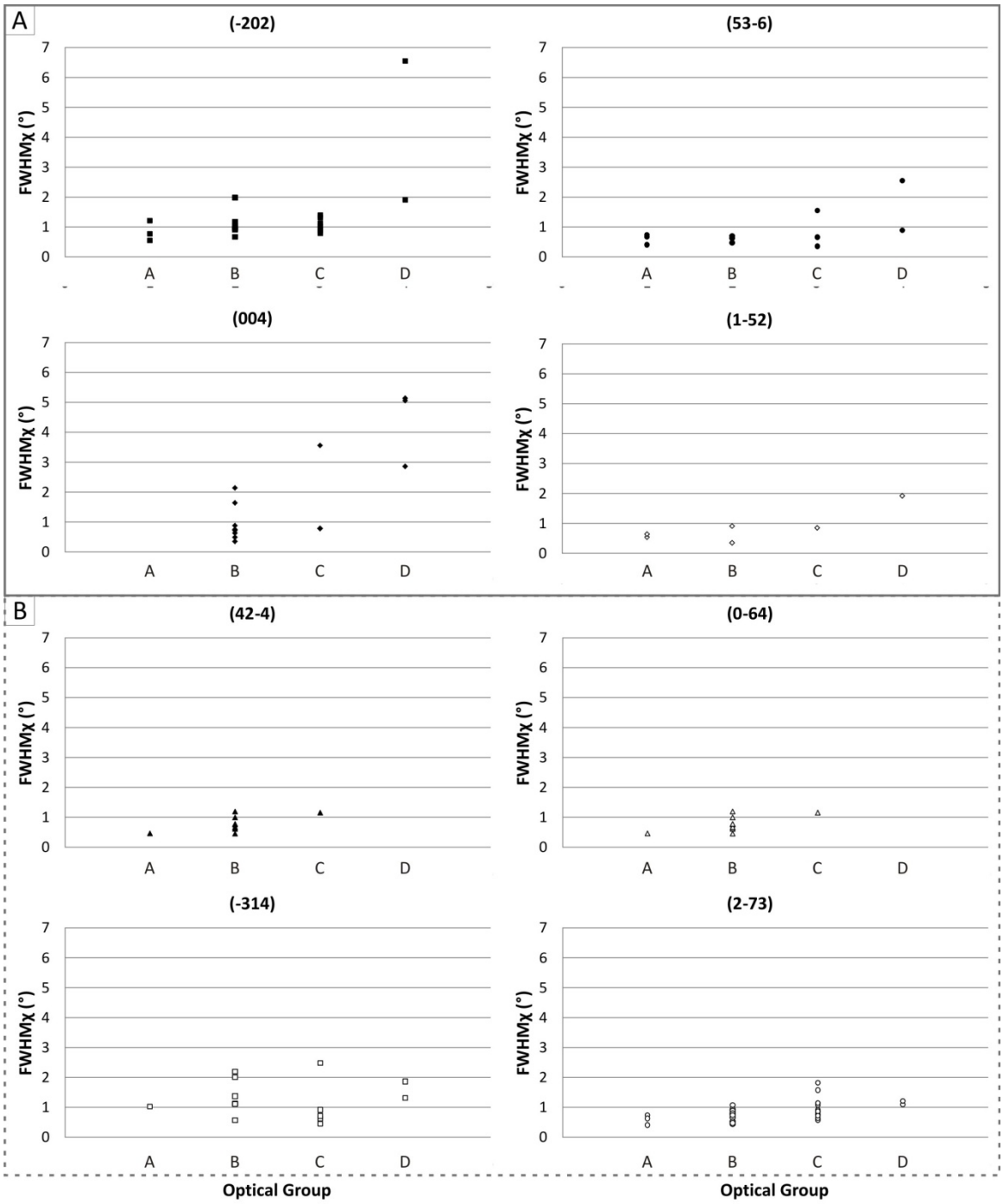

Figure C-1: Mistastin suite FWHMχ vs. optical group for all Miller indices analyzed. Those surrounded by a solid line (A) are used in Chapter 3, those surrounded by a dashed line (B) were excluded due to missing optical groups and poor variation across groups, there is more variation in FWHMχ for Miller indices with lower integer values (A) than those with higher integer values (B).

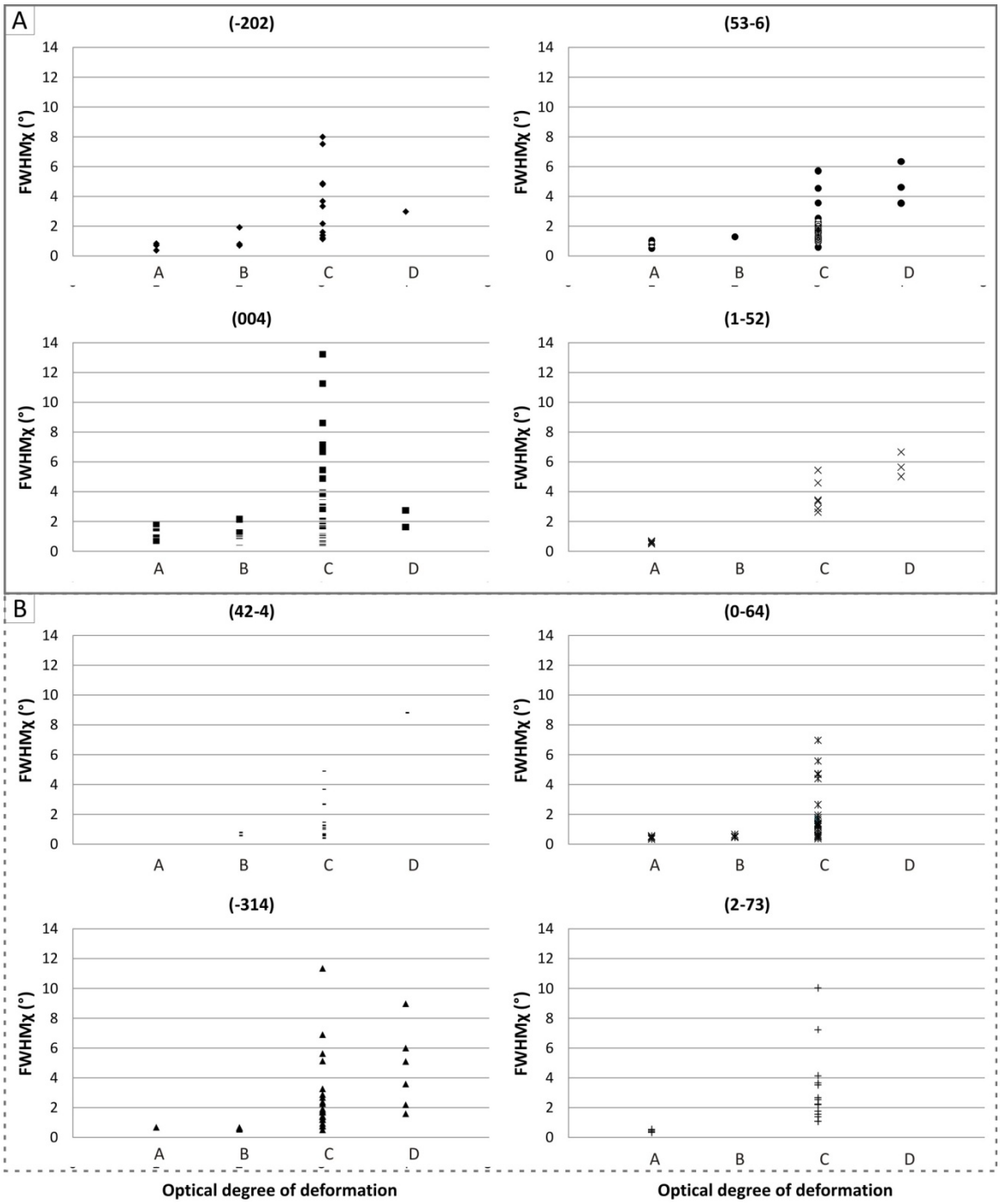

Figure C-2: Apollo suite FWHMχ vs. optical group for all Miller indices analyzed. Those surrounded by a solid line (A) are used in Chapter 3, those surrounded by a dashed line (B) were excluded due to missing optical groups.

Table C-1: Maximum FWHMχ measurements for Mistastin suite

Abbreviations: O.G.=Optical Group

			Miller Index							
Sample Name	**Spot**	**O.G.**	**($\bar{2}$02)**	**(004)**	**(53$\bar{6}$)**	**(1$\bar{5}$2)**	**(42$\bar{4}$)**	**(0$\bar{6}$4)**	**(2$\bar{7}$3)**	**($\bar{3}$14)**
MHI10_17	7	B		0.36						
MHI10_17_542	14	A						0.52		
MHI10_17_542	18	A			0.41					
MHI10_17_542	2	B					0.61			
MHI10_17_542	4	B					0.45			
MHI10_17_542	5	B			0.63					
MHI10_17_542	6	B					1.2	0.86		
MM09_010	1	C		3.57					1.83	2.49
MM09_010	4	D	1.91		2.56	1.93				
MM10_001c	10	A	0.78					0.88		
MM10_001c	11	A				0.55			0.74	
MM10_001c	12	A	1.22							1.03
MM10_001c	13	A	0.56			0.65				
MM10_005c_016	2	D	6.55							
MM10_025	1	B		0.89					0.67	
MM10_025	2	B		1.65					0.82	
MM10_025	4	B							0.9	
MM10_025	5	B		0.64						
MM10_025	8	C							1.08	
MM10_025	9	C							0.77	
MM10_025	10	C							0.61	
MM10_025	11	C							0.92	
MM10_025	7	D		2.53						
MM10_028	7	A					0.46	0.99	0.41	
MM10_028	5	B					0.66		0.53	
MM10_028	6	B	1.02							
MM10_11	4	A			0.67				0.63	
MM10_11	3	B			0.71				0.66	1.38
MM10_11	5	B		2.15					0.95	2.195
MM10_11	6	B		0.73					0.44	1.13
MM10_11	7	C			0.67					
MM10_11	8	C	1.32		0.66					
MM10_11	9	C							0.57	0.62
MM10_11	10	C							1.58	
MM10_11	1	D		5.15					1.1	1.87
MM10_11	2	D		2.87	0.9				1.22	1.32
MM10_13_2	2	B	1.99	0.76				1.49		2.01
MM10_32B	2	B					1	0.53	0.78	
MM10_32B	3	B					0.76		0.89	
MM10_32B	4	B	0.91		0.48			0.4		
MM10_32B	1	C						1.16		

(Table C-1 continued)

			Miller Index							
Sample Name	**Spot**	**O.G.**	**($\bar{2}$02)**	**(004)**	**(53$\bar{6}$)**	**(1$\bar{5}$2)**	**(42$\bar{4}$)**	**(0$\bar{6}$4)**	**(2$\bar{7}$3)**	**($\bar{3}$14)**
MM10_33_39_43	10	A			0.74					
MM10_33_39_43	14	A						0.47		
MM10_33_39_43	18	B	0.67			0.36		0.97		
MM10_33_39_43	1	C	0.80					0.51		
MM10_33_39_43	2	C	1.03					0.51		
MM10_33_39_43	4	C			1.56			2.17		
MM10_33_39_43	5	C			0.36			0.38		
MM10_33_39_43	17	C						1.05		0.45
MM10_36b_1	3	C							0.85	
MM10_36b_1	6	C	0.88	0.80						
MM10_36b_1	7	C		0.79				1.56		
MM10_36b_2	1	C							1.15	
MM10_38_40_42	1	B	0.96	0.50						
MM10_38_40_42	2	C							0.87	
MM10_38_40_42	3	C	0.94							
MM10_38_40_42	7	C	1.13							
MM10_40	1	B	1.18					0.65	0.53	1.12
MM10_40	2	B					0.67		0.80	0.57
MM10_40	7	B				0.92		0.39		
MM10_40	11	B						0.58	0.48	
MM10_40	12	B					0.78		0.48	
MM10_40	13	B						1.29	1.08	
MM10_40	14	B						0.58	0.74	
MM10_40	3	C	1.40						0.64	
MM10_40	4	C						0.70		0.92
MM10_40	5	C								
MM10_40	6	C				0.86	1.16		0.73	
MM10_40	8	C								0.72

Table C-2: Maximum FWHMχ measurements for Apollo suite

Abbreviations: O.G.=Optical Group

			Miller Index							
Sample Name	**Spot**	**O.G.**	**$(\bar{2}02)$**	**(004)**	**$(53\bar{6})$**	**$(1\bar{5}2)$**	**$(42\bar{4})$**	**$(0\bar{6}4)$**	**$(2\bar{7}3)$**	**$(\bar{3}14)$**
10047_16	4				0.79					
12054_126	15	C				5.46				6.91
15362_11	10	C		1.76						
15415_90	5	C		3.70			0.41	0.59		
15415_90	6	C			2.54					
15415_90	7	C		1.21						
15415_90	8	C		2.31	1.19			1.64		
15415_90	9	C						0.80		
15684_4	2	C				3.45				1.93
15684_4	4	D				6.66				1.61
60015_114	11	C		11.27						
60015_114	10	C		6.71						
60015_114	12	C			5.72				10.04	
60015_114	14	C	4.89					1.94		
60025_230	16	C	2.18	1.42						
60025_230	17	C		0.98						
60055_04	1	C	1.40					0.67		
60055_04	2	C	1.14		0.60		0.70			
60055_04	3	C							1.58	
60055_04	4	C						0.47		
60055_04	6	C						0.54		
60215_13	5	C					1.26		3.66	1.71
60215_13	9	B						0.53		0.69
60215_13	6	C			1.97		0.59			0.53
60215_13	8	C			1.75			2.66		1.24
60215_13	7	C							1.76	1.42
60618_4	12	C		1.09		2.87				
60618_4	13	C		1.69						
60618_4	11	C		3.78		2.63				
60619_2	4	B		0.77				0.46		
60619_2	2	B		0.67	1.31			0.66		
60619_2	1	A		1.38	0.51	0.66		0.35		
60619_2	5	A			1.04					
60619_2	6	A				0.51				
60619_2	7	A		0.72						
60619_2	8	A		0.72	0.79			0.44		
60619_2	3	A		1.14				0.55		
60629_2	15	C			3.58					
60629_2	16	C			2.29	3.37				
60629_2	17	C		3.78						
62237_21	1	B		2.16			0.78	0.50		

(Table C-2 continued)

			Miller Index							
Sample Name	**Spot**	**O.G.**	**($\bar{2}$02)**	**(004)**	**(53$\bar{6}$)**	**(1$\bar{5}$2)**	**(42$\bar{4}$)**	**(0$\bar{6}$4)**	**(2$\bar{7}$3)**	**($\bar{3}$14)**
62237_21	3	B								0.66
62237_21	2	C		1.28				0.57		
62237_21	4	C			0.95					
62237_21	5	C		3.45	1.27					
62237_21	6	C		3.22					2.20	2.9
62237_21	7	C		1.27						0.96
62237_21	8	C		3.92						2.4
62237_21	12	C		2.86	1.34			1.41		1.82
62237_21	13	C								1.73
62237_21	14	C		0.66			1.02			1.46
62237_21	15	C		0.89	2.02			0.99		
62237_21	16	C		1.54	1.53			1.42	2.25	1.4
62237_21	17	C		1.34						1.21
67075_41	1	C	1.22	2.32				1.33		
67075_41	5	C		0.62						
67075_41	2	C		0.72				1.34		
67075_41	3	C		0.66	1.12					
67075_41	4	C		0.83	4.56					
67415_113	3	B	0.71	0.63			0.59	0.49		0.57
67415_113	5	B	0.8	0.75						
67415_113	4	B		0.85						
67415_113	6	B		0.87						
67415_113	7	B	1.93	1.26						0.64
67415_113	2	C		0.6						
67415_113	1	A		1.77						
67746_12	1	A				0.63			0.35	
67746_12	3	A							0.57	
67746_12	4	A	0.72						0.49	
67746_12	5	A	0.84			0.70			0.39	
67746_12	2	A				0.58			0.38	
68035_06	1	C							2.68	
68035_06	2	C							2.54	
68035_06	4	C						4.40		
68035_06	5	C						4.69		
68035_06	6	C						1.30		
69955_27	3	C	8.02	4.89	2.12		2.69	4.74		5.14
69955_27	5	C	3.69	*7.17	1.55		1.10			2.7
69955_27	6	C	3.35	3.87				6.97		
69955_27	1	C		8.61					7.24	
69955_27	4	C		13.24						
69955_29	3	C	7.54				3.69			
69955_29	5	C							4.16	
73215_193	6	C	1.61					5.59		0.81

(Table C-2 continued)

			Miller Index							
Sample Name	**Spot**	**O.G.**	**($\bar{2}$02)**	**(004)**	**(53$\bar{6}$)**	**(1$\bar{5}$2)**	**(42$\bar{4}$)**	**(0$\bar{6}$4)**	**(2$\bar{7}$3)**	**($\bar{3}$14)**
73215_193	7	C								3.28
73215_193	7	C								5.64
73215_193	2	C	4.82		1.65	4.60				11.35
73215_193	5	A	0.38					0.48		0.70
76335_55	1	C						1.31		
76335_55	3	C		0.67			1.48			
76335_55	5	C		5.47					1.10	
76335_55	4	C		2.05				1.77		
76335_55	6	C						0.38		
79155_58	6	D	2.99	1.63						
79155_58	5	D								2.21
79155_58	4	D			4.62	5.03				8.98
79155_58	2	D		2.76	6.34	5.65	8.82			5.11
79155_58	1	D			3.55					3.60
79155_58	3	D								6.01

Curriculum Vitae

Name: Annemarie E. Pickersgill

Post-secondary Education and Degrees:
The University of Western Ontario
London, Ontario, Canada
2007-2011 B.Sc. (Honours)

The University of Western Ontario
London, Ontario, Canada
2012-2014 M.Sc.

Honours and Awards:
Natural Science and Engineering Research Council (NSERC)
2012-2014 (CREATE Technologies and Techniques for Earth and Space Exploration, M.Sc. Fellowship)
2013-2014 (Alexander Graham Bell Canada Graduate Scholarship – CGS-M)
2014-2017 (Postgraduate Scholarship – PGS-D)

Ontario Graduate Scholarship (OGS)
2012-2013, 2013-2014 (declined)

Lunar and Planetary Institute Career Development Award
2013

University of Glasgow
College of Science & Engineering Scholarship
2014-2017

Related Work Experience
Graduate Research/Teaching Assistant
The University of Western Ontario
2012-2014

Summer Research Assistant
The University of Western Ontario
2008-2011

Selected Publications:

Pickersgill A. E., Flemming R. L., and Osinski G. R. (2014) Streak Lengthening in Chi (°χ) from Micro-X-Ray Diffraction Patterns of Shocked Lunar and Terrestrial Plagioclase (abstract #2595). *45th Lunar and Planetary Science Conference*. Houston, Texas.

Pickersgill A. E., Flemming R. L., Osinski G. R., and Singleton A. C. (2013) Micro-X-Ray Diffraction Patterns of Shocked Plagioclase from the Mistastin Lake Impact Structure, Canada (abstract #5362). *76th Annual Meeting of the Meteoritical Society*. Edmonton, Alberta.

Pickersgill A. E., Osinski G. R., and Flemming R. L. (2013) Shock Metamorphism in Plagioclase from the Mistastin Lake Impact Structure, Canada (abstract #2471). *44th Lunar and Planetary Science Conference*. Houston, Texas.

Pickersgill A. E., Flemming R. L., and Osinski G. R. (2013) Shock Metamorphism in Plagioclase from the Mistastin Lake Impact Structure, Canada (abstract #303). *Geological Association of Canada – Mineralogical Association of Canada Annual Meeting*. Winnipeg, Manitoba.

Pickersgill A. E. and Osinski G. R. (2013) Planar Deformation Features in Quartz at the Newly Discovered Prince Albert Impact Structure, Northwest Territories, Canada (abstract #2602). *44th Lunar and Planetary Science Conference.* Houston, Texas.

Osinski G. R., Tornabene L. L., Banerjee N. R., Cockell C. S., Flemming R., Izawa M. R. M., McCutcheon J., Parnell J., Preston L., Pickersgill A. E., Pontefract A., Sapers H. M., Southam G. (2013) Impact-generated hydrothermal systems on Earth and Mars. *Icarus.* 224(2), 347-363.

Pickersgill A. E., Osinski G. R., and Mader M. M. (2012) A Formational Model for an Impact Melt-Bearing Breccia Dyke at the Mistastin Lake Impact Structure, Labrador, Canada (abstract #2473). *43rd Lunar and Planetary Science Conference*. Houston, Texas.

Pickersgill A. E., Osinski G. R., and Mader M. M. (2011) Characterization of shock in the impact-melt-bearing breccias of the Mistastin Lake impact structure, Labrador (abstract #487). *Geological Association of Canada – Mineralogical Association of Canada Annual Meeting*. Ottawa, Canada.